Data-Driven Interactive Simulations for Clinical and Robotic Applications

Jérémie Dequidt

Jérémie Dequidt. Data-Driven Interactive Simulations for Clinical and Robotic Applications. Modeling and Simulation. Université de Lille, 2023. tel-04144574

HAL Id: tel-04144574
https://inria.hal.science/tel-04144574
Submitted on 28 Jun 2023

Université de Lille

École Graduée Mathématiques, Sciences du numérique et de leurs interactions

Habilitation à Diriger des Recherches en Informatique

Simulation guidée par l’image pour applications cliniques et robotiques

Data-Driven Interactive Simulations for Clinical and Robotic Applications

Jérémie Dequidt

Composition du Jury

Rapporteur	Fernando Bello (PR)	Imperial College London
Rapporteur	Robert D. Howe (PR)	Harvard Paulson S.E.A.S
Rapporteuse	Maud Marchal (PR)	Université de Rennes
Examinatrice	Marie-Odile Berger (DR Inria)	Centre Inria Nancy - Grand Est
Examinateur	Pierre Renaud (PR)	INSA Strasbourg
Examinateur	Laurent Thines (PUPH)	CHU Besancon
Examinateur	Stéphane Cotin (DR Inria)	Centre Inria Nancy - Grand Est
President	Rochdi Merzouki (PR)	Université de Lille
Garant	Christian Duriez (DR Inria)	Inria Centre at the University of Lille

Vendredi, 10 février 2023

Jérémie Dequidt

Data-Driven Interactive Simulations for Clinical and Robotic Applications

Habilitation à Diriger des Recherches, Friday, February 10th 2023

Université de Lille

École Graduée Mathématiques, Sciences du numérique et de leurs interactions

Abstract

The research works briefly reviewed in this dissertation deal with questions related to the use of data in interactive simulations for applications in medicine and soft robotics. Geometrical modeling, (bio-)mechanical modeling as well as optimization techniques to reduce the computational footprint are presented. Using patient-specific or environment data with optimization techniques and simulation enables more realistic and predictive models and opens the way for new applications. Several examples are presented in the manuscript where our simulations were fed with data from medical images, videos streams or pre-operative data in order to provide more accurate medical simulations to provide better diagnoses or in the context of soft-robotics where visual servoing provides a more robust and stable control of soft-robots.

Résumé

Les travaux de recherche examinés dans ce manuscrit traitent des questions liées à l'utilisation des données dans les simulations interactives pour des applications en médecine et en robotique déformable. La modélisation géométrique, la modélisation (bio-)mécanique ainsi que les techniques d'optimisation pour réduire l'empreinte de calcul sont présentées. L'utilisation de données spécifiques au patient ou à l'environnement avec des techniques d'optimisation et de simulation permet des modèles plus réalistes et prédictifs et ouvre la voie à de nouvelles applications. Plusieurs exemples sont présentés dans le manuscrit où nos simulations ont été alimentées avec des données provenant d'images médicales, de flux vidéo ou de données préopératoires afin de fournir des simulations médicales plus précises pour fournir de meilleurs diagnostics ou dans le contexte de la robotique déformable où l'asservissement visuel fournit un contrôle plus robuste et stable des robots souples.

Foreword

> *Det spiller ingen rolle hvor sakte du går så lenge du ikke stopper.*
>
> — **Norwegian saying**

First of all, I would like to thank my three reviewers: Maud, Fernando and Robert for accepted to review my work. I feel very honoured to have such prestigious scientists assessing my work and providing valuable feedbacks and inspiring comments about my work. I also would like to thank my defence committee (Laurent, Pierre, Marie-Odile, Stephane and Rochdi) for their nice words during the defence and for their interesting and relevant questions.

I also to thank Christian for his help during these past years. It has been a pleasure working with you since the Shaman/Shacra era and it has been a very passionate journey to help building DEFROST with you. I am very proud to be part of the team and to contribute to the many successes we had in medical simulations and soft robotics. Thank you also for being comprehensive about that the fact that an associate professor position implies many teaching and administrative duties.

Special thanks to Stephane: after my PhD, the perspective of having a career in academic was an unattainable destination and something I didn't consider for myself. You gave me the opportunity to join your team in Boston, you gave me full trust for developing my ideas and with you I unlocked my potential for doing research. We had many projects, many great achievements and many funny moments throughout the years. Even if things have changed since Mimesis / Defrost split, I am still very grateful for what you have done.

Many thanks for the numerous colleagues I have worked with since my PhD. I am taking advantage of the opportunity to thank the Alcove colleagues especially, Jowan and Jeremy which have now successful careers outside academics, the Shacra colleagues especially Nazim and Hugo (our Siggraph / post-Siggraph trip is still one of my best memories), Alex... and finally the Defrost ones Bruno, Damien, Alex K., Olivier, Eulalie, Thor, Quentin, Younes, Gang and the PhD students I have co-supervised. Thanks also for the people outside the Shacra/Defrost circle: Lambert, Marie-B, Axelle, Geraldine and of course thanks to our swiss-army knife / problem solver wonder wom-Anne. Even if he has moved for sunnier places, I would like to thank David Simplot for being a role-model in many ways. Many thanks to the colleagues that are always ready for collaborative works: Erwan and P-F, Kenny and Miguel.

I would also like to thank colleagues from Polytech Lille because it has been an important place for my professional career and the office where I have spent most of my time lately (sorry Christian :/). Thanks to the teaching colleagues Alex, Florian, Nico, Sara, Bernard, Olivier, Othman, Rochdi, Laure... and François for sharing tips and tricks about managing an engineering department but also to the administrative colleagues Mumu, Melanie and Barbara for their efficient help and their responsiveness. It is nice working with all of you guys and having fun parties together. Special thanks to Manue (my partner in crime) for the fun and laugh you bring to this place and our fruitful collaboration. A final thank to Guy who learned me a lot, Nico for his trust (I hope to help you to do great things) and Cyril for his support.

Thank you also to my friends for their cheerful support and stress relief: Matthieu (my sidekick in sport), the Mexican mafia (Walter, Marcia, Vincent and Julien), the Houlette team (Oliv' and Caro, Steph and Marie, Jo and Eugen', Vincent and Sabine) and the polytech friends (Nour, Timmy, Pierre, Jean, Debo, Coline, Boris...) for the rare but precious moments. Thanks also to Clemence and Ju', Dom' and Louis, Pti' Pierre. Thanks also to the TNBM circle (Gylve, Ørjan, Vegard and Kristoffer), the DI6 circle (Douglas, Tony, Michael and Rose) and Lana for the inspiration.

And last but not least, I would like to thank my parents Gilles and Edith, my brother Geoffrey, my grand-mother Aniela and my family on the Putkownik and Dequidt side for their constant support and love. Thanks also to my step-family for their interest, support and accepting me as a full member of their clan: Bertrand, Françoise, Arnaud, Vincent and all the LSW. And finally a huge, full of love thank you to Marion for her love, her support and her inspiration that helps me reach this goal.

Contents

Introduction

> *If the doors of perception were cleansed*
> *everything would appear to man as it is, infinite.*
> *For man has closed himself up till he sees all*
> *things thro' narrow chinks of his cavern.*
>
> — **William Blake**

Digital technologies have greatly jolted modern medicine. For instance, the combination of electromagnetic radiation and digital geometry processing has originated the *X-ray computed tomography* (or *X-ray CT*) that allows to create a three-dimensional image of the targeted anatomical area. Another example is the use of computer vision algorithms to fuse (*register*) data from different imaging modalities such as *MRI* (*Magnetic Resonance Imaging*) that provides high-quality but slow-to-create images and *Ultrasonography* (*US*) that delivers real-time but noisy images. This fusion of information offers the opportunity to have high-quality and real-time visual feedbacks of anatomical structures. These two examples are part of a larger set of technologies such as *Radiography*, *Endoscopy*, *Positron Emission Tomography*... that are usually referred by the generic term of **Medical Imaging**. There are many direct benefits of Medical Imaging: it is non-invasive (no or small incision is required), accurate, efficient, interactive and provides rich information. Location of diseased areas is more accurately identified and tracked, evolution of pathologies is more easily monitored allowing physicians to establish precise diagnoses. Initially aimed at pre-operative steps of surgery, the availability of this technology has redefined some surgical procedures where treatments can be delivered deep within the body without surgery: for instance, bone biopsies can be performed in a minimally invasive manner under image guidance, which avoid blood loss, complications, scars and long recuperation [Jel+02]. They are now fully integrated in clinical routines and have led to safer, less morbid and more cost-effective medical interventions. The main drawback of such approach is that the complexity of the procedures has significantly increased: anatomical structures manipulation is indirect through telescopic devices or flexible ones and the clinicians observe the on-going procedure through monitors. Several studies (for instance [Sil+09]) reports several disadvantages related to the use of video-assisted surgery such as the loss of visual contact with instruments that may cause disruptions or is more prone to complications, the usually fixed camera induces spatially transformed and suboptimal pictures and the loss of three-dimensional depth cues creates psychomotor problems of hand-eye coordination. Having inaccurate, suboptimal and non-consistent feedbacks (be they tactile, haptic or visual) adds a level of complexity to already stressful and complex procedures. To overcome the difficulties induced by minimally invasive surgery, two complementary approaches are considered. The first one is to make the surgeons more familiar with these procedures by providing a dedicated training that will first focus on the improvement of psychomotor skills. The second one is to provide computer or robotic assistance that will augment the surgeon capabilities to conduct the surgical procedures such as the daVinci© robot that allows to filter out hand tremors and to scale movements and forces.

Virtual Reality (*VR*) applications have been adequate training tools for improving hand-eye coordination in case of minimally invasive surgery because they offer a reproducible, controlled, supervised and ethical environment. The logical progression of these applications had been to train high-level tasks (such as suture) or even perform a complete surgical procedure by using simulation to mimic the behavior of the human anatomy. However, despite several governmental incentives [AC04] few clinical curricula require training on simulators. De Visser *et. al.* [De +11] report that while the benefits of VR simulators are indisputable to train novice-to-intermediate skills, they are yet not suitable for the training and maintenance of advanced skills. Insufficient level of physical realism, incomplete performance assessment and modest case complexity are suggested by De Visser *et. al.* [De +11] to be the main limitations to use simulators for surgical curricula. First, the insufficient level of physical realism relates to the fact that the modeling and simulation of human anatomy remains challenging. Several physical behaviors should be considered such as biomechanics, electro-physiology... and they are difficult to model. For instance, surveys in the field [Hum03] detail the complexities of the microstructure and the biomechanical behaviour of biological cells and tissues. These complexities can be captured, reproduced or sometimes predicted thanks to an important computation time. In the context of interactive *VR* applications, the trade-off between simulation accuracy versus simulation speed always leans toward the later producing fast-response applications but unable to faithfully reproduce the richness of the human anatomy. Second, limited case complexity can be partially related to the fact that the building of a virtual 3D model of an anatomical structure relies on many patient-specific parameters to be acquired. Some can be obtained through a time-consuming process which involves medical image segmentation (*i.e.* to delimit the different anatomical structures in an image), 3D reconstruction (*i.e.* to build a

3D model from segmented images) and 3D model tuning (*i.e.* trade-off between model complexity and desired accuracy) to be suitable for interactive applications. Some other parameters, for instance mechanical or physiological parameters, can be hardly acquired without invasive (and therefore ethically questionable) probes or sensors. As a consequence, these measurements are often conducted on animals or cadavers in order to have a rough estimation of the parameters. And some manual or semi-automatic post-processing can be needed to adjust these parameters as they are essential to obtain accurate simulations. Given the long time scale and the human interventions needed to acquire relevant data, VR simulators often propose a small set of virtual patients and scenarios. The length and the complexity of the acquisition pipeline do not only hinder the use of training simulator in the context of modern medicine but it also slows down the development of other applications. For instance, patient-specific interactive simulations could be used by surgeons to rehearse the procedure on a specific patient, to try different strategies, to face possible complications. . . in order to determine the safest procedure to be performed on the *real* patient.

Per-operative guidance could also be considered as a way to help the surgeon during an actual procedure by giving additional information such as the presence of weakened structures, the location of targeted area which are hardly visible. . . Augmenting the perception and the capabilities of the surgeons is the second approach used to reduce the complexity of minimally invasive procedures. In that case, patient-specific data plays a key role (and there are several other research problems to consider) for taking virtual reality applications to their next step: to provide, in real time, feedbacks about the geometry, mechanical or physiological status of the biological structures being manipulated. Moreover patient-specific data could also opens the way to new medical applications. For instance soft robotics, the scientific field that targets the design and the building robots made of soft materials, such as silicone, is expected to produce important outcomes in medicine. Surgical robots are made of metal alloys that interact with delicate biological tissues and are much stiffer than any anatomical structures (except for bones whose stiffness is of the same magnitude as metal alloys[1]). This stiffness gap results in robots damaging living tissues due to excessive contact pressures or stress that may lead to medical complications to the patient. Soft materials tighten this stiffness gap reducing potential damages when in contact with anatomical structures thanks to their ability to deform and to conform to the environment they are in contact with. This ability to deform raises however several scientific challenges; some are generic like how to accurately model

---

[1] Stiffness of common materials can be found here: `http://www.engineeringtoolbox.com/young-modulus-d_417.html`

and control a soft robot, some are specific to surgery where the control law of the robot should take into account the possible contacts with the living tissues and thus requires an accurate computational model of the human body.

These two complementary goals to help surgeons to perform surgery induce several research problems for which we have proposed some original contributions. This manuscript will be focused on medical applications since they were my main application field since my PhD. But the contributions detailed here could be relevantly used in other domains and several examples will be provided throughout this document. Our aim is to tackle the problem of patient-specific data for interactive simulations and the rationale of our approach is to mostly rely on images (be it medical images or video streams) to estimate geometric and physical parameters. We focus on images as the main source of patient-specific data for two reasons. First, images are non-invasive and routinely used in medical procedures: we have already mentioned that medical diagnosis is a big consumer of medical images (*CT Scan*, *IRM*, *UltraSound*. . .), minimally invasive surgery (surgery through small incisions) relies on tiny cameras or endoscope and finally interventional radiology procedures are also supported by X-ray imaging. Second, images can be used as ground-truth to validate our simulation and moreover can be also used in an optimization framework to (dynamically) refine the parameters of the simulation. More specifically, the work we have conducted over the last few years relates to the acquisition and optimization (from a simulation standpoint) of patient-specific data, to the use of images to validate experimentally simulation and to the use of images to infer or estimate relevant parameters for the simulation. We want to emphasize that the scope of our works lies at the intersection of Computer Vision, Geometric and Physics-based Modeling and finally Interactive Simulation and that our main motivation is to strive to *enrich* generic medical simulations to make them patient-specific. Bridging the gap between simulation and images also implies several technical constraints we have to deal with, such as the quality and availability of images or the limited computational footprint of the physics-based model in order to achieve interactive simulations. These constraints lead to not having a single solution relevant to every kind of simulation or imaging techniques. However while the solutions are different we want to illustrate that our methodology (*i.e.* the use of a fast physics-based model as a backbone) allows to define relevant and efficient strategies for different kind of medical procedures. Those works have thus been possible through tight collaborations with surgeons and radiologists and have been declined in various medical fields such as Interventional Radiology, Laparoscopic Liver Surgery, Pelvic System Diagnosis and Radiotherapy. Finally modern medicine could benefit from the use of soft robots. Soft Robotics is a recent cross-disciplinary field that binds

Applied Mathematics, Automatic Control, Mechanical Engineering, Robotics, Mechatronics. . . In this field, the control of soft / deformable structures is a challenge and we will demonstrate that the work that has been conducted on medical simulation could be adapted to the control of soft robots.

The work presented in this manuscript covers the main results obtained following my PhD in 2005. I first spend one year in the SimGroup (CIMIT/Harvard Medical School / Mass General Hospital, Cambridge, USA) in 2006–07 where I have been working in geometrical modeling and contact modeling of vascular networks. This work has been continued in 2007–08 when I joined a collaboration between Inria teams Alcove and Magrit about the development of interventional radiology simulation. Since 2008, I am Assistant Professor at University of Lille and I have been involved in the research team Shaman / S.h.a.m.a.n / Shacra where the main focus was about surgical simulations. There, I have worked on modeling, parameter-estimation of digital models from medical images, simulation and augmented reality and the natural trend of my research work has been to integrate more and more data (medical images, video streams, sensors information. . .) in order to characterize digital models and to enrich surgical simulations. Since 2015, I am a member of Defrost research team whose main objective is to provide software tools to design, simulate and control soft robots. In Defrost, I will extend the works on parameter estimation to increase the robustness of the digital model of the soft-robot and to enable a closed-loop control of the robot. The work presented here is a collective effort conducted in about 10 years with colleagues in my successive research teams and some fruitful collaborations. I had also the opportunity to advise some PhD students: Ahmed Yureidini [Yur14], Nazim Haouchine [Hao15], Zhifan Jiang [Jia17], Zhongkai Zhang [Zha19], Pierre Schegg [Sch22] and Flavie Przybylski who will defend her thesis in 2024.

This manuscript is structured as follows. The first chapter Interactive Physics-based Simulation deals with interactive simulations: how to optimize the computational footprint and the possible use of digital simulations for medical applications. The work related to the extraction of dedicated, optimized geometric modeling from medical images is described in the second chapter Geometric Modeling for Interactive Simulation. The third chapter Medical and Robotic Applications details advances clinical and robotics applications that have been built using the works developed in the first two chapters.

Curriculum Vitae

Jeremie Dequidt

Nationality	French	**Date of Birth**	December, 4th 1979
Website	www.dequidt.me	**Place of Birth**	Dechy (59), France

- Associate Professor (Maître de Conférences) at University of Lille, CNU Section 27 (Computer Science)
- Member the DEFROST team (joint team between CRIStAL and Inria)
- Head of the Embedded Systems Department at Polytech Lille

Background

2008-now	**Associate Professor, University of Lille** *Research*: Geometrical and Biomechanical Modeling, Animation and Digital Simulation, Virtual and Augmented Reality, Soft Robotics *Teaching*: Programming, Computer Theory, Computer Graphics, Numerical Analysis, Digital Physics-based Simulation
2007-2008	**Post Doctorate, Inria** *Research*: Mechanical modeling of surgical tools for the simulation of interactive radiology interventions
2006-2007	**Research Fellow, CIMIT / Harvard Medical School, Cambridge (MA)** *Research*: Mechanical modeling of surgical tools for the simulation of interactive radiology interventions
2005-2006	**Adjunct Professor, Polytech Lille** *Research*: Computer Graphics and Simulation, Distributed Computation *Teaching*: Operating Systems, Databases, Programing
2002-2005	**PhD Student, University of Lille** *Research*: Computer Graphics and Simulation, Distributed Computation *Teaching*: Operating Systems, Networks, Programing

Doctoral Co-Supervision

Defended Thesis

- Ahmed Yureidini: Robust Blood Vessel Modeling for Interactive Simulations, defended 13/05/2014
- Nazim Haouchine: Image-guided simulation for augmented reality during hepatic surgery, defended 26/01/2015
- Zhifan Jiang: Évaluation des mobilités et modélisation géométrique du système pelvien féminin par analyse d'images médicales, defended 27/01/2017
- Zhongkai Zhang: Vision-based Calibration, Position Control and Force Sensing for Soft Robots, defended 10/01/2020
- Pierre Schegg: Autonomous Catheter and Guidewire Navigation for Robotic Percutaneous Coronary Interventions, defended 25/05/22

On-going Thesis

- Flavie Przybylski (start 1/10/2021): Simulation, design and fabrication of wine-robots

Undefended Thesis

- Francois Dervaux (start 1/10/2012), has leaved 18 months after the beginning of the thesis for a job in the industry

Post-Doctorate and Master Supervision

Post-Doctorate

- 2017-18, Thomas Morzadec, geometric modeling of soft-robots

Master Students

- 2018, Meichun Lin (Bio Medical Engineering Master2), training simulator for brachytherapy procedures
- 2017, Félix Vanneste (ISEN Engineer), bridging between SOFA and ROS
- 2016, Piotr Sordyl (Erasmus Master), sensibility analysis of catheter simulations
- 2014, Matthias De Bie (Polytech·Lille Engineer), bridging rendering and simulation softwares
- 2013, Pierre-Jean Petitprez (Polytech·Lille Engineer), real-time X-ray rendering
- 2013, Mélanie Lelaure (Polytech·Lille Engineer), user interface for interventional radiology simulations
- 2012, François Dervaux (Master2 IVI), asynchronous simulation in SOFA
- 2011, Nazim Haouchine (Master2 IVI), physics-based simulation and augmented reality

Temporary Engineers

- 2018, Meichun Lin, training simulator for brachytherapy procedures
- 2016, Christo Gnonnou, sensibility analysis of catheter simulations
- 2015, Mario Sanz Lopez, device for tracking neuro-surgical devices

Highlights

- Recipient of the Young Researcher Funding Programme (French Research Agency) in 2012, 175 keuros
- Recipient of the Dirk Bartz Prize for Visual Computing in Medicine in 2015
- Recipient of the Doctoral Supervision and Research Bonus (PEDR) for 2015–2018 and 2019–2022
- Runner-up Best Paper Award in ISMAR 2013
- TVCG Top Ranked AR/VR paper (presented at SIGGRAPH 2015)
- Best Paper Award in SIMPAR 2016
- Best Paper Award in Advanced Robotics 2018

Collaborations and Responsibilities

Collaborations

- University of Copenhagen, Kenny Erleben and Sune Darkner (on-going project about Digital Twins)
- Universidad Rey Juan Carlos, Miguel Otaduy (on-going project about Digital Twins)
- Vrije Universiteit Brussel, Bram Vanderborght (on-going project about Digital Twins)
- Magrit Team (Inria Nancy), Erwan Kerrien and Marie-Odile Berger (2 PhD co-supervising)
- Mimesis Team (Inria Nancy), Stéphane Cotin (2 PhD co-supervising), Igor Peterlik (publications on asynchronous simulation)
- LML, Mathias Brieu, Pauline Leconte, Jean-Francois Witz (1 PhD co-supervising)
- COL, Nick Reynaert (publication on deformable registration using FEM)
- King's College London, Hongbin Lu (publication on visual servoing for robotized catheter)
- CI2S (CRIStAL), Rochdi Merzouki (project on robotized brachytherapy)
- CHR Huriez, Jean-Francois Rouland (various publications on cataract surgery simulation)

Implication in the scientific communities

International Program Committee

- International Symposium on Visual Computing 2018, 2019, 2020
- Workshop on Virtual Reality Interaction and Physical Simulation (VRIPHYS) 2013, 2014, 2015 (+ Co-Organizer), 2018
- International Symposium on Biomedical Simulation 2010 and 2014 (+ General Chair)

Projects

- Member of the CNRS project Visadapt (PEPS) 2021-2023
- Member of the European project CoBra (Interreg 2 Seas) 2018 - 2022
- Member of the ADT (Inria Software Development Initiative) SIMILAR, 2018 - 2020
- Member of the European project COMOROS (FERDER grant), 2017 - 2020
- Member of the ANR project SORCERY, 2017- 2020
- Co of the ADT (Inria Software Development Initiative) SOROS, 2016 - 2018
- Prime Investigator of the ANR project IDeaS (Image-Driven Simulation), 2012 – 2016, 175 keuros
- Member of the ADT (Inria Software Development Initiative) SORBET, 2014 - 2016
- Member of the ADT (Inria Software Development Initiative) SIMPLE, 2007 - 2009

Technology Transfers

- 2018: Technology transfer of an interventional radiology simulator to Naviworks
- 2015: Technology transfer of a neurosurgical simulator to InSimo
- 2013: Technology transfer of a cataract surgery (MSICS) simulator to InSimo
- 2011: Industrial contract with HelpMeSee foundation (NGO)

Expertise

- Vice-President of the hiring committee for Assistant Professor positions (Polytech Lille) 2021, 2022
- Member of the evaluation committee for the french research agency (CE33: Interaction Robotique) 2021-2023
- Reviewer for french research agency (2017 generic call)
- Member of external hiring committees for Assistant Professor positions Calais (2010, 2011), Poitiers (2011)
- Elected Member of the internal hiring committee for Assistant Professor positions (since 2011)
- Reviewer for Soft Robotics, MICCAI, MedIA, Computer Graphics and Applications, IEEE Transaction on Haptics, IEEE/RSJ IROS, IEEE World Haptics, IEEE Transactions on Medical Imaging, Computer Graphics

Teachings

- Head of the Computer and Electrical Engineering (IMA) Department at Polytech·Lille (since 2017-2022)
- In charge of the coordination of the Cross-Disciplinary modules at Polytech·Lille since 2015 (200 students)
- Coordinator of Ima SC (Communicating Systems) track at Polytech·Lille (2011-2017)
- Coordinator of Ima5i track (from 2008 to 2011... now replaced by IMA SC track)
- In charge of 3 modules in computer science at Polytech Lille
- Active participant to the teaching reforms at Polytech Lille
- Member of the Administration board at Polytech Lille
- Teaching charge of 300h/year

Personal Publications

[Anx+09] René Anxionnat, Federico Rocca, Serge Bracard, Jeremie Dequidt, Erwan Kerien, Christian Duriez, Marie-Odile Berger, and Stephane Cotin. “Evaluation of a computer-based simulation for the endovascular treatment of intracranial aneurysms”. In: *10th congress of the World Federation of Interventional and Therapeutic Neuroradiology*. 2009.

[Ben+13] Jan Bender, Jeremie Dequidt, Christian Duriez, and Gabriel Zachmann, eds. *VRIPHYS 13: 10th Workshop on Virtual Reality Interactions and Physical Simulations, Lille, France, 2013. Proceedings*. Eurographics Association, 2013.

[Bil+11] Alexandre Bilger, Jeremie Dequidt, Christian Duriez, and Stephane Cotin. “Biomechanical simulation of electrode migration for deep brain stimulation”. In: *Medical Image Computing and Computer-Assisted Intervention*. 2011, pp. 339–346.

[Bos+14] Julien Bosman, Nazim Haouchine, Jeremie Dequidt, Igor Peterlik, Stephane Cotin, and Christian Duriez. “The Role of Ligaments: Patient-Specific or Scenario-Specific?” In: *6th International Symposium on Biomedical Simulation (ISBMS)*. 2014, pp. 228–232.

[Bou+10] Nadia Boubchir, Stephane Cotin, Olivier Comas, Frederick Roy, Christian Duriez, Jeremie Dequidt, Jeremie Allard, and Jean-Francois Rouland. “Computer-Based Simulation of Cataract Surgery: Toward a New Teaching Paradigm”. In: *Annual Meeting of the American Academy of Ophthalmology*. 2010.

[Bou+09] Nadia Boubchir, Stephane Cotin, Christian Duriez, Jeremie Dequidt, Jeremie Allard, and Jean-Francois Rouland. “Computer-Based Simulation of IOL Injection: Toward a Full Featured Cataract Surgery Training System”. In: *Annual Meeting of the American Academy of Ophthalmology*. 2009 (cit. on p. 43).

[Coe+17] Eulalie Coevoet, Thor Morales-Bieze, Frederick Largilliere, et al. “Software toolkit for modeling, simulation, and control of soft robots”. In: *Advanced Robotics* 31.22 (2017). Best Paper Award, pp. 1208–1224.

[Coe+14] Eulalie Coevoet, Nick Reynaert, Eric Lartigau, Luis Schiappacasse, Jeremie Dequidt, and Christian Duriez. “Introducing interactive inverse FEM simulation and its application for adaptive radiotherapy”. In: *Medical Image Computing and Computer Assisted Intervention*. 2014, pp. 81–88.

[Coe+15] Eulalie Coevoet, Nick Reynaert, Eric Lartigau, Luis Schiappacasse, Jeremie Dequidt, and Christian Duriez. “Registration by interactive inverse simulation: application for adaptive radiotherapy”. In: *International Journal of Computer Assisted Radiology and Surgery* 10.8 (2015), pp. 1193–1200.

[Cot+05] Stephane Cotin, Paul Neumann, Xunlei Wu, Sylvere Fonteneau, Pierre-Jean Bensoussan, Damien Marchal, Jeremie Dequidt, Laurent Grisoni, and Sylvain Karpf. “Collaborative Development of an Open Framework for Medical Simulation”. In: *Insight Journal*. 2005.

[Deq02] Jeremie Dequidt. “Détection de collisions entre objets physiques autonomes”. MA thesis. University of Lille 1, 2002.

[Deq17] Jeremie Dequidt. “Modeling interactions with soft objects”. In: *Workshop on Soft Morphological Design for Haptic Sensation, Interaction and Display*. 2017.

[Deq05] Jeremie Dequidt. “Objets autonomes en simulation physique temps-réel”. PhD thesis. University of Lille 1, 2005.

[Deq+15] Jeremie Dequidt, Eulalie Coevoet, Laurent Thines, and Christian Duriez. “Vascular neurosurgery simulation with bimanual haptic feedback”. In: *12th Workshop on Virtual Reality Interaction and Physical Simulation (VRIPHYS)*. Nov. 2015.

[Deq+13] Jeremie Dequidt, Hadrien Courtecuisse, Olivier Comas, Jeremie Allard, Christian Duriez, Stephane Cotin, Elodie Dumortier, Olivier Wavreille, and Jean-Francois Rouland. “Computer-based training system for cataract surgery”. In: *Simulation: Transactions of the Society for Modeling and Simulation International* 16 (2013), pp. 1–15.

[Deq+09] Jeremie Dequidt, Christian Duriez, Stephane Cotin, and Erwan Kerrien. “Towards interactive planning of coil embolization in brain aneurysms”. In: *Medical Image Computing and Computer-Assisted Intervention*. 2009, pp. 377–385.

[DGC04] Jeremie Dequidt, Laurent Grisoni, and Christophe Chaillou. *Asynchronous Interactive Physical Simulation*. Tech. rep. 5338. ALCOVE (INRIA / LIFL), 2004.

[DGC05a] Jeremie Dequidt, Laurent Grisoni, and Christophe Chaillou. “Collaborative interactive physical simulation”. In: *GRAPHITE ’05: Proceedings of the 3rd international conference on Computer graphics and interactive techniques in Australasia and South East Asia*. 2005, pp. 147–150 (cit. on p. 37).

[DGC05b] Jeremie Dequidt, Laurent Grisoni, and Christophe Chaillou. “Time-Critical Animation of Deformable Solids”. In: *Computer Animation and Social Agents*. 2005.

[DGM04] Jeremie Dequidt, Laurent Grisoni, and Philippe Meseure. “Détection de collisions entre objets rigides convexes autonomes”. In: *Revue de CFAO et d’informatique graphique* 18.2 (2004), pp. 183–195.

[DLC07] Jeremie Dequidt, Julien Lenoir, and Stephane Cotin. “Interactive contacts resolution using smooth surface representation”. In: *Medical Image Computing and Computer-Assisted Intervention*. 2007, pp. 850–857.

[DMG05] Jeremie Dequidt, Damien Marchal, and Laurent Grisoni. “Time-Critical Animation of Deformable Solids”. In: *Computer Animation and Virtual Worlds* 16 (2005), pp. 177–187.

[Deq+08] Jeremie Dequidt, Maud Marchal, Christian Duriez, Erwan Kerien, and Stephane Cotin. “Interactive simulation of embolization coils: Modeling and experimental validation”. In: *Medical Image Computing and Computer-Assisted Intervention*. 2008, pp. 695–702.

[Der+13] Francois Dervaux, Igor Peterlik, Jeremie Dequidt, Jeremie Cotin, and Duriez Christian. “Haptic Rendering of Interacting Dynamic Deformable Objects Simulated in Real-Time at Different Frequencies”. In: *IEEE/RSJ International Conference on Intelligent Robots and Systems*. 2013, pp. 2010–2016 (cit. on p. 37).

[Dum+10] Elodie Dumortier, Stephane Cotin, Jeremie Dequidt, Christian Duriez, Jeremie Allard, and Jean-Francois Rouland. “Computer-Based Training System for Cataract Surgery”. In: *International ICST Conference on Electronic Healthcare for the 21st Century*. 2010.

[Dum+11a] Elodie Dumortier, Stephane Cotin, Jeremie Dequidt, and Jean-Francois Rouland. “A Prototype of Simulation System for Cataract Surgery Training”. In: *European Society of Cataract and Refractive Surgeons Winter Meeting*. 2011.

[Dum+11b] Elodie Dumortier, Stephane Cotin, Jeremie Dequidt, and Jean-Francois Rouland. “Assessment Metrics For A Prototype Of Simulation System For Cataract Surgery Training”. In: *Annual Meeting of the Association for Research in Vision and Ophthalmology*. 2011.

[Dum+11c] Elodie Dumortier, Stephane Cotin, Jeremie Dequidt, and Jean-Francois Rouland. “Realisation d’un Prototype de Simulateur Fonctionnel pour la Chirurgie de la Cataracte”. In: *117e CONGRES de la Société Française d’Ophtalmologie*. 2011.

[Dur+16] Christian Duriez, Eulalie Coevoet, Frederick Largilliere, T Morales-Bieze, Zhongkai Zhang, Mario Sanz-Lopez, B Carrez, Damien Marchal, Olivier Goury, and Jeremie Dequidt. “Framework for online simulation of soft robots with optimization-based inverse model”. In: *Simulation, Modeling, and Programming for Autonomous Robots (SIMPAR), IEEE International Conference on*. Best Paper Award. 2016, pp. 111–118.

[Gou+16] Olivier Goury, Yann Nguyen, Renato Torres, Jeremie Dequidt, and Christian Duriez. “Numerical Simulation of Cochlear-Implant Surgery: Towards Patient-Specific Planning”. In: *International Conference on Medical Image Computing and Computer-Assisted Intervention (MICCAI)*. 2016, pp. 500–507.

[GD05] Laurent Grisoni and Jeremie Dequidt. “Asynchronous Interactive Physical Simulation”. In: *1st ICT Workshop on Virtual Reality*. 2005.

[GDC04] Laurent Grisoni, Jeremie Dequidt, and Christophe Chaillou. “Virtual Reality Applications and Frame-Rate Control”. In: *Development and Application Systems*. 2004, pp. 461–465.

[Hao+15a] Nazim Haouchine, Alexandre Bilger, Jeremie Dequidt, and Stephane Cotin. “Fracture in Augmented Reality”. In: *ACM SIGGRAPH 2015 Posters*. SIGGRAPH ’15. Los Angeles, California: ACM, 2015, 22:1–22:1.

[Hao+14a] Nazim Haouchine, Stephane Cotin, Jeremie Dequidt, Erwan Kerrien, Berger, and Marie-Odile. “Réalité augmentée pour la chirurgie minimalement invasive du foie utilisant un modèle biomécanique guidé par l’image”. In: *Actes de la conference RFIA 2014*. 2014.

[Hao+15b] Nazim Haouchine, Stephane Cotin, Igor Peterlik, Jeremie Dequidt, Mario Sanz Lopez, Erwan Kerrien, and Marie-Odile Berger. “Impact of Soft Tissue Heterogeneity on Augmented Reality for Liver Surgery”. In: *IEEE Transactions on Visualization and Computer Graphics* 21.5 (May 2015), pp. 584–597.

[Hao+13a] Nazim Haouchine, Jeremie Dequidt, Marie-Odile Berger, and Stephane Cotin. “Deformation-based Augmented Reality for Hepatic Surgery”. In: *Medicine Meets Virtual Reality*. 2013, pp. 182–188.

[Hao+15c] Nazim Haouchine, Jeremie Dequidt, Marie-Odile Berger, and Stephane Cotin. “Monocular 3D Reconstruction and Augmentation of Elastic Surfaces with Self-Occlusion Handling”. In: *IEEE Transactions on Visualization and Computer Graphics* 21.12 (Dec. 2015), pp. 1363–1376.

[Hao+14b] Nazim Haouchine, Jeremie Dequidt, Marie-Odile Berger, and Stephane Cotin. “Single View Augmentation of 3D Elastic Objects”. In: *Mixed and Augmented Reality (ISMAR), 2014 IEEE International Symposium on*. 2014, pp. 229–236.

[Hao+12] Nazim Haouchine, Jeremie Dequidt, Erwan Kerrien, Marie-Odile Berger, and Stephane Cotin. “Physics-based Augmented Reality for 3D Deformable Object”. In: *VRIPHYS - Virtual Reality Interaction and Physical Simulation*. 2012, pp. 31–38.

[Hao+13b] Nazim Haouchine, Jeremie Dequidt, Igor Peterlik, Erwan Kerrien, Marie-Odile Berger, and Stephane Cotin. “Image-guided Simulation of Heterogeneous Tissue Deformation For Augmented Reality during Hepatic Surgery”. In: *Mixed and Augmented Reality (ISMAR), 2013*

IEEE International Symposium on. Runner-up Best Paper Award. 2013, pp. 199–208.

[Hao+14c] Nazim Haouchine, Jeremie Dequidt, Igor Peterlik, Erwan Kerrien, Marie-Odile Berger, and Stephane Cotin. “Towards an accurate tracking of liver tumors for augmented reality in robotic assisted surgery”. In: *Robotics and Automation (ICRA), 2014 IEEE International Conference on*. 2014, pp. 4121–4126.

[JDC15] Zhifan Jiang, Jeremie Dequidt, and Stephane Cotin. “Détection de contours des organes pelviens dans des images médicales par modèles de B-spline”. In: *Congrès Français de Mécanique*. AFM, Association Française de Mécanique, 2015.

[Jia+14] Zhifan Jiang, Witz Jean-Francois, Lecomte-Grosbras Pauline, Jeremie Dequidt, Stephane Cotin, Christian Duriez, and Mathias Brieu. “Segmentation, Geometric Modeling And Motion Tracking For Evaluation Of Pelvic System Mobilities”. In: *International Conference on Experimental Mechanics*. 2014.

[Jia+17] Zhifan Jiang, Jean-Francois Witz, Pauline Lecomte-Grosbras, Jeremie Dequidt, Michel Cosson, Stephane Cotin, Christian Duriez, and Mathias Brieu. “Multi-organ Motion Tracking in Dynamic Magnetic Resonance Imaging for Evaluation of Pelvic System Mobility and Shear Strain”. In: *Strain* 53.2 (2017) (cit. on p. 88).

[Jia+18] Zhifan Jiang, Jean-Francois Witz, Pauline Lecomte-Grosbras, Jeremie Dequidt, Michel Cosson, Stephane Cotin, Christian Duriez, and Mathias Brieu. “Virtual Image Correlation of Magnetic Resonance Images for 3D Geometric Modelling of Pelvic Organs”. In: *Strain* 55.3 (2018), pp. 1230–5 (cit. on p. 88).

[Jia+15] Zhifan Jiang, Jean-Francois Witz, Pauline Lecomte-Grosbras, Jeremie Dequidt, Christian Duriez, Michel Cosson, Stephane Cotin, and Mathias Brieu. “B-spline Based Multi-organ Detection in Magnetic Resonance Imaging”. In: *Strain* 51.3 (2015), pp. 235–247 (cit. on p. 88).

[KBD08] Erwan Kerrien, Marie-Odile Berger, and Jeremie Dequidt. “Refining the 3D surface of blood vessels from a reduced set of 2D DSA images”. In: *Augmented environments for Medical Imaging and Computer-aided Surgery*. 2008, pp. 61–69.

[Ker+17] Erwan Kerrien, Ahmed Yureidini, Jeremie Dequidt, Christian Duriez, Rene Anxionnat, and Stephane Cotin. “Blood vessel modeling for interactive simulation of interventional neuroradiology procedures". In: *Medical image analysis* 35 (2017), pp. 685–698 (cit. on p. 77).

[Lar+15] Frederick Largilliere, Valerian Verona, Eulalie Coevoet, Mario Sanz-Lopez, Jeremie Dequidt, and Christian Duriez. "Real-time control of soft-robots using asynchronous finite element modeling". In: *Robotics and Automation (ICRA), 2015 IEEE International Conference on*. May 2015, pp. 2550–2555.

[Lec+13] Pauline Lecomte-Grosbras, Mouhamadou Nassirou - Diallo, Jean-Francois Witz, Damien Marchal, Jeremie Dequidt, Stephane Cotin, Michel Cosson, Christian Duriez, and Mathias Brieu. "Towards a better understanding of pelvic system disorders using numerical simulation". In: *Medical Image Computing and Computer-Assisted Intervention*. 2013, pp. 307–314.

[Mar+06] Damien Marchal, Fabrice Aubert, Christophe Chaillou, Laurent Grisoni, and Jeremie Dequidt. "Towards Cuttable Deformable Objects". In: *2nd ICT Workshop on Virtual Reality*. 2006.

[Rab+07] James Rabinov, Stephane Cotin, Jeremie Allard, Jeremie Dequidt, Julien Lenoir, Vincent Luboz, Paul Neumann, Xunlei Wu, and Steve Dawson. "EVE: Computer Based Endovascular Training System for Neuroradiolgy". In: *45th Annual Meeting & NER Foundation Symposium*. 2007, pp. 147–150.

[San+14] Mario Sanz-Lopez, Jeremie Dequidt, Erwan Kerrien, Christian Duriez, Marie-Odile Berger, and Stephane Cotin. "Testbed for Assessing the Accuracy of Interventional Radiology Simulations". In: *6th International Symposium on Biomedical Simulation (ISBMS)*. 2014, pp. 106–111.

[Sch+22] Pierre Schegg, Jeremie Dequidt, Eulalie Coevoet, Edouard Leurent, Remi Sabatier, Philippe Preux, and Christian Duriez. "Automated Planning For Robotic Guidewire Navigation In The Coronary Arteries". In: *IEEE 5th International Conference on Soft Robotics*. 2022 (cit. on p. 140).

[SDG12a] David Selosse, Jeremie Dequidt, and Laurent Grisoni. "A Sketch-Based Interface for Annotation of 3D Brain Vascular Reconstructions". In: *Computer Graphics International*. 2012.

[SDG12b] David Selosse, Jeremie Dequidt, and Laurent Grisoni. *A Sketch-Based Interface for Annotation of 3D Brain Vascular Reconstructions*. Tech. rep. 00698832. SHACRA (INRIA LNE / LIFL), 2012.

[Tal+15] Hugo Talbot, Nazim Haouchine, Igor Peterlik, Jeremie Dequidt, Christian Duriez, Herve Delingette, and Stéphane Cotin. “Surgery Training, Planning and Guidance Using the SOFA Framework”. In: *EG 2015 - Dirk Bartz Prize*. Ed. by H.-C. Hege and T. Ropinski. prize. The Eurographics Association, 2015.

[Wei+12] Yiyi Wei, Stephane Cotin, Jeremie Dequidt, Christian Duriez, Jeremie Allard, and Erwan Kerrien. “A (Near) Real-Time Simulation Method of Aneurysm Coil Embolization”. In: *Aneurysm*. InTech Publisher, 2012.

[Yur+11] Ahmed Yureidini, Jeremie Dequidt, Erwan Kerrien, Christian Duriez, and Stephane Cotin. “Computer-based simulation for the endovascular treatment of intracranial aneurysms”. In: *Living Imaging (Imaging and its applications in medicine and life sciences)*. 2011.

[Yur+12] Ahmed Yureidini, Erwan Kerrien, Jeremie Dequidt, Christian Duriez, and Stephane Cotin. “Local Implicit Modeling of Blood Vessels for Interactive Simulation”. In: *Medical Image Computing and Computer-Assisted Intervention*. 2012, pp. 553–560.

[Zha+19a] Zhongkai Zhang, Jeremie Dequidt, Junghwan Back, Hongbin Liu, and Christian Duriez. “Motion Control of Cable-Driven Continuum Catheter Robot through Contacts”. In: *Robotics and Automation (ICRA), 2019 IEEE International Conference on*. 2019.

[Zha+19b] Zhongkai Zhang, Jeremie Dequidt, Junghwan Back, Hongbin Liu, and Christian Duriez. “Motion Control of Cable-Driven Continuum Catheter Robot through Contacts”. In: *IEEE Robotics and Automation Letters* 4.2 (2019), pp. 1852–1859 (cit. on p. 135).

[ZDD18a] Zhongkai Zhang, Jeremie Dequidt, and Christian Duriez. “Vision-based Sensing of External Force for Soft Robots using Finite Element Model”. In: *Robotics and Automation (ICRA), 2018 IEEE International Conference on*. 2018, pp. 1529–1536.

[ZDD18b] Zhongkai Zhang, Jeremie Dequidt, and Christian Duriez. “Vision-based Sensing of External Force for Soft Robots using Finite Element Model”. In: *IEEE Robotics and Automation Letters* 3.3 (2018), pp. 1529–1536 (cit. on p. 129).

[Zha+16] Zhongkai Zhang, Jeremie Dequidt, Alexandre Kruszewski, Frederick Largilliere, and Christian Duriez. “Kinematic Modeling and Observer Based Control of Soft Robot using Real-Time Finite Element Method”. In: *IEEE/RSJ International Conference on Intelligent Robots and Systems*. 2016, pp. 5509–5514 (cit. on p. 129).

[Zha+17] Zhongkai Zhang, Thor Enrique Morales Bieze, Jeremie Dequidt, Alexandre Kruszewski, and Christian Duriez. “Visual Servoing Control of Soft Robots Based on Finite Element Model”. In: *IEEE/RSJ International Conference on Intelligent Robots and Systems*. 2017, pp. 2895–2901 (cit. on p. 129).

[Zha+19c] Zhongkai Zhang, Antoine Petit, Jeremie Dequidt, and Christian Duriez. “Calibration and External Force Sensing for Soft Robots using an RGB-D Camera”. In: *Robotics and Automation (ICRA), 2019 IEEE International Conference on*. 2019.

[Zha+19d] Zhongkai Zhang, Antoine Petit, Jeremie Dequidt, and Christian Duriez. “Calibration and External Force Sensing for Soft Robots using an RGB-D Camera”. In: *IEEE Robotics and Automation Letters* 4.3 (2019), pp. 2356–2363.

[Zha+22] Zhongkai Zhang, Antoine Petit, Jeremie Dequidt, and Christian Duriez. “SofaGym: An open platform for Reinforcement Learning based on Soft Robot simulations”. In: *Soft Robotics Journal* TBA.TBA (20x22), TBA (cit. on p. 140).

1

Interactive Physics-based Simulation

> *Dissimuler est feindre de ne pas avoir ce qu'on a. Simuler est feindre d'avoir ce qu'on n'a pas. L'un renvoie à une présence, l'autre à une absence.*
>
> — **Jean Baudrillard**
> Simulacres et Simulation

Physics-based simulation or computer simulation[1] is a standard tool for engineers and scientists. Thanks to the availability of computing technologies and their increasing performance, it has been widely used in many domains for the design and improvement of complex systems or to understand / predict natural phenomenon. For these kind of applications, the main target is accuracy because users want to be able to predict precisely what will happen in the *real world*. This accuracy is achieved by using complex physics models where the governing equations are highly non-linear and the parameters are numerous preventing to obtain an analytical solution of the problem. Numerical solutions are therefore sought after by discretizing the phenomenon in space and time leading to a high number of unknowns to solve. As a consequence, typical simulations in engineering exhibit high computation time or require clusters of computer to provide results in a reasonable time [Ste13].

Over the past decade I have been focusing my efforts in using computer simulation for medical applications. While scientific deadlocks related to general simulation still exist, modeling and simulating living tissues or organs raises specific challenges. First, the characterization of living materials is complex as few methods exist to perform harmless, ethical, non-invasive, in-vivo probing. Elastography [WMK06], an imaging technique that relies on the Doppler Effect to provide tissue movements or strain, may become the standard technology for biomechanical characterization but technological improvements are still needed to be effective. Second, properties of living materials exhibit lot of intra-variability (property is not constant in the whole material) and inter-variability (property is not constant for all beings). Third, experimental validation is also a challenging task and shares the same difficulties

---

[1] https://en.wikipedia.org/wiki/Computer_simulation

than characterization: the scarcity and the complexity to acquire data. To these intrinsic challenges, I also wanted that these computer simulations target specific medical applications: training simulators and computer-assisted software for surgery. Therefore this raises the need for interactive simulation that allows virtual interaction of a user on the simulation. Because this user can move, probe or manipulate the virtual models, this leads to unexpected solicitations on the model that cannot be pre-computed. Moreover the user expects the virtual simulation to immediately react after each of his/her actions as it will happen in a real surgical procedure. As a consequence, bounding computation time is the main has been another issue I have tackled in my research works.

The intent of the previous paragraphs was to provide a *big picture* of the large scope of scientific deadlocks that are related to computer simulation. My research activities in the field has been devoted to a much narrower spectrum. First of all, I have been mainly interested in mechanical / biomechanical modeling. Because most of living materials are soft and because some surgical devices are also soft, I have been working on the modeling on soft materials and the modeling of interactions between soft materials and rigid ones. Second to reduce the computational footprint or to provide the optimal trade-off between simulation accuracy and speed, I have worked on asynchronous strategies that ensure mechanical consistency while being less demanding with respect to computation power. Finally fast and accurate computer simulations require some work on software / hardware integration. The remaining of this chapter will present some scientific contributions on these different items to illustrate my work. It is not intended to be exhaustive as the reader will find a complete list of publications related to computer modeling and simulation at the end of the manuscript.

1.1 Motivations for Medical Procedures

Until the 1960's, Radiology was only used as a way to diagnose vascular diseases through angiography. In January 16, 1964, the first intervention (a dilatation of a stenosis) through Radiology was performed by Charles Dotter [RKK03]. *Interventional Radiology* became popular after that first initiative as an efficient way to treat vascular disease. It involves the insertion of thin flexible devices (*catheters* or *guidewire*) than are pushed in the vascular system until the reach of the targeted area and many pathologies can now be treated through this technique.

Fig. 1.1: Photography of a radiology intervention: thin flexible devices are inserted in the femoral artery and are navigated inside the vascular network until reaching the diseased area. Then different treatments can be performed. Monitoring the motion of the device in the patient is performed via X-ray imaging. Photography appears courtesy of www.dicardiology.com

Two decades later, surgical procedures have also faced a paradigm shift. The introduction of *laparoscopic cholecystectomy* (the surgical removal of the gallbladder) [BA11] encountered immediate acceptance by patients and surgeons. Compared to *open cholecystectomy* where a surgical incision of approximately 10 to 15 cm is typically made below the edge of the right ribcage, laparoscopic cholecystectomy only requires 4 small incisions (named *operating ports*) to let tubes of diameter from 5 to 10mm be inserted in the abdominal cavity. Theses tubes are then used to place instruments and a video camera in the patient belly.The surgeon monitors the procedure through a TV screen and acts by manipulating the instruments through the operating ports 1.2. This technique has retrospectively been proved to be safe and effective [BM94].

As a consequence and with the widespread of new technologies such as micro-instruments or imaging modalities, modern surgical procedures tend to be as less invasive as possible. Although this kind of surgery has tremendous advantages, offering quicker recovery, less pain, and greater safety, it presents new challenges for surgeons as they do not touch directly the patient but operate through specific (sometimes robotized) devices and have indirect visual feedback through video monitors. Because of this new complexity in medical procedures, medical institutions demand

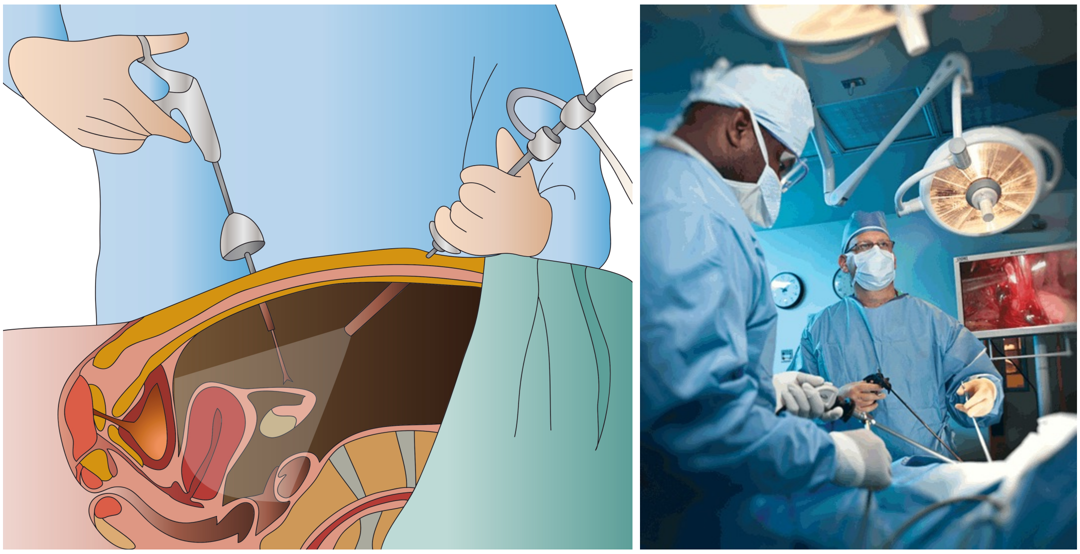

Fig. 1.2: Illustrations of laparoscopic surgery procedure: 4 small incisions are required to insert surgical instruments and camera (left). The surgeons then monitor the procedure on a video screen while manipulating the long thin surgical instruments (right). Left image appears courtesy of Sunshine Coast Advanced Laparoscopic Surgery, right image appears courtesy of www.chronogram.com.

new ways of training the interns before they face real patients. In that computer simulation is an ideal candidate as it provides a safe, reproducible, configurable, assessable test-bed and some simulators (classified as *Level-D simulators* by national aviation authorities) have already proven to be very effective for the training of pilots[2].

1.2 Simulation Overview

When applied to surgical procedures, computer-based training systems rely on a combination of hardware and software. Hardware usually include a computational system with visual system (from video monitor to stereographic system) and an acquisition device meant to mimic surgical devices. A popular acquisition device is a robotic arm that will track the user motion and will be able to provide force feedback when touching objects in the simulation. The software part is obviously a software that allow to integrate all the hardware devices and runs the virtual simulation. An example of such system is provided in Figure 1.3 which shows a training system for neuro-surgical procedures.

---

[2] https://en.wikipedia.org/wiki/Full_flight_simulator

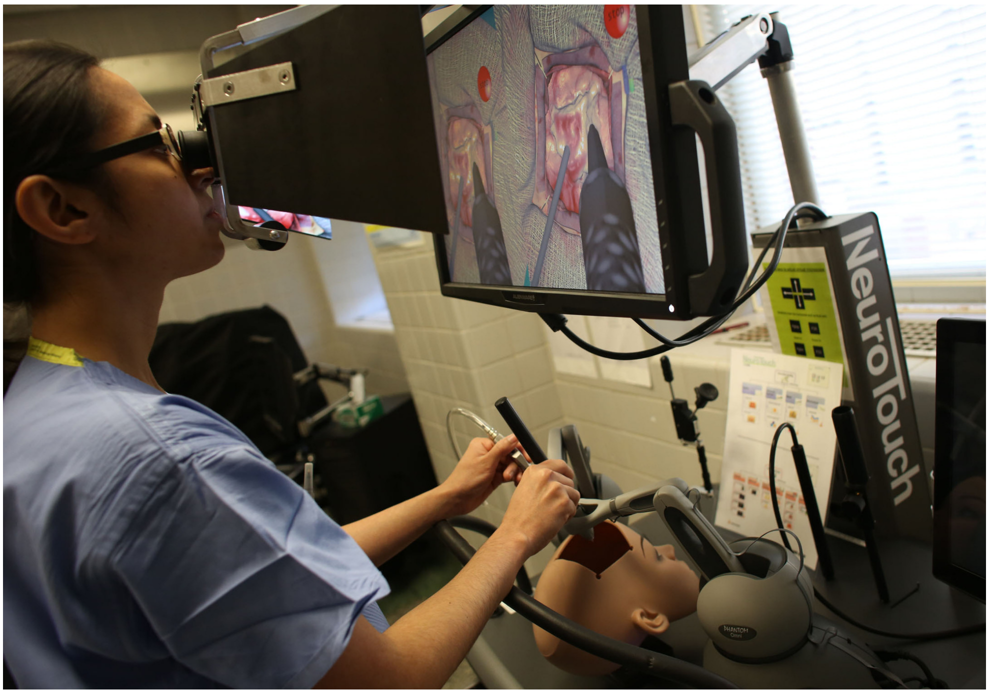

Fig. 1.3: Example of a neuro-surgical training system by Neurotouch©. The system includes robotic arm equipped with stylus (Geomagic© Touch) to acquire user gesture and to render forces in case of contact and a stereo-vision display to mimic the use of binoculars.

A computer software for bio-mechanical simulation can be summarized in a loop (called **Simulation Loop**) of 4 repeated steps 1.4: *Deformation Computation*, *Collision Detection*, *Contact Resolution* and *Rendering*. The *Deformation Computation* step aims at solving bio-mechanical equations in order to find out how the soft material has moved given specific forces applied to it. The *Collision Detection* step finds colliding (*touching*) or inter-penetrating (*object inside another*) objects involved in the simulation. Colliding objects can be virtual surgical tools manipulated by the user, therefore this step will acquire the current position of the tools. The *Contact Resolution* step will take care of these objects and will correct their position in order to provide a solution which is mechanically consistent and realistic. Forces will also be computed that can be sent to any force-feedback device. Finally the *Rendering* step is performed to provide a 3D / 2D / stereo visualization of the current state of the simulation. The *Deformation Computation* and the *Contact Resolution* steps rely on mechanical equations while the *Collision Detection* step relies on geometric algorithms. The *Rendering* step relies on Computer Graphics techniques and will not be addressed in this manuscript as I do not have proposed any original contributions in this field.

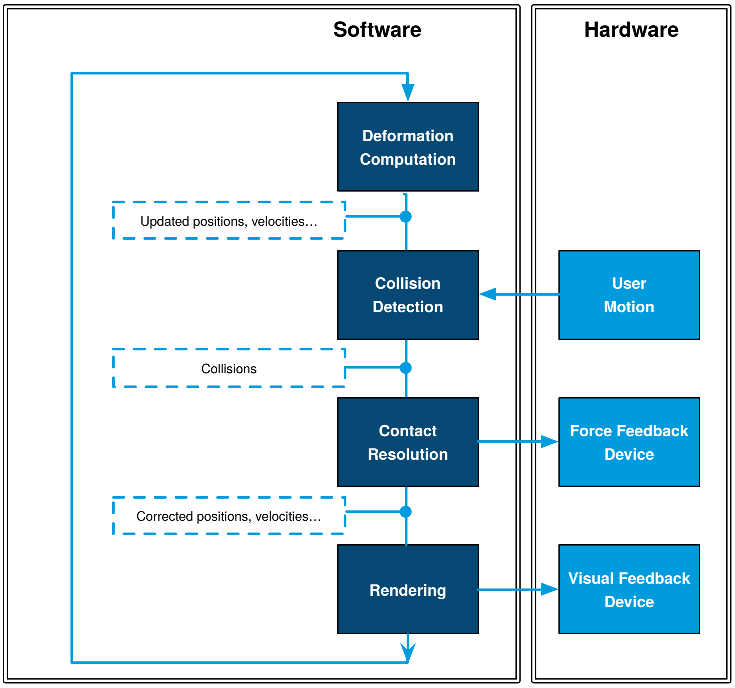

Fig. 1.4: A simplified overview of the simulation loop for bio-mechanical applications. These 4 steps are repeated to produce feedbacks (visual, haptic, audio…) to the user.

This simulation loop complies with several technical constraints (stability, robustness…) but the most important constraint is induced by the user acting on the simulation. It implies that first, very few hypotheses on the motion / gesture of the user can be made and second, the simulation should react *fast enough* to look realistic and comfortable for the user. Thus, acceptable visual feedback rates are between 30 Hz and 60 Hz while haptic feedback are usually between 300 Hz and several kHz [FU06]. This means that the simulation software should output a new image every [16-33] milliseconds and a new force every [1-3] milliseconds which imposes high-performance computation on the simulation or to choose an adequate trade-off between accuracy and computation speed.

The core of any computer-training system for surgery is the computation of the deformation and the mechanics of deformable solids is quite a large topic [Dog13]. Computational models for deformable solids are a very active research field in the mechanical engineering and computer graphics communities. The concerns in computer graphics community focus on controlling the computational footprint and the ease of implementation and versatility [Nea+06]. Deformable solids are governed by the equation of the dynamics (Newton's second law of motion):

$$\mathbf{M}\dot{\mathbf{v}} = \mathbf{f}^{\text{ext}} - \mathbf{f}^{\text{int}}(\mathbf{q}, \dot{\mathbf{q}}) + \mathbf{H}^{\text{T}}\lambda \tag{1.1}$$

where $\mathbf{q} \in \mathbb{R}^n$ is the vector of generalized degrees of freedom of the solid, $\mathbf{q}$ represents the velocity, $\mathbf{M}$ is a mass (intertia) matrix, $\mathbf{f}^{ext}$ and $\mathbf{f}^{ext}$ are respectively the vectors of the external and internal forces. $\mathbf{H}^{\text{T}}\lambda$ gathers the constraint forces contributions, this later term will be detailed later. Forces $\mathbf{f}^{\text{int}}(\mathbf{q}, \dot{\mathbf{q}})$ are expressed as a function of the position of the solid and its velocity. Solving this equation analytically can be achieved on limited, special cases. When dealing with solids with arbitrary shapes and position-dependent forces, this equation requires a numerical approach to be solved. Thus the time-line is discretized as a set of time intervals for which the deformation will be computed. The temporal discretization is chosen according to the time constraints imposed by visual and/or haptic feedbacks. A fixed period (labeled h) is considered between time-steps whose value is usually between 1 milliseconds to 50 milliseconds. Integration of equation (1.1) over a time interval $[t, t+h]$ leads to:

$$\begin{gathered} \int_t^{t+h} \mathbf{M}\dot{\mathbf{v}}dt = \int_t^{t+h} (\mathbf{f}^{\text{ext}} - \mathbf{f}^{\text{int}}(\mathbf{q}, \dot{\mathbf{q}}) + \mathbf{H}^{\text{T}}\lambda)dt \\ \mathbf{M}(v_{t+h} - v_t) = h(\mathbf{f}^{\text{ext}}_{t+h} - \mathbf{f}^{\text{int}}(\mathbf{q}_{t+h}, \dot{\mathbf{q}}_{t+h}) + \mathbf{H}^{\text{T}}\lambda_{t+h}) \end{gathered} \tag{1.2}$$

Subscript t and $t+h$ have been added to explicitly indicate when equation variables are considered. We use implicit (or backward) Euler method that states for any ordinary differential equation $\frac{\mathrm{d}y}{\mathrm{d}t} = f(t, y)$, the sequence of approximations are built using: $y_{k+1} = y_k + hf(t_{k+1}, y_{k+1})$. Then we can write that: $\mathbf{q}_{t+h} = \mathbf{q}_t + h\mathbf{v}_{t+h}$. Since internal forces are non-linear functions of the degrees of freedom and their velocities, we apply a Taylor series expansion and make the first order approximation (a single linearization by time-step):

$$\mathbf{f}^{\text{int}}(\mathbf{q}_{t+h}, \dot{\mathbf{q}}_{t+h}) \approx \mathbf{f}^{\text{int}}(\mathbf{q}_t, \dot{\mathbf{q}}_t) + \frac{\partial \mathbf{f}^{\text{int}}}{\partial \mathbf{q}}\mathrm{d}\mathbf{q} + \frac{\partial \mathbf{f}^{\text{int}}}{\partial \dot{\mathbf{q}}}\mathrm{d}\dot{\mathbf{q}} \tag{1.3}$$

Combining equations 1.2 and 1.3 and posing $d\mathbf{q}$ as $\mathbf{q}_{t+h} - \mathbf{q}_t$ (which also equals to $h\mathbf{v}_{t+h}$), we obtain the following equation:

$$\left(\frac{\mathbf{M}}{h^2} + \frac{\partial \mathbf{f}^{int}}{\partial \dot{\mathbf{q}} h} + \frac{\partial \mathbf{f}^{int}}{\partial \mathbf{q}}\right)\mathrm{d}\mathbf{q} = \mathbf{f}^{\text{ ext}} - \mathbf{f}^{\text{ int}}(\mathbf{q}_t, \dot{\mathbf{q}}_t) + \left(\frac{\mathbf{M}}{h} - \frac{\partial \mathbf{f}^{\text{ int}}}{\partial \dot{\mathbf{q}}}\right)\dot{\mathbf{q}}_t + \mathbf{H}^{\text{T}}\lambda \tag{1.4}$$

Fig. 1.5: Examples of manufactured surgical devices than can be modeled as one-dimensional solids: Surgical Thread (®AD Surgical), Endoscope (®International Light Technologies), Catheter (®Paralogic), Detachable coil (®MedTronic)

which is a linear system of equations $\mathbf{A}\mathrm{dq} = \mathbf{b}$ where terms $\mathbf{A}$ and $\mathbf{b}$ are estimated at each time-step and are specific to the mechanical model of the solid and the constraints we consider. Solving this linear system enables to compute the motion and the deformation of the solid over the time of simulation. We will detail in the following section how this equation could be applied to simulate a one-dimensional deformable object.

1.3 1D Mechanical Model

We choose to detail in this manuscript our contributions about one-dimensional deformable models. From an *application* standpoint, one-dimensional model can be used to simulate a large variety of objects in surgical training systems (see figure 1.5 for some devices): for instance surgical thread (for suturing tasks), minimally invasive or endovascular devices such as endoscopes, catheters but also anatomical structures such as blood vessels, ligaments or fiber muscles. And from *modelling* and *simulation* standpoints, it raises some of the challenges related to characterization and computational optimization.

In the clinical context of interventional radiology, detachable coil embolization is a a minimally invasive procedure to treat aneurysm[3] 1.6 where the vascular network is used as a medium to reach the disease vessel. The interventional radiologist starts by inserting a catheter (a long, thin and flexible tube) into the femoral artery. This catheter is then manipulated through the arterial system until the aneurysm location is reached. When complex branchings occur, a guidewire (a long, thin wire, stiffer than a catheter) can be inserted inside the catheter to help reaching the desired artery. Once in position, the physician places one or more small coils through the catheter

---

[3] An aneurysm often consists in an abnormal bulge that appears close to branching arteries

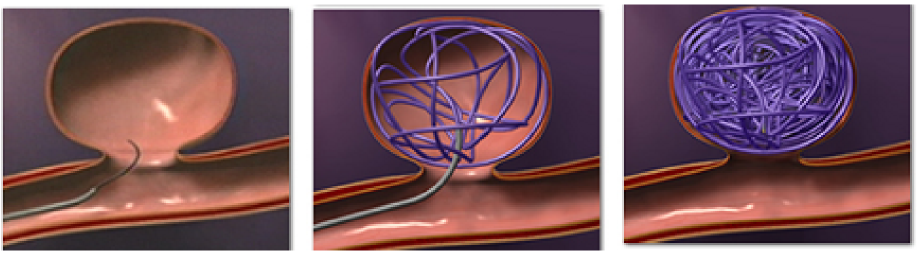

Fig. 1.6: Example of a coiling procedure in an aneurysm (blood vessel bulge): a thin wire (coil) is inserted in the aneurysm reducing the blood flow thus the blood pressure and allowing the blood to clot.

Fig. 1.7: Examples of the diversity of manufactured detachable coils used in interventional radiology. Length, diameter and shapes (helical, 3D, 360 degrees) may differ and are used given the pathology encountered.

into the aneurysm. The body responds by forming a blood clot around the coil, thus blocking off the aneurysm and considerably reducing the risk of rupture. Although coil embolization is less invasive than open surgery, and allows treatment of cerebral aneurysms that previously were considered inoperable, such procedures are very difficult to perform and require an important experience from the interventional radiologist. This is particularly true when treating brain aneurysms, where any mistake occurring during the coil deployment or when reaching the aneurysm could lead to a brain hemorrhage. Yet, even in the case of a successfully performed procedure, the choice of the coil plays a key role in the long term success of the procedure. Most of them have a core made of platinum, and are sometimes coated with another material or a biologically active agent and their principle characteristics are the shape, the length, the diameter (see figure 1.7). All types are made of soft platinum wire of less than a millimeter diameter and therefore are very soft. The softness of the platinum allows the coil to conform to the often irregular shape of the aneurysm, while the diameter, length and shape of the coil are chosen based on the shape and volume of the aneurysm, as well as the size of the neck of the aneurysm. In most cases, several coils are required to completely fill the aneurysm and maximize the chances to clot (see figure 1.8).

Fig. 1.8: Aneurysm coiling requires several coils to fill the aneurysm in order to reduce the blood flow and thus prevents the aneurysm from rupturing. Image courtesy of Stryker Neurovascular.

1.3.1 Contributions

Given this clinical context, we proposed a model for simulating very thin and flexible devices such as coils. An original approach was also introduced for describing the complex rest shape of coils. Co-axial insertions of endovascular devices (coil inside a micro-catheter for instance) are achieved using a *composite model*, which is based on a geometric combination of the characteristic rest shapes of each model. This composite model allows to use a single model to simulate several instruments together and then saves the computational burden of having several interacting objects to simulate.

The proposed model uses a series of serially linked beam elements, similarly as proposed by Duriez et al. [Dur+06] for simulating catheters and guidewires. A beam element, as introduced by Przemieniecki [Prz68] allows to model mechanically a piece of curve that can handle bending, stretching and twisting. Both extremities of the beam are called *nodes* and are described by six degrees of freedom, three of three of which correspond to the spatial position, and three to the angular position of the node in a global reference frame (see figure 1.9a). An elementary stiffness matrix $\mathbf{K_e}$ is a 12×12 symmetric matrix that relates spatial and angular positions of each end of a beam element to the forces and torques applied to it. The notable parameters of the matrix $\mathbf{K_e}$ are the mechanical properties of the beam (E the Young's modulus and ν the Poisson's ratio) and the geometric properties of the beam (length, cross-section area and cross-section moments of inertia). The reader may refer to [Dur+06] or [Prz68] for more details about the construction of $\mathbf{K_e}$ given these parameters.

In the reference frame, only deformations (bending, torsion, elongation) are measured. A transformation matrix $\mathbf{\Lambda}$ is then defined to change the local frame of reference to a global coordinate system. This leads to the following relationship between $\overline{\mathbf{K}}_{\mathbf{e}}$ in local coordinates and $\mathbf{K}_{\mathbf{e}}$ in a global frame:

$$\mathbf{K}_{\mathbf{e}} = \mathbf{\Lambda}^T \overline{\mathbf{K}}_{\mathbf{e}} \mathbf{\Lambda} \tag{1.5}$$

As the beam deforms, only $\mathbf{\Lambda}$ changes and needs to be recomputed, while $\overline{\mathbf{K}}_{\mathbf{e}}$ remains constant, as long as the deformation of the beam in its local frame remains small. To model a complex structure such as a coil, which undergoes large displacements, we need to discretize it as a series of beam elements to ensure that each beam deformation will remain small (see figure 1.9). For the entire structure describing a catheter or guidewire, the global stiffness matrix $\mathbf{K}$ is recomputed, at each time stetp, by summing the contributions of each beam element, through its elementary stiffness matrix $\mathbf{K}_{\mathbf{e}}$. Assuming lumped masses at the nodes, the mass matrix $\mathbf{M}$ is a diagonal matrix. A damping matrix $\mathbf{D}$ is also introduced as a linear combination of the stiffness and mass matrices $\mathbf{D} = \alpha\mathbf{M} + \beta\mathbf{K}$, known as Raleigh damping. This leads to express the internal forces from equation 1.2 as:

$$\mathbf{f}^{\text{int}}(\mathbf{q}, \dot{\mathbf{q}}) = \mathbf{D}\dot{\mathbf{q}} + \mathbf{K}\mathbf{q} \tag{1.6}$$

However, we introduce several modifications to take into account for the particular nature of interventional devices. Boundary conditions are specified by defining a particular translation or rotation for the first node of the model to represent user control of the device (the coil is manipulated by pushing and twisting a wire). Even if $\overline{\mathbf{K}}_{\mathbf{e}}$ is a linear approximation of Hooke's law, our model can handle large displacements: given an initial configuration of a beam, a current deformed one and a reference frame of the first extremity, the beam theory defines the way the local frame of the second extremity will be updated. Since the first node of the model is constrained, the first beam equation will be used to update the local frame for the second node, thus allowing the second beam to be computed in a reference frame where no rigid transformation occurs. By repeating this process through the whole structure, we can compute $\mathbf{\Lambda}$ for each beam element and therefore determine $\mathbf{K}_{\mathbf{e}}$. This method is closer to the co-rotational approach [Fel00] than the incremental approach proposed in [Dur+06] and permits to model the geometric non-linearities that occur during the deformation of the coil.

Devices such as catheters, guide-wires and coils are not subject to elongation but mainly bending and twisting. They are also characterized by their rest shape, which plays a very important role in the delivery of the therapy. We model these complex shapes by changing the local frame at each node of the model, as illustrated in figure

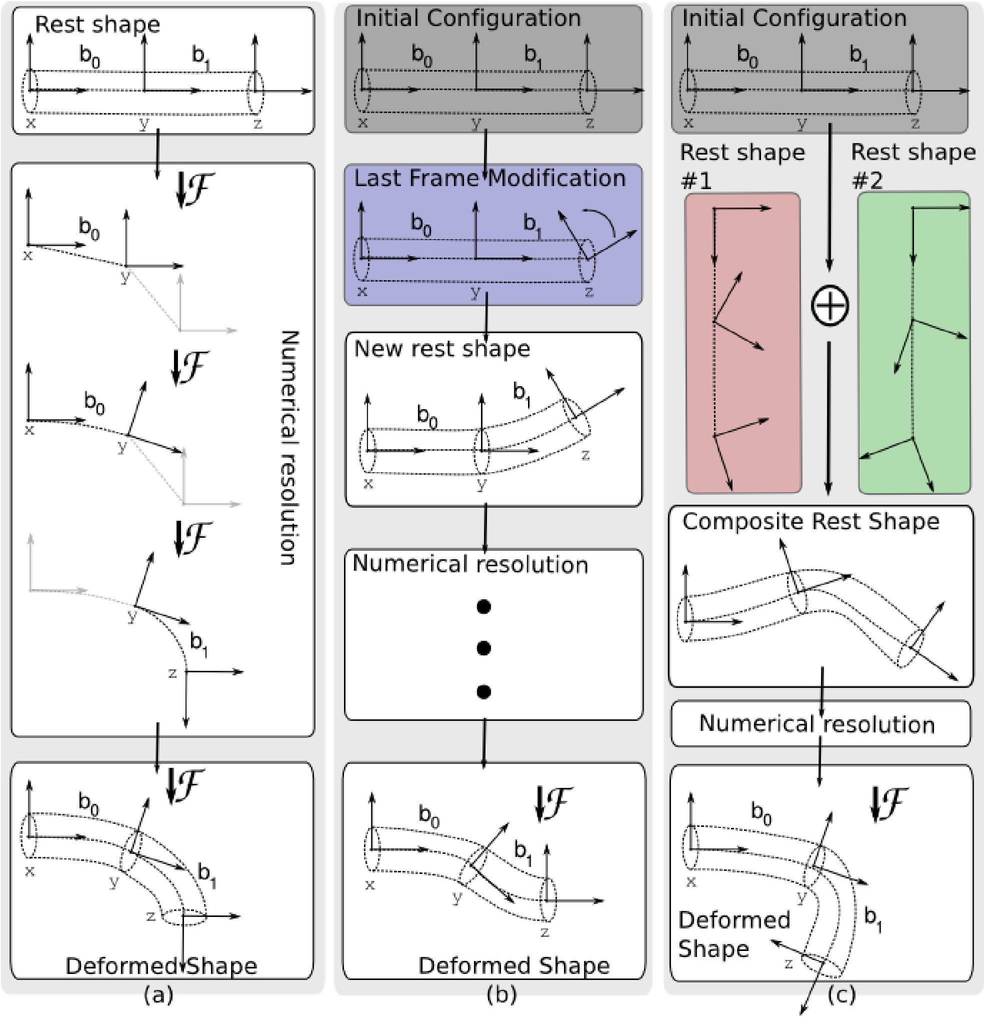

Fig. 1.9: Modeling of a wire using linked beam elements. (a) Given an initial rest shape and forces applied on DOFs, internal forces are computed using a local reference frame to handle large deformations. Starting from the first beam, reference frames are updated to suppress rigid transformation from the expression of the beam deformation. (b) Modification of the initial shape by moving frames or positions allows the generation of various deformed shapes. (c) A composite model (co-axial combination of two wires) is obtained by geometrically mixing different rest shapes on one geometric model.

1.9b. Obviously, an important feature is to dynamically modify theses frames at run-time to describe more complex behaviors. For instance, to simulate a coil being deployed from a micro-catheter, we avoid computing the complex interactions the take place between the coil and the micro-catheter. Instead we propose to simulate this behavior by using a composite model. The Halpin-Tsai [HK76] equations provide a framework to update mechanical properties of a reinforced fiber. This approach was applied to the simulation of catheters and guide-wires by Lenoir *et. al.* [Len+05]. We propose an extension of this framework to take into account two or more local frames and combine them using weighted sum (see figure 1.9c):

$$q_{cmp} = \frac{q_1 E_1}{E_1 + E_2} + \frac{q_2 E_2}{E_1 + E_2}$$

where each q_i is the quaternion representing the transformation from local frame global frame and E_i represents the beam Young modulus of the considered rest shape. As a consequence, such weighted sum will give more influence on the final composite shape to stiff materials.

From an optimization standpoint, it is worth mentioning that since all beam elements are serially connected, the resulting stiffness matrix $\mathbf{K}$ is a tridiagonal matrix with a band size of 12 (since each $\mathbf{K_e}$ is a 12×12 matrix). Since the mass and damping matrices are also diagonal, we solve the linear system using the algorithm proposed by Kumar *et al.* [KP93]. The solution can be obtained in $O(n)$ operations instead of $O(n^3)$. This allows to drastically reduce the computational footprint of the system resolution.

1.3.2 Coil Deployment in Collision-Free Environment

In order to validate our one-dimensional model, we want to compare our simulation against real data. However, exact mechanical properties of coils are difficult to obtain since they are not shared by device manufacturers. Among the parameters required to simulate our coil model, some of them are usually provided, such as coil length, diameter of the cross section and possibly some hints about the rest shape (circle diameter for helical-shaped coil for instance). Other parameters such as mass, Young's modulus and Poisson's ratio can be found in mechanical engineering handbooks. Coils are made of platinum and other materials such as titanium, giving us an initial guess for what Young modulus and Poisson ratio values to use. Eventually, the rest shape is the decisive parameter we need to identify because this feature is very important for embolization coils.

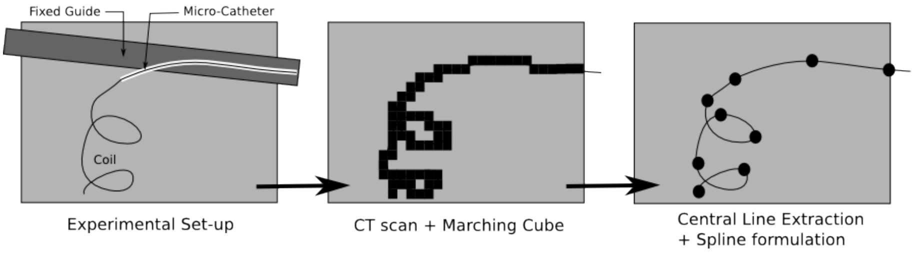

Fig. 1.10: Experimental setup: (a) the coil is deployed in a contact-free environment. (b) Volumetric data is obtained by 3DXA and a marching cube is performed to get a mesh of the real coil. (c) Central line of the coil is extracted and a continuous formulation is built using splines.

In order to estimate these missing parameters we build an experimental setup that consists of a box filled with water and a transversal fixed guide, defining the path for the catheter. The catheter is first introduced, followed by the helical coil as in the real procedure. The three-dimensional shape of the coil at different stages of the deployment is obtained from 3DXA (3D X-ray angiography) images using a marching cubes algorithm. The different steps of the experiment are illustrated in figure 1.10. In these experiments, the coil is only subject to a gravity force, and contacts with the box were avoided.

Once the real coil positions have been tracked and the shape segmented for three different stages of the coil deployment, an algorithm using a B-spline formulation was applied to the real coil data to obtain a continuous description of the shape. Given this dataset, we run an optimization (brute-force gradient descent) algorithm to estimate the rest shape of the coil as well as mechanical parameters. A validation of the coil simulations is reported in the next table for three different stages of the deployment. Then, simulations of the coil were performed using the same boundary conditions as measured during the actual coil deployment. In order to compare our simulation with the actual data, the B-spline curve was discretized using the same number of points as the number of nodes in the simulation. The error metric used to validate the coil simulation is the relative energy norm error [ZZ87]. The metric is defined as the ratio of the displacement between the simulated and the real coil and the real displacement. The error is computed for each node and for the three different steps of the deployment. The results are given in table 1.1. The relative energy norm error is small and exhibits that our simulation is close from real data. The absolute mean distance between simulated and real positions after deployment is equal to $1mm$ for each stage, explaining why the error increases if the coil is deployed on a small length. An illustration comparing the simulated coil and the real coil is proposed in the figure 1.11 showing the accuracy of the model.

	Relative Energy norm error	Mean total displacement
	Average % (SD)	(mm)
Stage 1	9.80% (4.05)	18.2
Stage 2	6.19 % (5.05)	24.99
Stage 3	4.17 % (1.42)	39.11

Tab. 1.1: Error measurement. The average and the standard deviation (SD) of the relative energy norm error are given in percentage in the first column. The second column contains the mean displacement of the coil for the three different steps.

Fig. 1.11: Visual comparison of our coil simulation (in red) with the reconstructed coil model from our experiments (in yellow) at different stages of the deployment. Quantitative errors are available in table 1.1.

1.4 Asynchronous Simulation

Given mechanical models for deformable solids, simulation of these models can be included in a single virtual reality environment. In the context of medical simulations, a common scenario considers a set of soft anatomical structures (soft tissues, organs, blood vessels. . .) which are manipulated or cut by surgical devices. Compared to these anatomical structures, the surgical devices appeared to be much stiffer and can sometimes be modeled as rigid objects (for micro-surgical blades for instance). But some devices like catheters, guide-wires or surgical threads, while being composed of stiff materials, are thin enough to be bended and might be subject to high-speed deformations or vibrations. Combining *soft* and *stiff* objects in a simulation raises a computational issue:

- *stiff* objects are usually simulated with dedicated models (such as described in section 1.3) and are composed of several degrees of freedom (DOFs). They can be therefore simulated interactively with a small time-step to capture the deformations occurring at high-frequency.
- *soft* objects are built with generic FEM models with a large number of DOFs mainly because of the number of geometric primitives used to describe their arbitrary shapes. They therefore require a large time-step to be simulated interactively.

Having the two objects interacting in the same simulation, like the *stiff* needle puncturing the *soft* liver, requires the objects to share a single time-line and cannot be simulated in parallel. Such an approach can be acceptable in the case where the simulation is not required to be run in a real-time: in this case a small simulation time step is chosen to account for the high frequencies in the needle response. Thereby, it's assumed that it will run much more slowly than the real clock time, as in each small time-step, the costly dynamics of the bulky soft objects has to be recomputed.

In the context of interactive simulations, such a solution cannot be considered. The strategy we have proposed is a multi-rate approach where dynamics of each object in the scene is integrated in real-time with its own time-step. This approach is especially suited for simulations with haptic rendering. In this case, the dynamics of the stiff object (e.g. the flexible needle) which does not require heavy computations can be simulated in the haptic loop running usually at 1000Hz, while the dynamics of the soft highly-deformable body (e.g. the liver) is simulated on a much lower (typically synchronized with the visual thread running about 30 or 60Hz), since it requires more computationally expensive calculations. This approach was already studied for example in our previous works such as [DGC05a] where the objects were simulated at different frequencies, however, at the cost of simplification in modeling the interactions. The contributions we present in this sections are based on [PDC11] where a method allowing for multi-rate interactive simulation of objects simulated at two different frequencies has been proposed. However, the method was suitable only for a quasi-static scenario: it required that compliance matrices needed to simulate the interactions between the objects do not depend on time step.

Our framework relies on simulation loops running at different frequencies. A simple explanation of our strategy can summarized as follows: time-consuming operations will be performed in the low-rate simulation loop while fast computations will be performed in the high-rate loop:

- *low-rate loop*: unconstrained motions, proximity queries,
- *high-rate loop*: unconstrained motion (stiff objects), constraint solving (violation evaluation, compliance computation, resolution, corrective motion), haptic-force computation

The details and more specifically the equations are detailed in [Der+13] but we want to emphasize on the following features. The models of both stiff and soft objects are linked by the constraint based expression of their mechanical interactions. Among the interactions between the two deformable bodies, we need to detect the collision and provide an adequate response (without inter-penetration). The collision detection (or more generally the geometrical determination of the contact points) is often time consuming and is not compatible with the high rate loop. In our approach, we use an algorithm based on proximity queries between meshes that is computed in the low rate loop. It supposes that we have access to a geometrical position of the stiff object in this low rate loop. The algorithm places contact constraints where the local minimal distance between the meshes is small enough to have a potential collision between current time t and $t + h$. Other type of constraints, for instance bilateral constraints (attachment, sliding...) can also be set. After computing the queries, a matrix $\mathbf{H}$ (see equation 1.1) containing the directions of unilateral and bilateral constraints for each object is assembled. To solve the reaction forces related to constraints, we first to need evaluate the constraint violation when applying an unconstrained dynamic motion to both deformable objects (i.e. solving equation 1.1 with λ set to 0). This unconstrained motion is also called *free motion* and allows to obtain the constraint violation δ^{free} (which is computed at low and high rates). Solving a MCP (mixed complementarity problem) allows to find the final constrained positions.

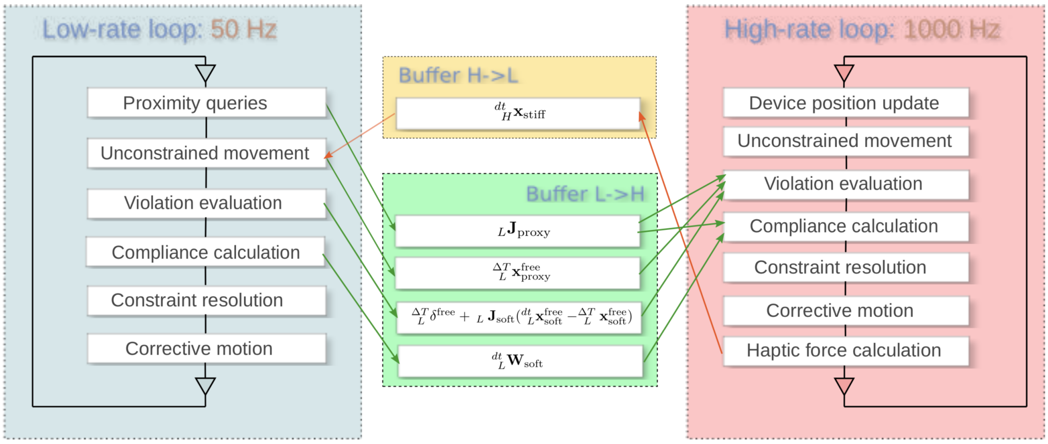

Fig. 1.12: Asynchronous simulation: details on the steps performed by the two loops that run at different frequencies. The central blocks represent shared buffers that are needed to compute mechanical interactions.

To validate this method, we created a simulation scene where a cylinder is placed on a horizontal plane. The cylinder is modeled by tetrahedral corotational FEM and is simulated at 50 Hz. A wire is attached to the upper part of the cylinder and the other endpoint of the thread is driven by a haptic device as shown in figure 1.13. The wire is modeled with 10 serially-linked beam elements based on Tymoshenko formulation and its dynamics is computed at 1000 Hz. The collisions between the plane, cylinder and the thread are being detected and resolved during the simulation. During the interaction, the simulation remains stable for any admissible configuration: the position of the cylinder on the plane can be changed by pulling the wire, or the cylinder can be even pulled out of the plane, so it's hanging freely in the space been hung on the wire. At the same time, a detailed and realistic haptic force-feedback is delivered to the user.

1.5 Applications: Medical Simulators

The methodology employed through this chapter has been applied to other scientific problems related to mechanical modeling or simulation interactivity. In order to illustrate the potential and the relevance of the contributions, we have built several proof-of-concept medical applications that rely on interactive simulations. Some have been a necessary step to open new collaborations or to build more ambitious projects and other have been transfered to start-up companies to be commercialized. In this section, we will focus on two specific applications: first, a simulator to train

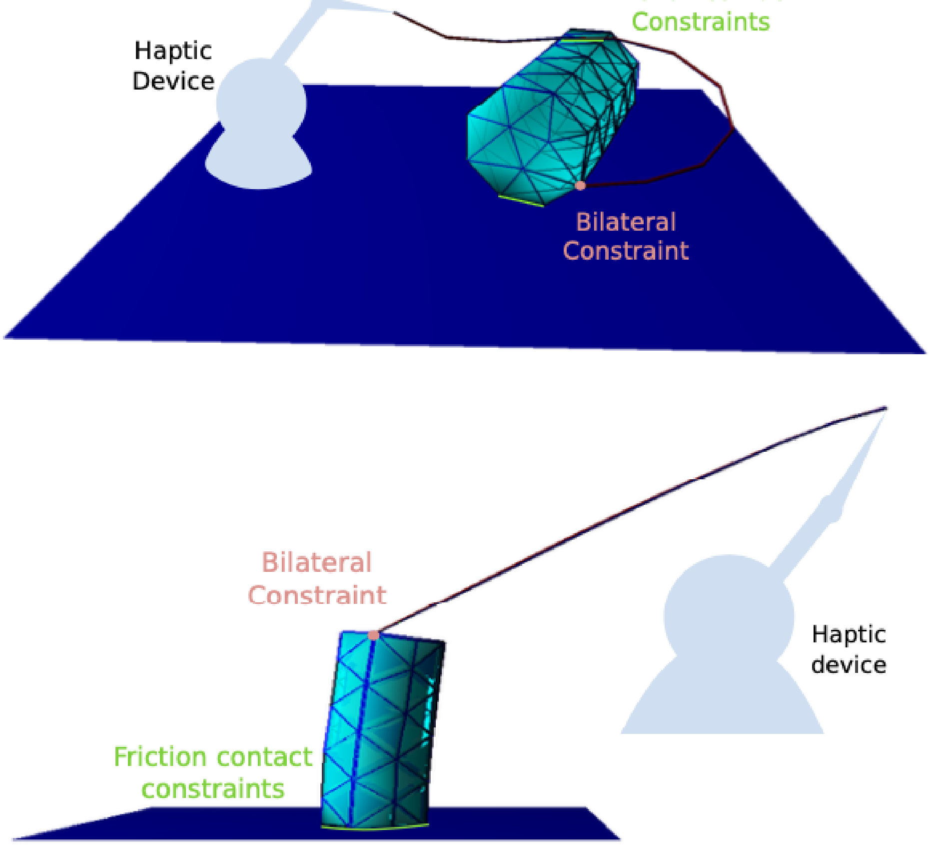

Fig. 1.13: Simulation of a deformable cylinder (simulated at 50 Hz) and a thread (simulated at 1 kHz) interacting with a solid plane.

cataract surgery procedure and second, an application that help radiologists to plan coiling interventions.

1.5.1 Training System

The development of a training system for opthalmology has been a good opportunity to showcase the various contributions in interactive simulation while strengthening a collaboration with the CHRU of Lille that has proven to be very fruitful.

When designing the simulator, our objectives were:

1. be able to train on the three most important steps of the procedure: capsulorhexis, phacoemulsification, and intra-ocular lens injection which has not, to our knowledge, been treated previously

2. develop advanced models based on biomechanics that can be easily parametrized using material properties and that can be computed quickly

3. have a working environment and devices as close as possible to real operating rooms.

System overview

The environment consists in a microscope where stereo glasses have been fixed in order to render the virtual scene in 3D, a full-body mannequin where replaceable silicon eyes that support cataract surgery may be inserted. Monitors are also available in the room to provide additional informations (like vital constants) or feedbacks. This serves a pedagogic purpose because it increases the feeling of immersion while allowing to train and memorize the real procedure with the same devices (microscope, pedals. . .) and the same surgical tools design using rapid prototyping. The tools are tracked in real-time and their 3D position is used to feed our real-time simulation. Figure 1.14 illustrates the various components that are part of the training system and how their are connected.

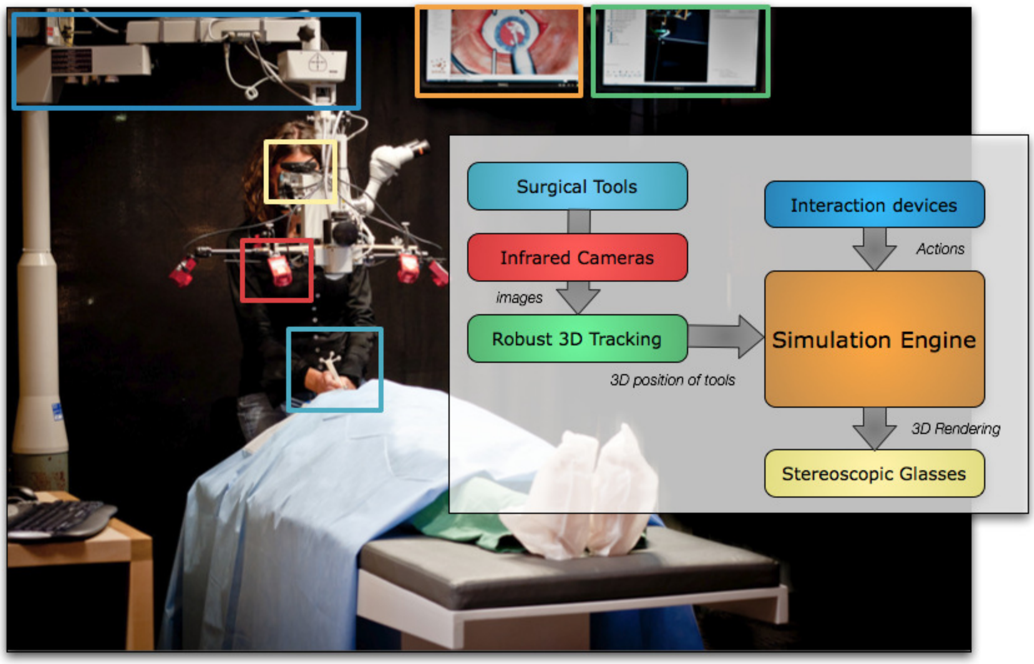

Fig. 1.14: Functional view and picture of the training system. The system relies on devices used in real procedures (microscope, pedals...), replicas of surgical tools that are tracked in real-time and on a simulation engine that renders a realistic and interactive simulation of cataract surgery.

Interaction Devices Real surgical tools could have been used to interact with the simulation, however they suffer from two important drawbacks. First they are expensive and second they are metal-based which makes the tracking more difficult and lower the accuracy (diffuse reflection area may appear on the images). Therefore, the use of replicas of surgical tools based on polyamide (nylon) was made. They were first modeled using standard CAD software and then were built using fast prototyping. Figure 1.15 shows the comparison between some of the real surgical tools and the ones used in our simulation. Reflective markers may disturb the clinician, especially for grasping tasks, but the markers are carefully placed to limit disturbance.

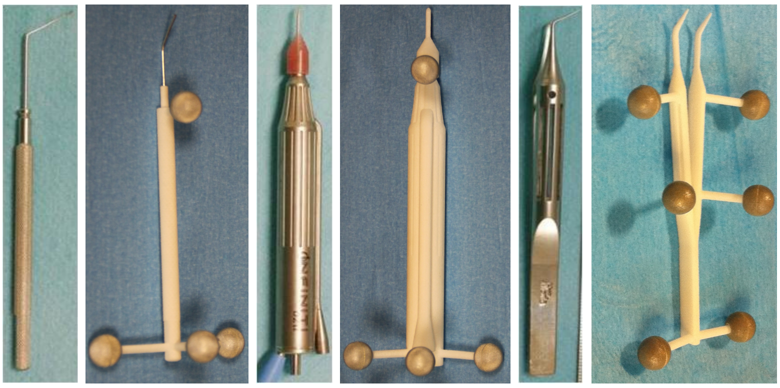

Fig. 1.15: Examples of tools used in cataract surgery and the ones we built for interacting with the simulation. From left to right: the phaco chopper, the phacoemulsification hand-piece and the capsulorhexis forceps.

Robust 3D Tracking Our setup includes six infra-red cameras that targets the area around the eye. Two cameras may be sufficient to provide a 3D tracking but this is not a robust set-up. Indeed, intensive manipulations in that area may completely or partially hide instruments preventing the real-time tracking to work. With six cameras, the operative area is well covered and during any step of the procedure at least two cameras are able to track the instruments. The setup is shown on figure 1.16. The redundancy involved with the six cameras make the calibration more time-consuming but once it has been performed, the tracking algorithm is able to provide 3D position of markers in real time. We are also using a feature proposed by *Tracking Tools*[4] software which allows to track rigid bodies. Each rigid body is defined as a set of reflective markers and the distance between markers do not change over time and the tracking is then more simple. Three markers may be sufficient to define a 3D position but again for robustness issues, we introduce redundancy by placing four markers on the instrument. Using different *signatures*

---

[4] `http://www.naturalpoint.com/optitrack/products/tracking-tools/`

(*e.g.* the way markers are placed on the tools), we can manage to track several tools simultaneously (see figure 1.17) which is a prerequisite for several steps of the cataract surgery procedure.

For a better balance of the computation power needed to run our simulation system, two computers are used. The first one, which does not require large computational resources, is connected to the cameras and runs the tracking software while the second one runs the simulation engine. The two computers shared tracking informations by using the VRPN library[5] which is a lightweight and low-latency client-server protocol dedicated to virtual reality applications. The simulation engine is therefore on a single computer (with high-performance graphics cards) and can provide fast response to user inputs.

Fig. 1.16: Overview of our setup: mannequin and microscope where 6 infrared cameras are attached. These cameras allow to track in real-time the motion of the surgical tools.

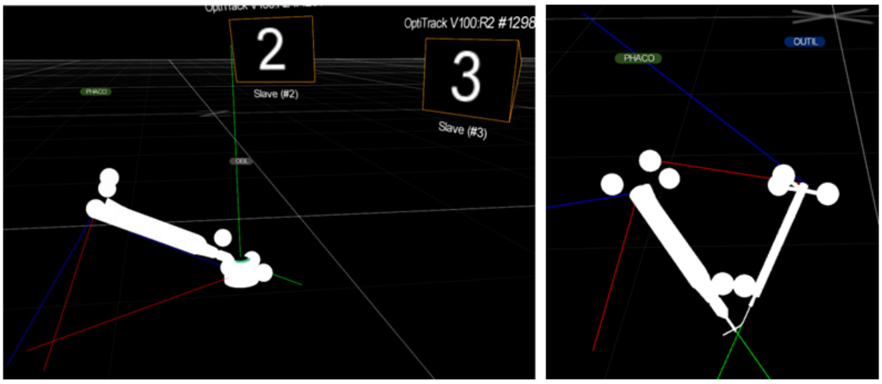

Fig. 1.17: Screenshots of the tracking of surgical tools. With the reflective markers, the tracking system is able to compute the 3D position of the tool in real-time and using different marker signatures, we can manage to detect several tools simultaneously without ambiguity.

---

[5] http://www.cs.unc.edu/Research/vrpn/

Simulation considerations

Bio-mechanical modeling The deformable lens is modeled using a co-rotational FEM formulation with linear elasticity. It is represented by a tetrahedral mesh that can be tessellated to produce small elements (see Figure **??**). We chose an implicit time integration scheme in order to achieve large time-steps and provide a stable simulation even when subjected to challenging interactions. We use the approach detailed in [Cou+10], where the resulting system of equations is solved iteratively using a Conjugate Gradient solver implemented on the GPU.

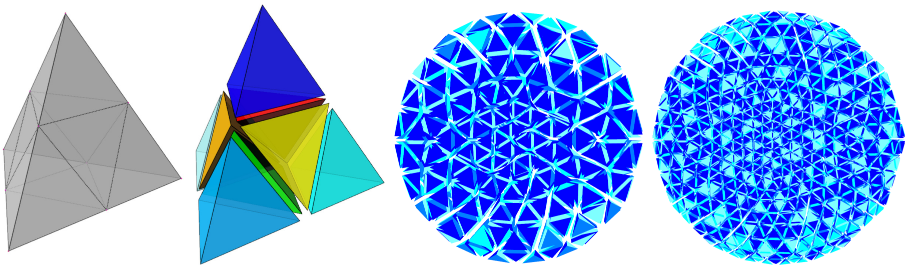

Fig. 1.18: Tessellation algorithm that can dynamically refine tetrahedra (two images on the left). Two-levels tetrahedral topology for lens phacoemulsification (two pictures on the right).

One important aspect of this method is that the mechanical matrix of the full system is not explicitly computed, but matrix-vector products are instead parallelized directly over the mesh elements. This allows to easily change the topology of this mesh, as is necessary in this application to implement the interactions with the phacoemulsifier explained below.

The approach used to model the complex deformations of the implant during its insertion in the lens capsule is based on the use of triangular shell elements and a co-rotational formulation [CCD10; Bou+09]. The combination of both leads to an accurate, yet computationally efficient, shell finite element method featuring both membrane and bending energies. In addition, the polynomial shape functions employed to compute internal forces in our FEM formulation are also used to process contacts and interactions with the curved triangles. The benefits of our approach (fast computation and possible interactions with other objects) allow us to successfully simulate the complex step of the insertion and deployment of the intra-ocular implant.

Interactions Besides the biomechanical modeling of the anatomical structures of the eye and the mechanical modeling of the surgical devices, several specific interactions happened during the procedure:

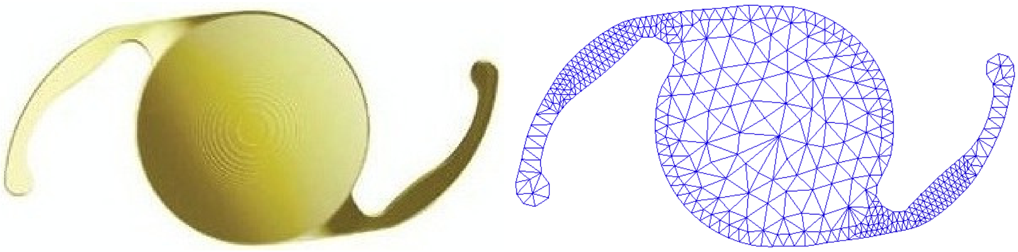

Fig. 1.19: An actual intra-ocular implant (courtesy of Alcon) and the triangular mesh used in our simulations. Notice the higher density of elements in areas where large deformations will take place.

Aspiration: The phacoemulsifier proposes two modes of interactions to the surgeon. The first one, when activated, pumps liquids from the eye into the instrument, creating a force pushing the lens toward the tip of the phacoemulsifier.

Fragmentation: The second one, a probe at the tip vibrate at about 40,000 cycles per second, creating ultrasonic waves that break up the lens into small pieces that are sucked into the instrument by the aspiration and removed from the eye.

Tearing: *Continuous Curvilinear Capsulorhexis*, a technique used to create a circular opening in the lens capsule. Once a small initial incision has been made, this technique relies essentially on the application of shear and stretch forces to create the opening. When performed correctly, the continuous curvilinear capsulorhexis creates a smooth opening, reducing the risk of tear when forces are applied to the capsule during surgery. The main risk with the continuous curvilinear capsulorhexis is to either create an opening that is too large or to create an edge that could promote a tear proceeding outwards.

The aspiration aspect is handled by defining a spherical volume around the type and finding parts of the lens within it. When the aspiration is activated, an artificial force is added to pull the enclosed particles toward the tip. When fragmentation is also activated, we remove tetrahedral elements from the geometrical model of the lens. The removed elements should be as fine as possible to provide an accurate visual feedback to the surgeon. However, the mechanical mesh need to be relatively coarse to maintain good performances. To solve this issue, we use a finer tessellated mesh for rendering and interactions with the instrument. This is done by splitting each tetrahedron in the simulation mesh into eight smaller tetrahedra (Fig. 1.18). Therefore finer elements are removed due to aspiration. And if the eight finer elements of a coarse tetrahedron are removed, the coarse tetrahedron is also removed in order to mechanically take into account the loss of matter in the lens. This allows the use of a relatively coarse mechanical mesh while using a more detailed visual mesh for the rendering (Fig. 1.18).

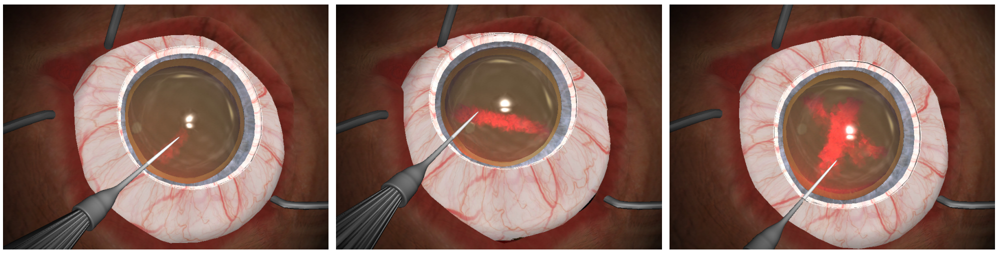

Fig. 1.20: Three screenshots of the phacoemulsification simulation. Local fragmentation of the lens create a cross-like pattern on the lens.

In our approach, we propose to model the deformation and tearing of thin soft tissue (such as membranes, capsules, etc.) by using a transversely isotropic elastic model. The model is based on a co-rotational finite element method formulation, using triangular elements on which a specific fiber directions can be defined (see Figure 1.21). During deformation of the tissue, this fiber orientation, and the principal strain direction on the element are used to determine the tear propagation. Tearing or fracture within an element only occurs when a threshold is reached, which is computed using an eigenvalue decomposition of the strain tensor in each element. If the largest eigenvalue is above a given threshold (in our experiments, the value is tuned according to the feedbacks provided by the surgeon), the element is identified as "*b*reakable" and the eigenvector associated with this eigenvalue corresponds to the principal strain direction (see figure 1.21). Since tearing tends to propagate from an already fractured location, we also account for the history of tear location and direction in the overall computation of the current tear direction. Topological changes on the FEM mesh are performed at each time step. Each triangle in the neighborhood of the current tear location which strain is above our threshold will be re-meshed. This local re-meshing subdivides a triangle into new triangles. There is no particular requirement on the local re-meshing besides avoiding very small triangles which lead to ill-conditioned systems.

Comments

The results presented in this section illustrate that the work required needed to step from the research contributions to a working simulation prototype. These contributions rely on advanced biomechanical models and intensive use of modern graphics hardware to provide fast computation times. Moreover, surgical devices, that are tracked in real-time thanks to infra-red cameras, have been reproduced in

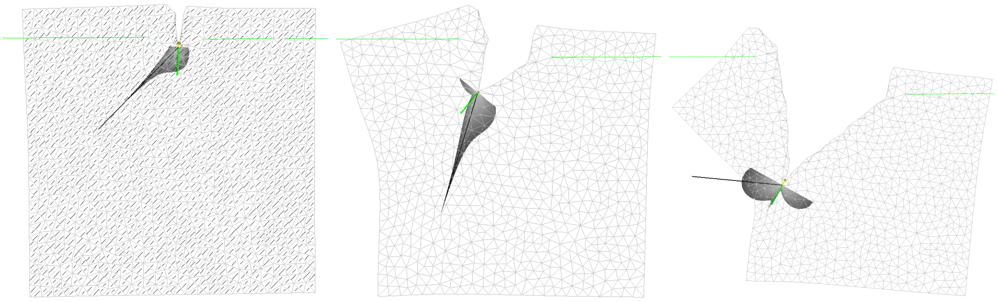

Fig. 1.21: From left to right: tearing propagation throughout the tissue. Fibers (not visible on the meshes since they are defined per triangles) are oriented with a 45 degree angle, and forces are applied outward, on the left and right sides of the square mesh. Our fracture criteria is represented as the shaded area. One can see on the left image how the anisotropy affects the deformation of the tissue, and on the rightmost images how the fracture direction depends on the previous fracture direction, as well as fiber direction. The square mesh is composed of 1,500 triangles. Anisotropic deformation, fracture and remeshing are performed in real-time.

order to faithfully mimic the operating room environment and the actual procedures. Preliminary tests have been performed by experienced ophthalmologists to qualitatively look at the realism of the simulation and the faithfulness of the interactions with the surgical tools.

As these feedbacks were positive a double-blind experiment was supposed to be conducted among ophthalmologist interns to assess the effectiveness of simulation training compared to current companionship training methods. The common ground used to measure surgeons performance during cataract surgery is based on [Sal+07] and is an objective performance rating tool derived from the Objective Structured Assessment of Technical Skill (OSATS) [Mar+97]. OSATS has also been validated for other surgical specialties. The work of Saleh *et. al.* on OSACSS (Objective Structured Assessment of Cataract Surgical Skill) exhibits construct validity and is therefore a valuable tool to assess the surgical skill of trainees [Sal+07]. OSACSS is based on a set of 20 measurements or observations that can be programmed into the simulation engine. For instance, observations include *Eye Positioned Centrally Within Microscope View*, *Iris Protection* or *Capsulorhexis: Formation and Circular Completion* and can be easily translated into computer instructions. Unfortunately this study has been preempted before the end as interns willing to conduct the study left before the end of the study.

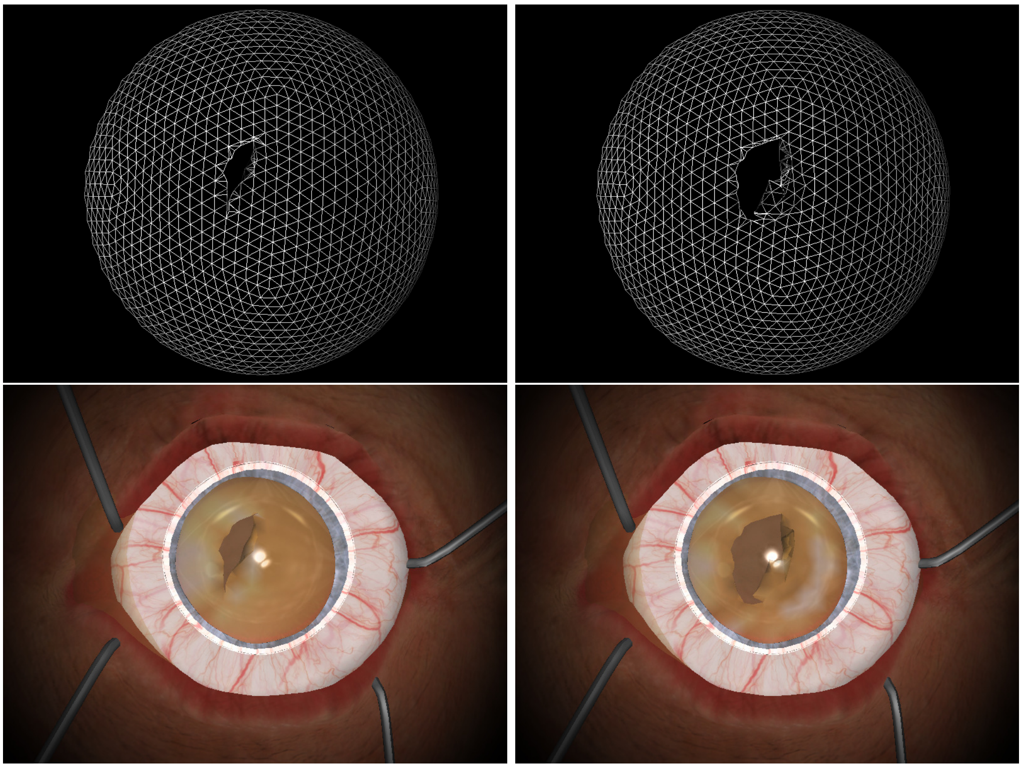

Fig. 1.22: Simulation of capsulorhexis, a technique used to create a circular opening in the lens capsule. This technique relies essentially on the application of shear and stretch forces to propagate a fracture throughout the membrane. Top (a): the mesh used to support the computation of the deformation and topological changes. Bottom (b): final result as seen in the training system.

1.5.2 Planning System

In the case of interventional radiology (see section 1.3 for the clinical context), the overall morbidity and mortality associated with endovascular repair is lower than for surgery (9.5% at one year, compared to 12.2%) the technical challenges associated with coil embolization remain important. It was however shown recently that the risk of complications with coil embolization of unruptured aneurysms decreases dramatically with physician experience [Sin+02]. This clearly emphasizes the need for simulation systems that can be used for physician training as well as for pre-operative planning. This section describes how a simulation tool can be used to select the proper characteristics of the coil based on the patient anatomy, but to also deploy interactively the virtual coil (s) to plan or rehearse the procedure. The interactive aspect in this planning plays a key role as the interventional radiologist constantly controls the motion of the coil and as such influences the final coil placement within the aneurysm.

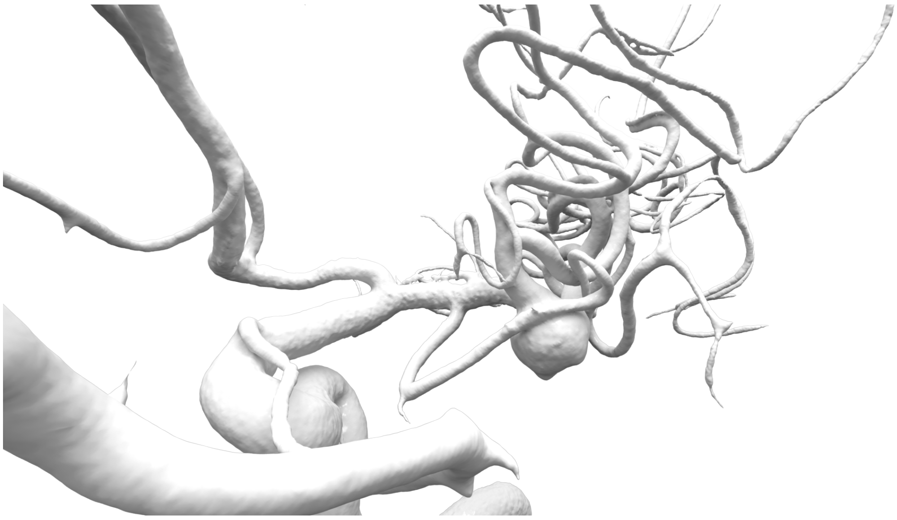

Fig. 1.23: Reconstructed vasculature using 3DXA imaging modality. The 3D volume was segmented and reconstructed using triangles.

Using the approach presented in section 1.3, the geometry of aneurysms and nearby vessels can be reconstructed from a volumetric 3DXA data set (figure 1.23). Then, an actual coil has been deployed inside the aneurysm of the digital model and its shape, during its deployment, has been reconstructed. We then simulated the deployment of a virtual coil in the reconstructed model of the aneurysm. The coil was represented using 100 beam elements. Our dynamic coil model, in combination with the fast solver and contact model introduced above, allowed an interactive and computationally efficient simulation of the coil deployment. In this simulation, a friction coefficient $\mu = 0.6$ was used, and due to the rigid nature of the phantom model, we did not integrate the compliance for the vessel walls or aneurysm during the contact response. While this may seem as a simplified problem, it is actually more complex to handle numerically. Yet, the simulated coil embolization we have obtained exhibits a similar dynamic behavior and final configuration as what can be observed during an actual procedure (see pictures 1.24). Computation times for the whole simulation including coil deformation, collision detection were of 50 ms in average, although they varied depending on the number of contacts.

Figure 1.25 is a close-up on the final stage of the coil deployment and illustrates that our whole approach prevents penetration of the coil inside the vasculature wall as well as self-penetrations of the coil which is mandatory to have a realistic simulation. The mechanical model also allows large deformations of the model making the coil possible to conform to the aneurysm shape.

Using the simulation for coil deployment enables to have additional information that can be useful for clinicians. Since the contacts between the surgical devices and the

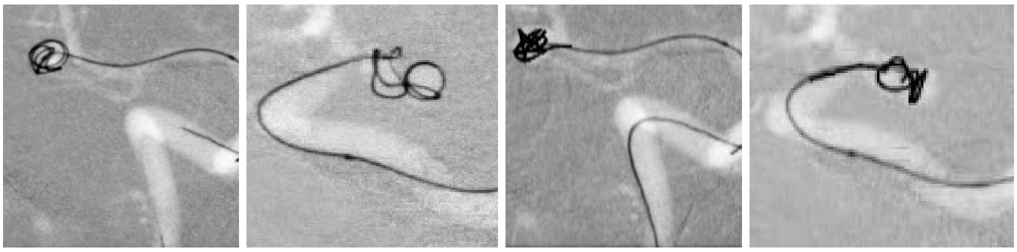

Fig. 1.24: Examples of our simulation results: (two images on the left) real coil embolization; (two images on the right) our simulated coil embolization with 3D coils.

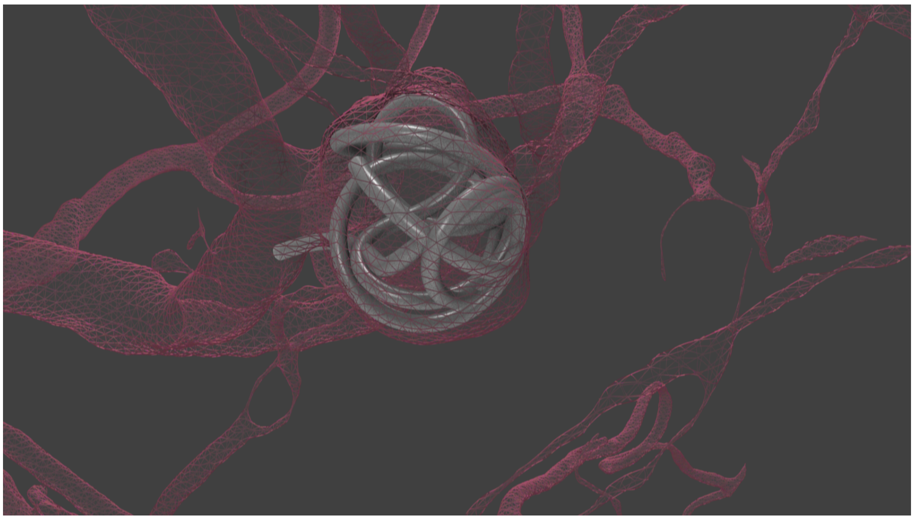

Fig. 1.25: Examples of our simulation results: close-up on the coil deployment and wireframe display to illustrate the deformation of the coil.

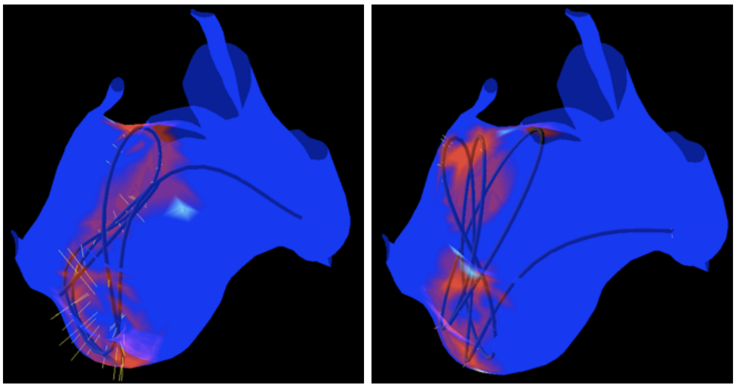

Fig. 1.26: Examples of our simulation results: pressure of the coil on the aneurysm surface can be displayed using a thermal scale Using a larger coil (right) induces more important pressure on the aneurysm wall which could lead to rupture.

anatomy are handled with mechanical constraints, pressure on the surface can be computed. Figure 1.26 illustrates the kind of additional data that can be displayed for the radiologists: pressure was color-coded using a thermal scale (blue=low to red=high) to enable a better comprehension of the locations of highest pressure on the aneurysm wall during coil deployment in real-time. Contact forces were also depicted as yellow arrows whose length is proportional to the intensity of the forces. Choosing a larger coil implies a significant increase of pressure forces on the aneurysm wall.

Having the simulation software can be used by experienced or novice radiologists to test different strategies in a safe environment. For example, given a specific patient with an aneurysm, users can try different coils (helical, 3D. . .) or insertion strategies to select the one that seems to be optimal given the aneurysm features. Figure 1.27 is an example of this planning strategy: 3 different helical coils (4mm, 7mm and 10mm diameter) have been inserted in the aneurysm and the simulation illustrates the role of the diameter in the deployment: the smallest one cannot fit the aneurysm cavity and is floating inside the bulge making it very dangerous for the patient (can move into the parenting artery and thus into the brain), whereas the largest one induces increased pressure on the wall that can lead to rupture (and cause hemorrhage).

The placement of the first coil is an essential step to guarantee the success of the procedure: it should cover most of the surface of the aneurysm and should be firmly anchored on the aneurysm wall as it will served as a support for the following coils [Sat+98; Tam+02]. A common metric that is routinely used in the CER (*Coil Embolization Ratio*) or VER (*Volume Embolization Ratio*) that has been to be positively correlated with the long term stability of the embolization [Clo+00; YAG+05]. The

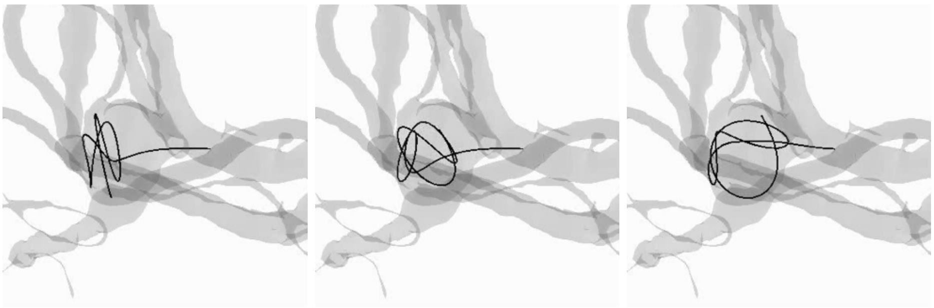

Fig. 1.27: Examples of our simulation results: using helical coils with different diameters: (left) 4mm helical coil which is too small for the aneurysm and the coil is floating inside the aneurysm and this can be dangerous for the patient, (middle) 7mm helical coil which is the optimal size for this aneurysm, (right) a 10mm helical coil which is too big and leads to extra pressure on the aneurysm wall.

CER requires volumetric data of the aneurysm in order to be computed which cannot be done in every clinical set-up. For a fast metric that can be done with any imaging modality, we propose to derive the CER to the CESR (*Coil Embolization Surface Ratio*) because it combines the several advantages: close to the current clinical usage of radiologists, easy computation that can be done in the working imaging view during the procedures. Computation is a simple ratio between the surface (in pixels) occupied by the first coil and the surface (in pixels) of the aneurysm.

	REF	OK	NOK
Patient 1	81% (0%)	68% (16%)	55% (32%)
Patient 2	24% (0%)	17% (30%)	11% (54%)

Tab. 1.2: CSER computation for two patients. REF corresponds to the CSER of the coil inserted by the clinician, OK represents the CSER of the simulation of the same coil, NOK represent a simulated helical coil. The relative errors to the REF are provided in parentheses.

Figure 1.28 illustrates the computation of CSER for two different patients and the results are reported in the table 1.2 where 2 patients have been treated with 3D coils. The first column represents the CESR from real road-map image (REF), the second column represents the CESR from simulation with the right 3D coil (OK), the third column represents the CESR from simulation with a wrong helical coil (same diameter) (NOK). Given this scenario, the following comment can be made: the CESR is able to distinguish between a right (3D) coil and a wrong (helical) coil. This difference appears clearly in the case of the bilobated aneurysm (patient 2). For patient 1, the rounded shape of the aneurysm justifies a lower relative error for the helical coil. These first results are interesting but the quite large relative errors for the right coil require a refinement of CESR as a quantitative score.

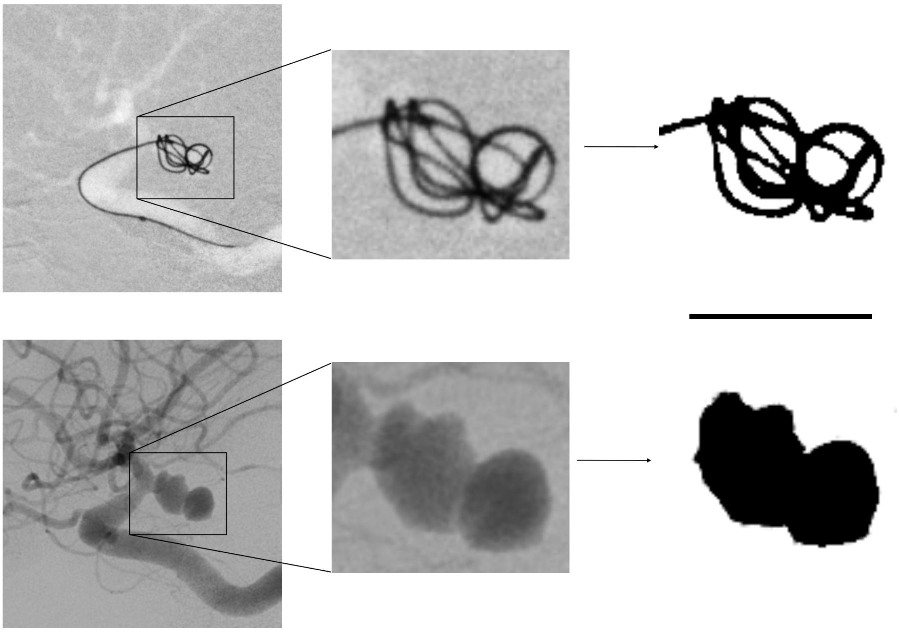

htbp

Fig. 1.28: Computation of the Coil Embolization Surface Ratio metric: it divides the surface of the coil by the surface of the aneurysm.

1.5.3 Discussion

The previous application examples illustrate that our simulations perform *qualitatively* well compared to actual surgical or interventional procedures. However a *quantitative* assessment of the performance is difficult to conduct: many software components needs to be evaluated (bio-mechanical models, interactions, environment modeling. . .), boundary conditions are badly-known and ground-truth data depends on imaging modalities that exhibit several limitations in terms of resolution, dynamic range and noise. In order to address the these particular challenges, the following chapter will detail some contributions around the use of medical images to extract relevant informations for the simulation.

2

Geometric Modeling for Interactive Simulation

> *Arithmétique ! algèbre ! géométrie ! trinité grandiose ! triangle lumineux ! Celui qui ne vous a pas connues est un insensé !*
>
> — **Lautréamont**
> Les Chants de Maldoror

Obtaining digital representations from medical images is a two-step process that combines first the *segmentation* of the image and second the *reconstruction* of the digital model. Segmentation consists in splitting a raw image into one or several structures of interest and isolating non-relevant information (*i.e.* the background). From 2D, resp. 3D, arrays of pixels, resp. voxels, segmentation consists in classifying each pixel / voxel according to the structure it belongs to. While manual segmentation is possible, it is a time-consuming task and subject to operator variability. Automatic segmentation is therefore encouraged and mainly relies on signal processing techniques. Reconstruction consists in building a digital representation from the processed image according to geometric modeling techniques. While this process is very common in the Computer Vision community, several constraints inherent to medicine makes this problem much more challenging: some are related to imaging, some are related to the patient itself.

Whatever the imaging modality and despite impressive progress in imaging, segmentation faces three image-dependent problems. First, images are *noisy* and may alter pixels intensity making the classification more difficult. Second, images may exhibit *intensity nonuniformity* where the intensity of a single structure varies over the extent of the image. Third, images have relatively low definition (often around 256/512 pixels for each dimensions), which induces *partial volume averaging* meaning that an individual pixel contains a blend of several structures and thus the intensity of a pixel may not be related to the intensity of pixels from a given structure. For dynamic imaging such as dynamic MRI, the acquisition rate is not fast enough to capture very fast motion leading to blurry data. And at least, some structures are not visible under specific modalities (for instance ligaments in MRI).

There is a huge inter-patient variability for anatomic structures which means that for a given structure an average representation or template cannot be used as an *a-priori* to ease the segmentation step. Moreover even manual segmentations performed by experts present uncertainties: *inter-observer variability*, variability where several experts perform the segmentation, as well as *intra-observer variability*, variability when a single export perform the same segmentation multiple times, has been recorded.

Thus, from a formal standpoint, the segmentation of medical images can be seen as under-determined problem where there are multiple classifications from a single image. The main challenge when developing segmentation algorithms is to propose methods that try to overcome this image limitations while producing acceptable results for experts. This is a very active field in research and the medical imaging community have proposed many different approaches. First approaches used image processing technique such as thresholding [SV16], region growing [HK98], edge tracing [HL00], while more recent works have used statistical analysis [BHC93], clustering [Pha01], deformable models / active contours [KWT88], neural networks [Bar+94] or atlases [Fis+02].

Segmentation has been extensively studied in the medical imaging community but remains on open-problem. Reconstruction has however received less attention and this can be explained by the first applications of medical imaging which were mostly used as a tool for diagnoses. Therefore the smoothness, the compactness, details outside the area of interest were not primary criterion for the reconstruction. As a result first models were only voxel soups who exhibit jagged surfaces 2.3. This was enough to give some hints or overview about the targeted area but the overall shape lacked realism. Besides these visual considerations, the smoothness of shapes is an important feature to have for mechanical simulations since irregular or jagged surfaces could lead to artificial sticking of objects instead of sliding. For instance, the figure 2.1 illustrates the influence the importance of friction in the context of catheter navigation: since the main behaviour of this navigation relies on the catheter sliding along the vasculature wall and the use the support of the vessel to take a specific vessel in case of branchings, the change of friction coefficient or artificial friction introduced can lead to very different simulation. To illustrate the importance of static friction phenomenon, Alderliesten *et al.* [AKN07] have conducted a thorough quantitative experimental validation of a quasi-static model of guidewires: 3D comparison through 3DRA is performed with several deployment scenarios.

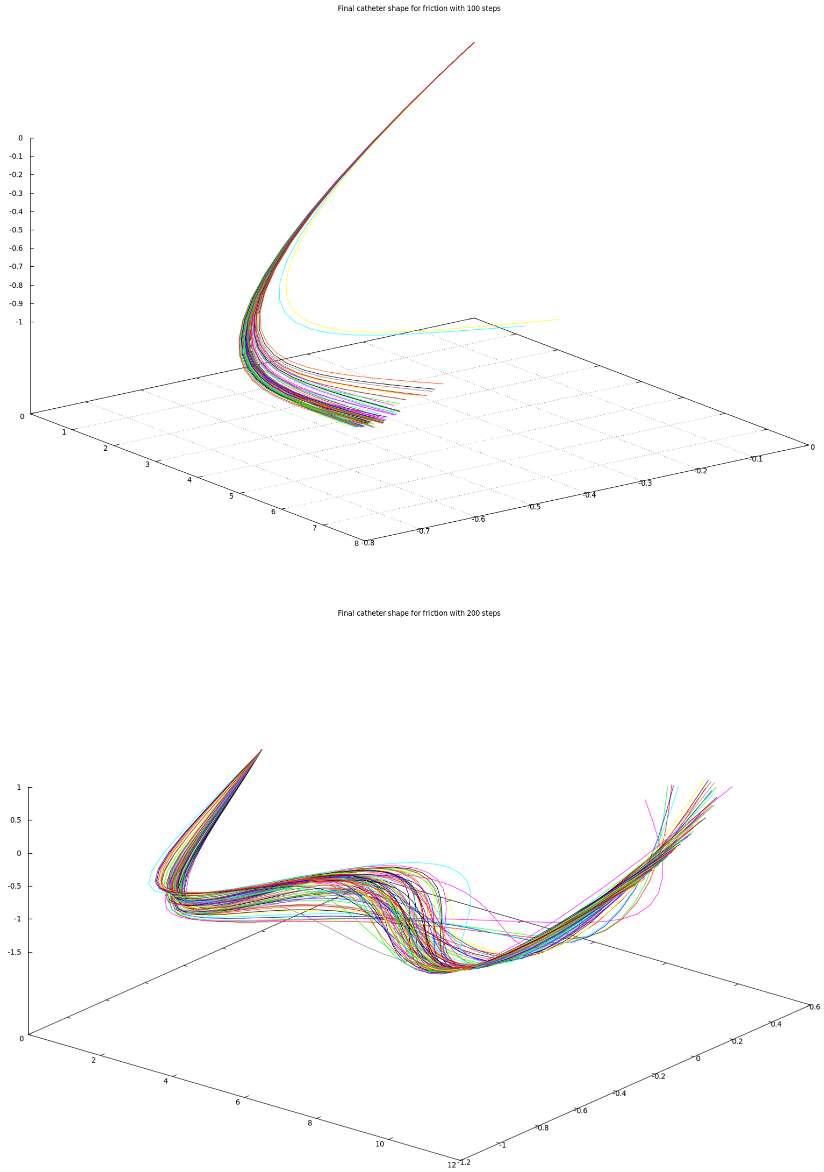

Fig. 2.1: 200msec recorded sequences of catheter deployments in a small cylindric vessels. Catheters share the same mechanical parameters and only the friction coefficient between the vessel wall and the tool is modified. This illustrates the importance of adequate friction estimation and smooth geometry.

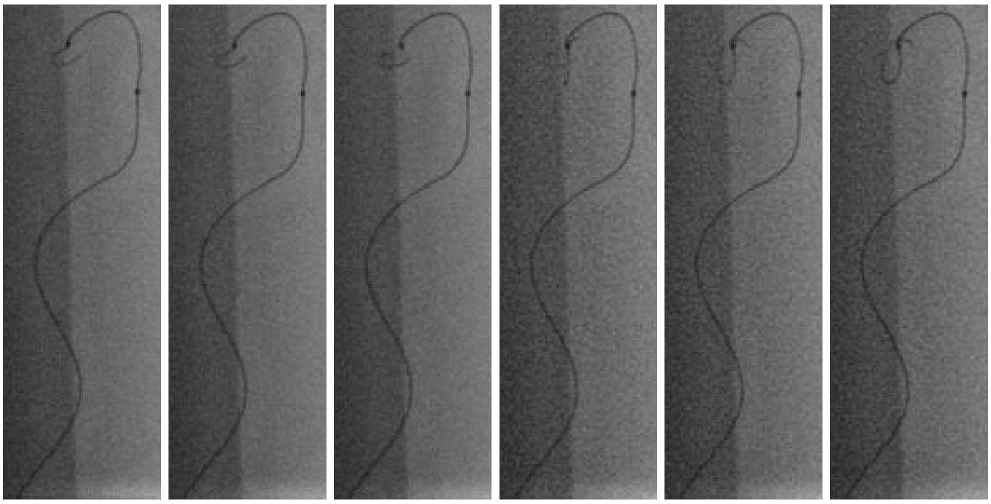

Fig. 2.2: Recorded sequence of a coil deployed at low and constant speed where image acquisition is performed at 15 fps through 3D Rotational Angiography. The sequence shows the effect of friction and then sliding as the coil completely changes its configuration between frames 3 and 4 (67 msecs between each frame).

Dynamic friction is also to be considered because it can significantly change the trajectory followed by the devices. Even if the friction between the arterial wall and the tools may be negligible in certain circumstances (for instance slow motion, simple path to reach the targeted area), its effects are significant in tortuous vasculature or aneurysms. The figure 2.2 illustrates that friction implies high frequency motion for the deployment of a coil (thin coated platinum thread) in an aneurysm. Therefore, accurate models for the tools and for the interactions between tools and the blood vessel are mandatory.

A second feature that is less important for the accuracy of the simulation but is essential for optimization is the compactness of the virtual 3D model, *i.e* the number of primitives used to described the virtual model: not only a more compact model implies a smaller memory footprint but since collision detection step usually has to inspect all the primitives, this is a time-consuming procedure. Without any optimization the cost of the collision step, is quadratic with respect to the number of objects in the virtual environment and quadratic to the number of their primitives. Obviously, optimization strategies exist [Zac01] but even with these optimization, it is one of the most costly step of the simulation loop. Indeed, dealing with deformable objects invalidates optimization based on geometry pre-processing because the geometry may change at every time-step. Having a compacter model may reduce the computational burden of the collision detection. Dedicated ways of representing shapes such as distance fields or implicit surfaces may also be investigated.

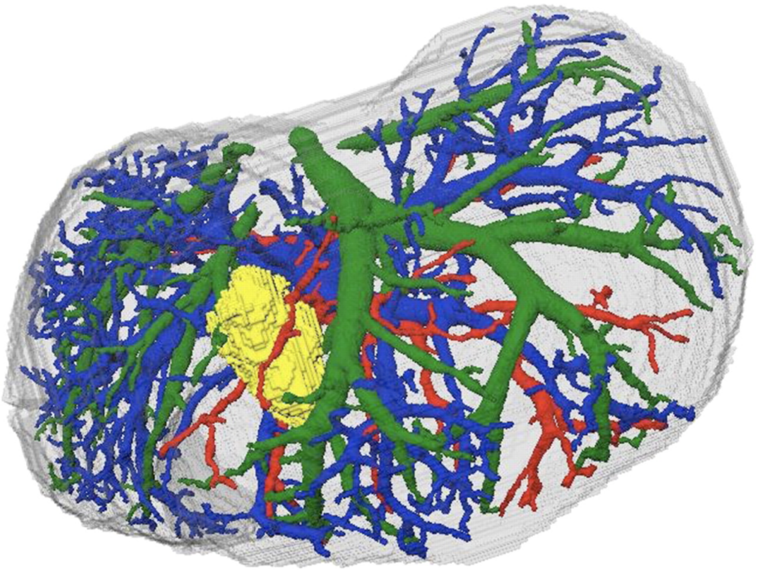

Fig. 2.3: Reconstructed liver and its vasculature: segmentation and reconstruction have been performed without smoothing. The limited resolution of the imaging device leads to virtual 3D models that exhibit jagged surfaces which are not very organic.

The contributions detailed in this chapter will illustrate two examples of geometric modeling: starting from medical images, specific and *simulation-aware* strategies will be used to obtain 3D geometric models that are optimized for mechanical simulation applications. But before digging into these two contributions, we will elaborate on implicit surfaces and illustrate that it is a representation that is very convenient for mechanical simulation.

2.1 Smooth surface using implicit surfaces

An implicit surface is based on a function f and a scalar constant c, called *isovalue*. The function f associates to any point $P(x, y, z)$ of the 3D space, a scalar value $f(P)$:

$$\begin{array}{rccc} f: & \mathbb{R}^3 & \longrightarrow & \mathbb{R} \\ & \boldsymbol{P} & \longmapsto & f(\boldsymbol{P}) \end{array} \tag{2.1}$$

The resulting space obtained by applying f to $\mathbb{R}^3$ gives a scalar field called *implicit* or *potential* field. The equation $f(P) = c$ describes an isosurface, separating the values greater to c of the implicit field from the values lower to c. Usually a g function is introduced which is $g(P) = f(P) - c$. Such surface is usually discretized and parametrized to be displayed.

An interesting property is that the gradient of f defined as:

$$\nabla f = \frac{\partial f}{\partial \boldsymbol{P}} \tag{2.2}$$

gives the normal to the isosurface that passes through $f(p)$ and $-\nabla g$ points to the direction that reaches the faster the higher values of the field. Such property is useful for contacts resolution with implicit surface.

The choice of function f is a complex step there is no convenient way to extract the function from a arbitrary shape. In the case of tubular structures, such as blood vessels, Bloomenthal [Blo95] introduced convolution surfaces which are skeleton-based implicit surfaces. The surfaces are described with few geometrical primitives (called *skeleton* s) and a convolution filter h which is a function from $\mathbb{R}^3 \longrightarrow \mathbb{R}^+$ and has a finite support or fast decay to 0. The resulting surface is defined as $\forall P \in \mathbb{R}^3, f(P) = h(P) \otimes s = iso$, where iso is an isosurface value and $f(P)$ the potential at P. The convolution surface then produced is smooth and very appropriate to design organic 3D objects. The figure 2.4 represents a simple vessel-like network built with cylindrical primitives and a gaussian convolution filter. The surface is also easily modifiable to produce anatomical anomalies such as stenoses or aneurysms.

Given the previous analytic formulation of the surface, the collision detection is about to find where a point cross the surface. With $g(P) = f(P) - iso$, this is equivalent to root-finding problem on the interval $[P_t, P_{t+1}]$. A Newton-Raphson algorithm is used to grant quadratic convergence. Moreover to insure convergence criteria (*i.e.* monotonicity of g and a single root on the interval), we subdivide $[P_t, P_{t+1}]$ according to the number of primitives and their radii. When the crossing point P is found, we can easily compute an linear approximation of the surface as $-\nabla g(P) \times x = \|P\|$ (tangent plane) to use it for the contact algorithm. Figure 2.5 illustrates several steps of a simulated procedure where a catheter and a guide-wire are inserted into a virtual simple vascular model.

We have applied our method to a complex simulation: the navigation of a catheter and guide-wire inside a reconstructed vascular network to perform a virtual angiography and the deployment of a coil inside an aneurysm to perform an embolization. The catheter, guide-wire and coil models consist of a series of non-linear deformable

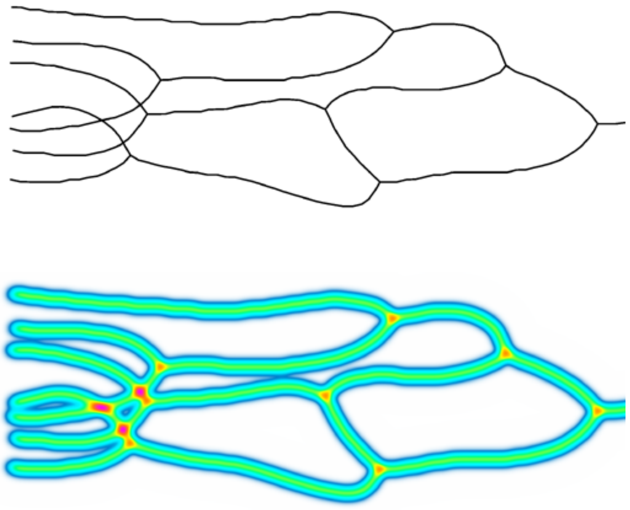

Fig. 2.4: Skeleton-based convolution surface: using a skeleton defined by cylindrical-shaped primitives (top, for clarity, only the center line of the cylinders are shown) and a Gaussian convolution filter. The potential field is displayed with a heat-map (left-bottom).

beam elements. Each device is composed from 100 to 200 beam elements while the vascular network is constituted of more than 4,000 vessels and undergoes periodic deformations due to both cardiac and respiratory motions. When entering the cerebrovascular system, where the diameter of the vessels is very small, the catheter or guide-wire are constantly colliding and sliding along the vessels wall (see Figure 1). Similarly, when deployed within an aneurysm, the coil becomes highly constrained, and proper contact modeling becomes of prime importance to guarantee a correct behavior during the simulation (see Figure 2.6). We have performed a series of simulations on a standard desktop computer and obtained real-time computation rates (100 Hz). These timings include the computation and inversion of the system stiffness matrix K at each time step, as well as collision detection and collision response. Since the contacts are solved in the contact space, the size of the system is the number c of contact (defining n as the number of DOFs, $c \leq n$ and usually $c << n$). It is also important to mention that, in order to enforce the convergence and stability of the contact algorithm, we use a subdivision strategy where each time step is subdivided into a variable number of sub-steps. The initial time step is subdivided if not all contacts have been solved after N iterations of the main loop of the algorithm. This subdivision strategy allows us to solve complex contact configurations and to handle concave cases has a succession of convex cases.

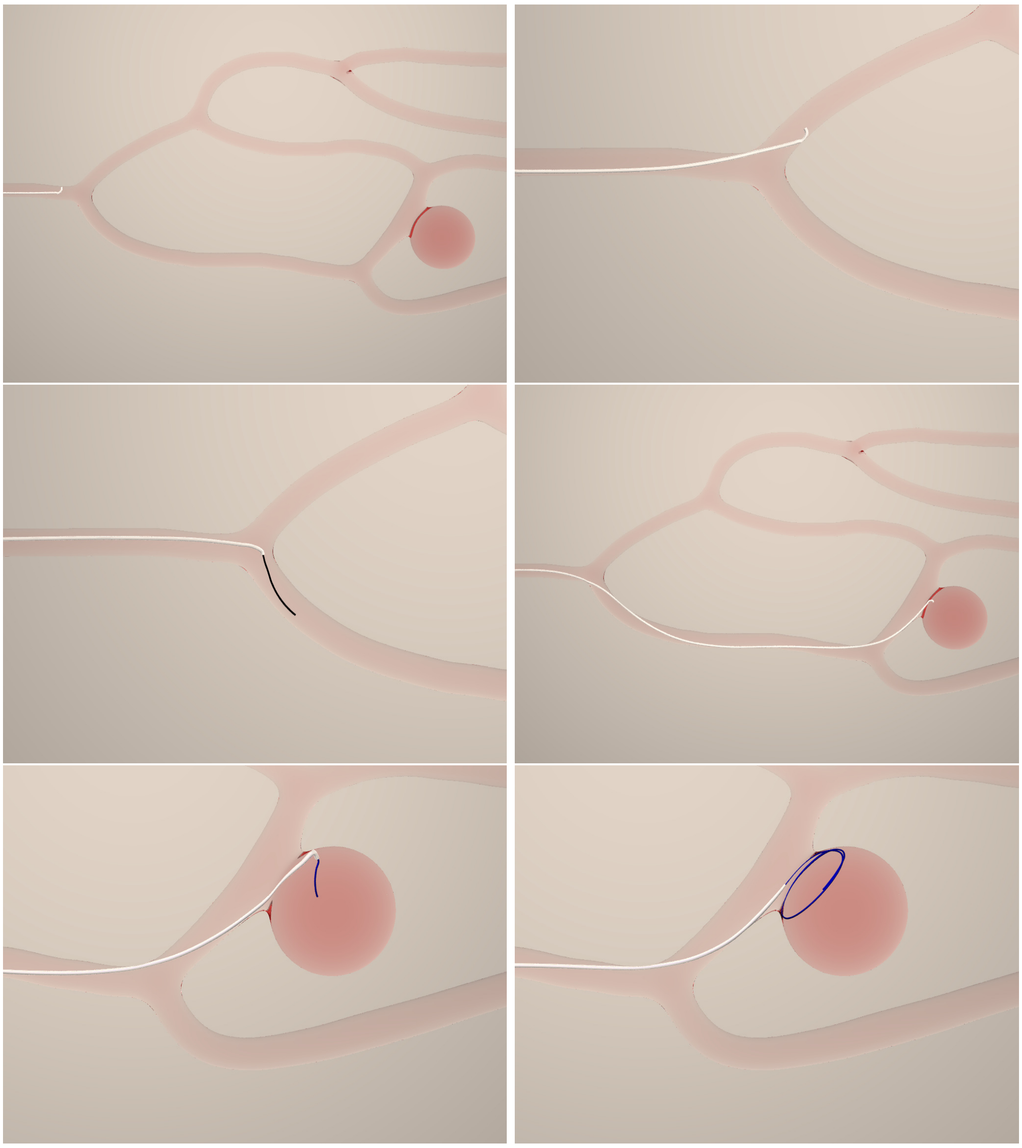

Fig. 2.5: Example of catheter and guide-wire navigation inside a vascular phantom using convolution surfaces as the underlying geometric model.

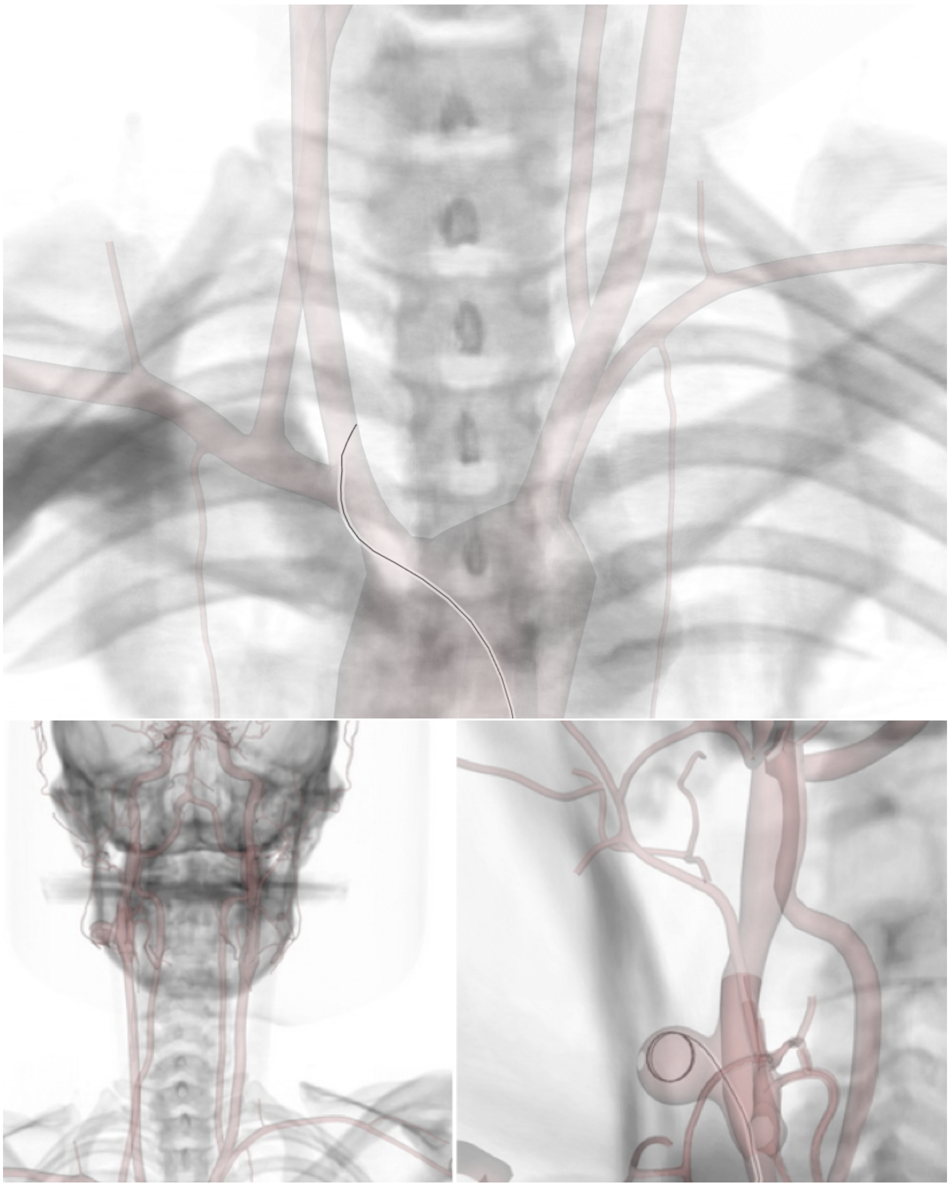

Fig. 2.6: Example of catheter and guide-wire navigation inside a vascular network of a specific patient. The vascular model consists in more than 4000 blood vessels and the simulation can be run at interactive rates (100 Hz). Complex configurations (tortuous and small vessels) are handled correctly.

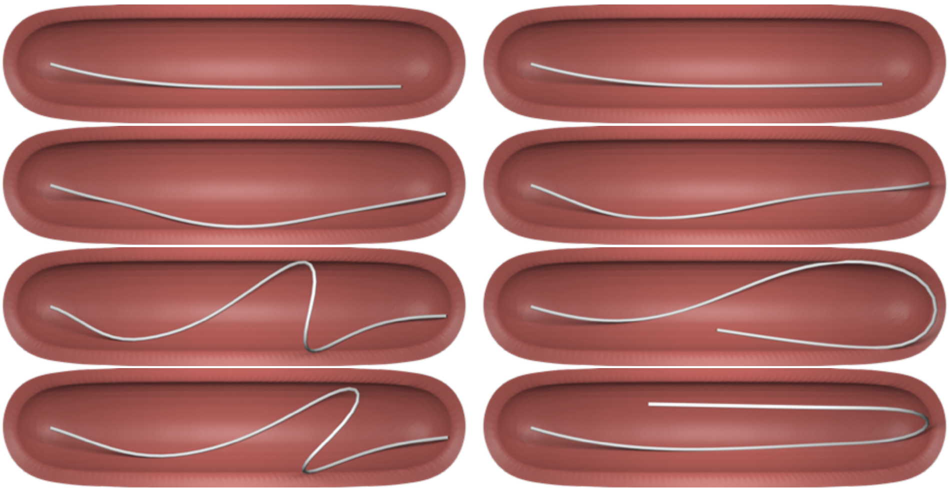

Fig. 2.7: Catheter deployment in a closed capsule. (Left-column) the capsule is modeled as a polygonal mesh, (Right-column) the capsule is modeled as a convolution surface. The snapshots taken at the same simulation time-steps illustrate that artificial friction can be induced with polygonal meshes because the tip sticks into the perfectly smooth vessel instead of sliding along it (which is the case of the implicit surface).

To illustrate how artificial friction can be induced with (*relatively*) polygonal models, we perform a simple experiment: we deploy a catheter-like tool inside a closed capsule with an ellipsoidal shape. This shape is modeled with 400 polygons (mainly quads but with several triangles) or with a skeleton-based convolution surface with a single primitive (*a segment*). The results are illustrated on 2.7 where the left-column displays the deployment inside the polygonal mesh while the right-column displays the deployment inside the implicit surface. Deployment inside the implicit surface is perfectly smooth without any hitch. On the contrary, the deployment inside the polygonal surface exhibits a moment where the tip of the catheter is stuck in the surface (on an edge between two polygons), then the deployment produces a spring catheter shape where a lot of internal energy is accumulated that can lead to fast and uncontrollable release at any time. Again such artificial friction is unnoticeable when objects in simulation have temporary contacts but when the simulation will contain sliding of objects on another, this becomes a major concern. Obviously this limitation of polygonal surfaces can be addressed by using smaller elements and thus producing a *smoother* surface but it will significantly improve the time needed for collusion detection.

This previous examples illustrate the potential of implicit surfaces for simulation and more specifically for applications where contacts with friction and sliding will be preponderant such as interventional radiology procedures are. However while it is straight-forward to derive implicit surfaces for basic shapes or skeleton-based shapes, building an implicit surface from an arbitrary shape is complicated. Since we aim at patient-specific simulation (for planning applications for instance), we should address how to build accurate implicit surfaces for medical images.

2.2 Models of vascular anatomy

Our objective is the simulation of neuroradiology interventions. Procedural implicit surfaces appear best suited for precise and physically grounded contact computation. But the complex intracranial vasculature is likely to require a complex implicit function, putting interactive simulation rates at risk. Besides, vessel centerlines carry precious topological information to accelerate contact localization. But current implicit vessel representations cannot be used for simulation. Cylinder-like shapes are unable to capture details at the vessel surface, and cross-sectional descriptions suffer from a lack of smoothness in the longitudinal direction.

The Computer Graphics community has devoted a vast literature to the problem of implicit surface reconstruction from data points [Ber+13]. Such methods bear no difficulty to interpolate missing data points [Oht+05] but handling noise and outlier data points is still considered an issue [Mul+10]. Besides the advantages mentioned in the previous section, implicit surfaces tend to blend as they come close to each other. As a result, implicit modeling of a complete vasculature is very difficult since, for example, close or kissing vessel branches merge 2.8. Controlling the blend is still an open problem when more than two objects are merging or in the case of complex topologies. Moreover using generic-purpose segmentation algorithms may lead to other artifacts such as holes or discontinuing vessels (see Figure 2.8 bottom).

Therefore, we propose in this section a new blood vessel surface model, namely Local Implicit Modeling (*LIM*), that uses a specific implicit reconstruction from data points. To get these data points, a new blood vessel tracking algorithm is proposed that

- detects the vessel centerline;
- provides a local radius estimate;
- extracts a dense set of points at the blood vessel surface.

This algorithm is based on a RANdom SAmple Consensus (*RANSAC*) based robust fitting of successive cylinders along the vessel. Our method was validated against the Multiple Hypothesis Tracking (MHT) algorithm on 10 patients three-Dimensional

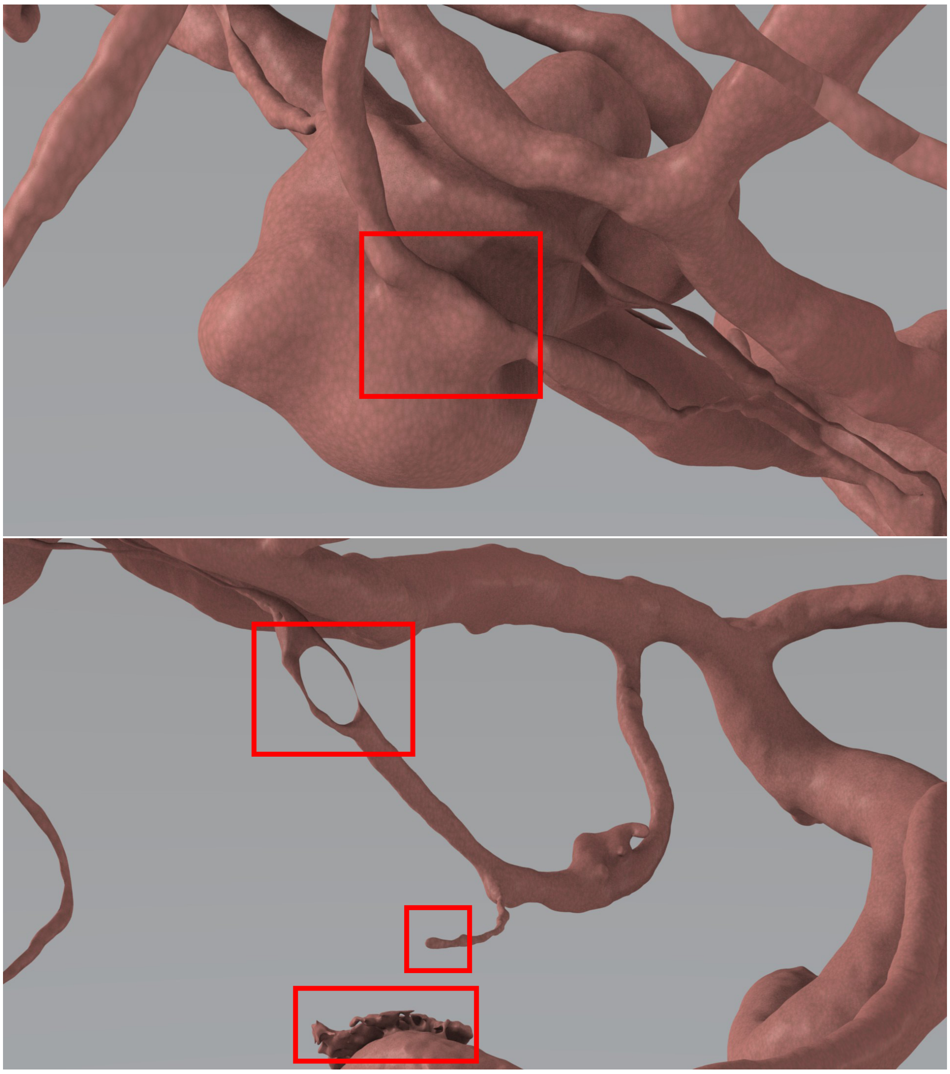

Fig. 2.8: Examples of reconstruction issues from segmented medical images. Since the contouring of the vascular structure do not encode any topological information many artifacts may occur such as blending between aneurysms and vessels (top) or holes and discontinuing vessels (bottom).

(3D) Rotational Angiography (RA) data. Over 744 blood vessel of various sizes were considered for each patient. Given these data, LIM locally reconstructs the blood vessel surface thanks to information provided by its centerline and a dense sampling of the vessel surface (point-set). In other words, LIM locally performs the point-set reconstruction by fitting a skeleton-based implicit function - i.e. Blobby Model (*BM*) - through energy minimization, alternating with an original selection and subdivision scheme of BM primitives (iterative process). The idea of LIM is to enrich the blood vessel centerline by attaching a BM to a point on the centerline that locally reconstructs the vessel surface. The resulting blood vessel surface is supplied as a tree of local implicit surfaces generated by BMs.

2.2.1 Vessel Centerline Tracking

Overview of the algorithm

We model the local vessel shape as a finite cylinder $(C, r, \mathbf{d}, h)$ where C is the center, r the radius, $\mathbf{d}$ the axis direction, and h the height. Our algorithm alternates between a prediction and an estimation step. State t is predicted from state $t-1$ by:

$$C_t^\star = C_{t-1} + s\frac{h_{t-1}}{2}\mathbf{d}_{t-1} \tag{2.3}$$

and

$$(r_t^\star, \mathbf{d}_t^\star, h_t^\star) = (r_{t-1}, \mathbf{d}_{t-1}, h_{t-1}) \tag{2.4}$$

where s is a scaling factor for the height-dependent step size. We set it to 0.5 in order for successive cylinders to superimpose.

The estimation step is more complex. First, it extracts a set of candidate points at the vessel surface in the vicinity of the cylinder location predicted by $(C_t^\star, r_t^\star, \mathbf{d}_t^\star, h_t^\star)$. Then the best cylinder $(C_t, r_t, \mathbf{d}_t, h_t)$ is found that fits these points. A subset of candidate points are thereby found to lie at the blood vessel surface. We propose to add this subset of selected points to the vessel shape description. Hereafter, a focus is made on the different steps of the estimation process.

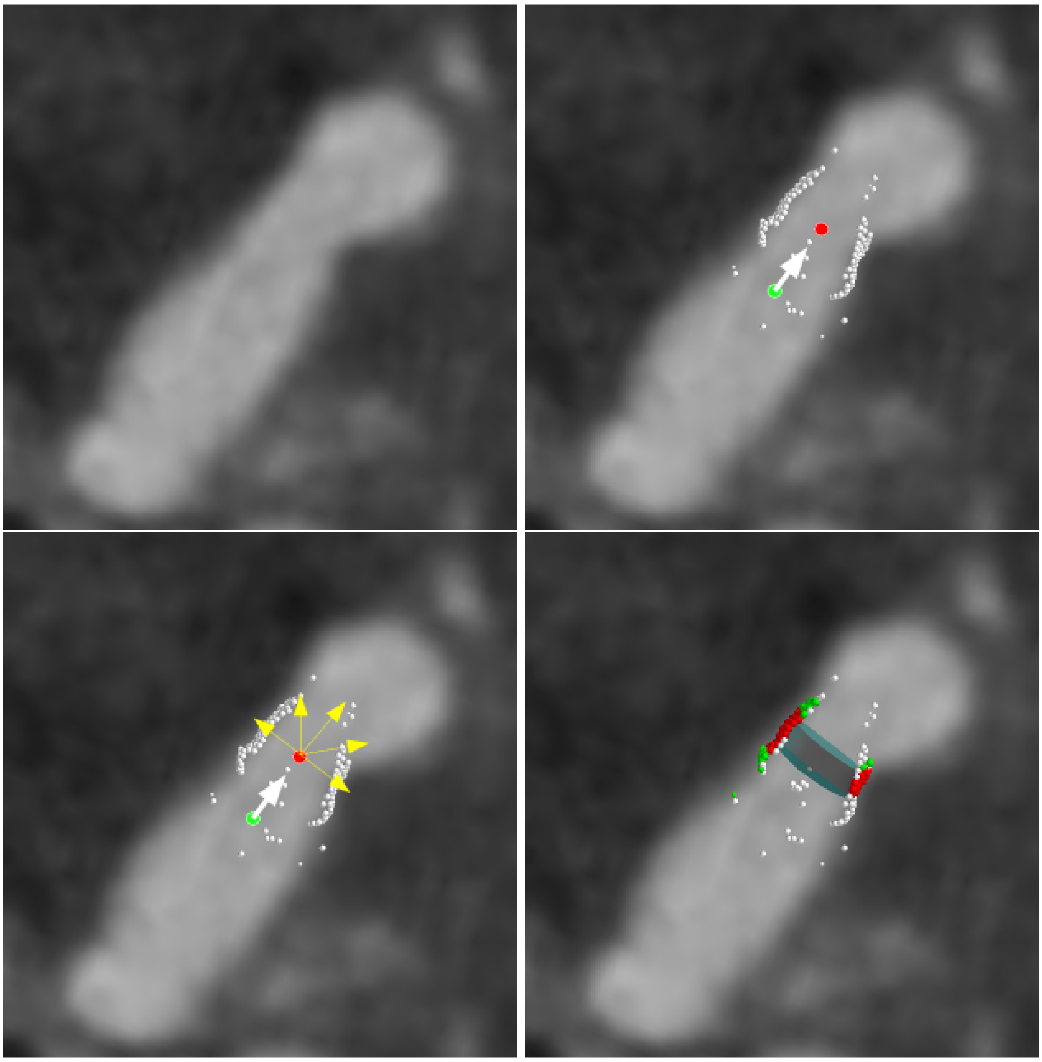

Fig. 2.9: Outline of RBT vessel tracking algorithm. (top left) Cut plane through the original 3DRA data; (top right) Prediction: Starting from C_{t-1} (green dot) and $\vec{d}_{t-1}$ (white arrow), the new center $C_t^\star$ (red dot) is found. Candidate points (white dots) are extracted at the vessel surface by casting rays in the volume, from $C_t^\star$. Only the points around the displayed cut plane are shown. (bottom left) N_d directions are tested for the cylinder axes (yellow arrows). One fitting cylinder is found per axis, using RANSAC. (bottom right) Best cylinder found $(C_t, r_t, \vec{d}_t)$, together with its consensus set (green dots). The red dots were used to compute the cylinder height h_t: they are the set of points $\mathcal{P}_t$, attached to the cylinder.

Candidate point extraction

In angiographic images, such as 3DRA data, the vessels are bright tubular-shaped objects, on a dark background. The points of minimal directional gradient along rays cast from the cylinder center $C_t^\star$ are collected as candidate points at the local vessel surface (one point per ray). This extraction scheme is very similar to taking the points of maximal gradient along the columns of a bounded spherical projection image [WC07a] except that we used N_r rays evenly sampled on the Gaussian sphere to avoid point clustering that occurs at the poles with spherical coordinates.

The prediction step, followed by the candidate point extraction is illustrated in figure 2.9, top right.

Cylinder fit with RANSAC filtering

Most of the extracted points lie at the local vessel surface, even though this location is tainted with noise, but some points are outliers, due e.g. to neighboring structures or bifurcations. RANdom SAmpling Consensus (RANSAC) is a robust estimation procedure that has been successfully applied to fit cylinders to a point set [CG01]. It relies on a closed-form equation to retrieve the cylinder parameters from a minimal set of points. Various solutions exist depending on the parametrization of the cylinder [CW06]. In [CG01], the cylinder axis direction was first estimated and the center and radius of the cylinder were estimated using RANSAC. This parametrization has the advantages of simplicity (it resorts to fitting a circle to three points in the plane orthogonal to the axis) and low complexity (the minimal input set has only 3 points).

In our case, the axis direction can hardly be estimated from the point normals as in [CG01]. Indeed, the normals would be computed from image gradients, which are sensitive to noise, and would be untrustworthy around curved portions of the vessels. Therefore, a strategy similar to [Fri+10] was adopted: N_d predefined axis directions are tested, centered on $\vec{d}_t^\star$; the best cylinder (center and radius) for each direction is estimated by RANSAC (see figure 2.9, bottom left). The N_d directions are reviewed by increasing angle with $\vec{d}_t^\star$: as soon as a valid cylinder is found (see below), the search stops and the cylinder is kept. This pruning strategy speeds up the process.

In order to cope with a large scale of vessel sizes, the distance threshold was set proportional to the estimated radius: a point is an inlier if its distance to the cylinder is below $0.1 r_t^\star$. The set of inlier points is called the consensus set.

Validity of a cylinder

RANSAC iteratively fits a cylinder to a set of 3 randomly sampled points. This cylinder is considered valid as soon as its consensus set encompasses more than $p_{inl}\%$ of the input point set. The density constraint proposed by [CG01] was not applied in order to consider cylinders despite holes in the point set due to e.g. vessel bifurcations. However, RANSAC may exhibit cylinders of extreme radii (either too small or too large) as degenerate solutions. Therefore, a cylinder was considered as valid only if its radius was in $[r_t^\star/2, 3r_t^\star/2]$ [WC07a].

Refinement and height estimation

The minimization, using Powell's algorithm, of the distance from the returned valid cylinder to its inlier point set is searched to tune its parameters. In particular, it enables the axis direction to be refined from its initial discrete value. Then, the position of the cylinder center is adjusted along the axis, to coincide with the median position of the inlier points. Thereby the new parameters $(C_t, r_t, \vec{d_t})$ are set. A new set of candidate points is extracted using these values and the points in consensus with the cylinder are kept: the height h_t is set so that 75% of the inlier points are encompassed around C_t. These inlier points are returned by the estimation procedure. We will denote this set as $\mathcal{P}_t$ (see figure 2.9, bottom right).

RBT produces a representation of the vasculature as a tree of center points C_t, each equipped with a tuple $\{r_t, \vec{d_t}, h_t, \mathcal{P}_t\}$. We call this information a *node*: each node gives a local picture of the blood vessel around its center.

Tracking the whole vessel tree

The previous paragraphs described one inner loop of our RANSAC-Based Tracking algorithm (RBT). The correction step of RBT, where a cylinder is fitted to candidate points, proved to be very robust to poor initialization of the cylinder parameters. As an example, the trackings for brain arteries, were initialized with the up vector direction $\vec{d_0} = (0, 0, 1)$, the average radius reported in the literature ($r_0 = 2mm$) and C_0 manually placed in the proximal portion of the internal carotid artery. The tracking started with the correction step.

Moreover, RBT can track a single branch at a time, but it does not stop at bifurcations. Instead, it recursively takes one bifurcating branch and tracks it until its distal end. According with the algorithm properties, this branch depends on its alignment to the

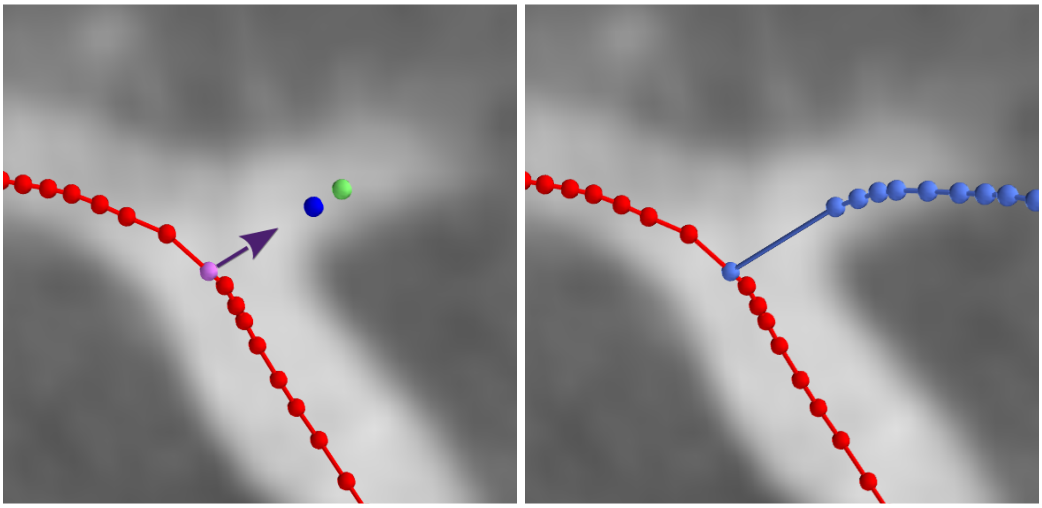

Fig. 2.10: Adding a new branch: (left) Initialize with a user-input point (green point), project it on the parent centerline (violet point). Their connection initializes the vessel direction (arrow). Tune the initial (green) point, by moving it along the vessel direction, so that it is out of the parent vessel, but still close to the proximal end of the child vessel (blue point). (right) Tracks the child branch from this point and connects it to the parent branch (stale blue polyline)

prior tracked centerline, its contrast and clarity, but may also be random, depending on the RANSAC sampling. To add a new branch, the user was asked to manually place a starting point $C_0^\star$ (see figure 2.10). This initial location was automatically tuned by projecting $C_0^\star$ onto the parent vessel centerline as C_0': the initial direction was $\vec{d}_0 = (C_0^\star - C_0')/|C_0^\star - C_0'|$ and the initial radius r_0 was set equal to the radius of the parent vessel. The initial point C_0 was set so that $C_0 = C_0' + 1.25 r_0 \vec{d}_0$.

Capturing aneurysms

Aneurysms do not comply well with the cylinder shape prior. A manual procedure was chosen to capture aneurysms, following [WNV00]: center points are placed within the aneurysm (1 or 2 points are enough in most cases), and rays are cast from each point, keeping the first location where the directional gradient is above a user-defined threshold to build the corresponding $\mathcal{P}_t$. The radius is estimated by fitting a sphere to each point set $\mathcal{P}_t$, in the least-squares sense, and center points are linked to complete the vessel centerline. The subtree corresponding to the aneurysm is attached to the RBT tree.

2.2.2 Implicit modeling: The LIM algorithm

RBT models the vascular tree as a tree of local point sets, around center points associated with a vessel radius estimate. This depiction is too rough and approximate for an accurate and realistic tool simulation to be conducted. The central idea of local implicit modeling (LIM) is to further enrich each node on this tree with a continuous and smooth representation of the local vessel surface as an implicit surface. Figure 2.11 displays the main steps in the reconstruction process for one node in the vicinity of a bifurcation. The same process is applied to each node in the vascular tree.

Implicit formulation

Implicit surfaces generated by skeletons are particularly well-suited for modeling smooth free-form shapes in a very compact and versatile way [BTC95]. They present good *locality* properties: skeleton objects far apart have no, or at least negligible, influence on each other [DOG04]. In particular, point set skeletons produce procedural implicit functions which are computationnally very efficient.

An implicit iso-surface generated by a point-set skeleton [Bli82] is expressed as the zero-level set $\mathcal{S}$ of a function f, a sum of implicit spheres:

$$f(X;p) = \sum_{j=1}^{N_b} \alpha_j \phi\left(\frac{|X - C_j|}{\rho_j}\right) - T \tag{2.5}$$

where $X\mathbb{R}^3$, $T \in \mathbb{R}^+$ is the iso-surface threshold, $\{\alpha_j\}$ are positive weights (height), and $\{C_j\}$ is the point-set skeleton. Each implicit sphere $\#j$ is defined by a symmetric spherical function, centered on C_j, of width ρ_j and following a radial profile. This profile (or *kernel*) is a function $\phi : \mathbb{R}^+ \to \mathbb{R}^+$, rapidly and monotonically decreasing to 0 and such that $\phi(0) = 1$, and ϕ has a bell-shaped graph [She99]. C^1 continuity around the center point imposes that $\phi'(0) = 0$. Though our implementation supports several kernels, all our experiments were realized using the Cauchy kernel: $\phi(x) = (1 + x^2/5)^{-2}$.

Muraki [Mur91] was the first to use a Gaussian-based model in the context of object reconstruction. Such models were called differently depending on the kernel used [She99]. Following the seminal work of [Mur91], we shall use the terms *blob* for an implicit sphere, and Blobby Model (BM) as a generic name for the implicit models f.

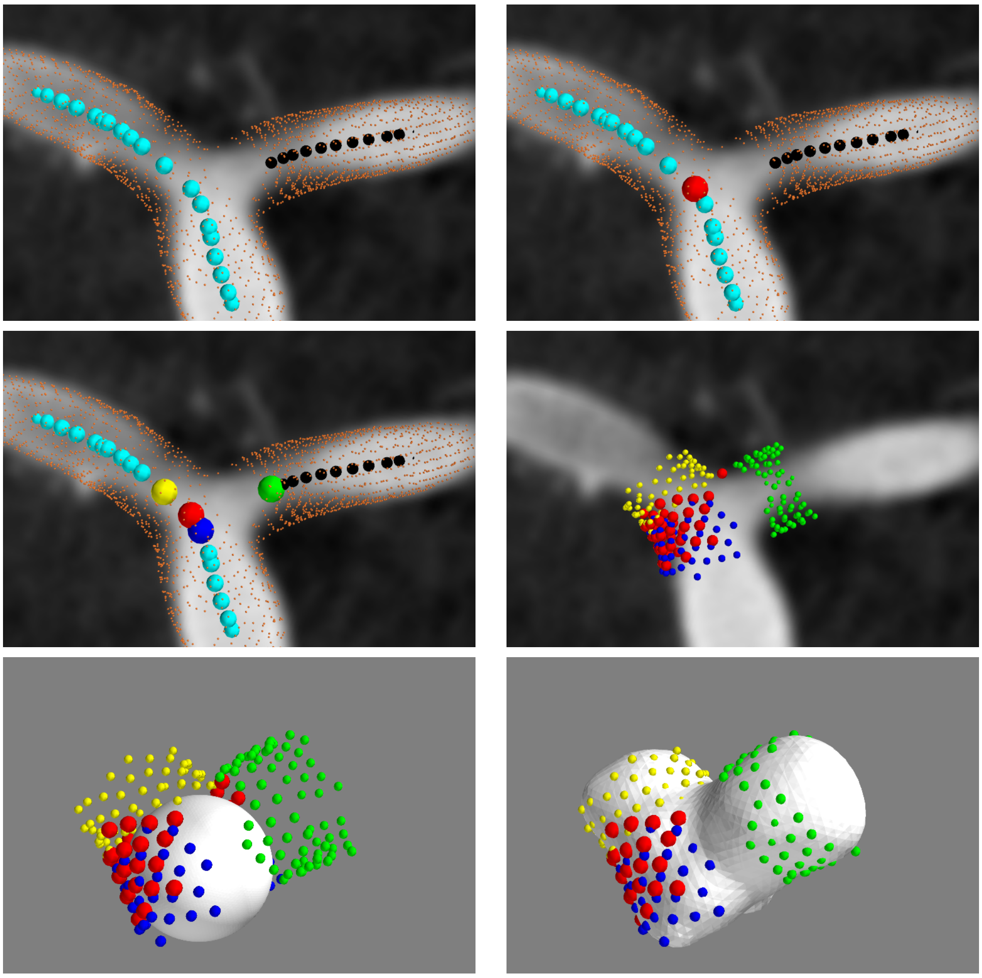

Fig. 2.11: Outline of the LIM algorithm. (top left) Input data: RBT for two branching arteries on 3DRA data results in points on the centerlines (blue and black points) equipped with points locally extracted at the vessel surface (orange dots); (top right) The red node is chosen. (middle left) Closest neighbor nodes are selected w.r.t a given topological distance (of one, here). (middle right) Local point sets are concatenated. (bottom left) The local implicit surface (blobby model) is initialized with two close spheres. (bottom right) LIM successively fits and splits blobs to fit the input points. 30 subdivisions were necessary to produce the resulting implicit surface.

In our particular simulation context, in order to help predict collisions, and have the function give a valid interpenetration direction, the algebraic value $f(X;p)$ at point X should relate monotonically to the geometric distance of X to the surface. We set $\alpha_j = \rho_j$, which obviously establishes the sought relation in the case of a single blob. Furthermore, redundancy in the implicit formulation of f is dismissed since height α_j and width ρ_j are dual in their role. As a consequence, the implicit function f is parametrized by $p^T = \{C_j^T, \rho_j\}_{j=1\ldots N_b}$, the vector of dimension $4N_b$, gathering centers and widths of the N_b implicit spheres composing the implicit function.

Energy Formulation

Fitting a surface to N_p points $\{P_i\}$ can be written as an energy minimization problem [Mur91; BTC95; TBC95]. We propose to combine 3 energy terms: $\mathcal{E} = \mathcal{E}_d + \alpha\mathcal{E}_c + \beta\mathcal{E}_a$ where $(\alpha, \beta) \in {\mathbb{R}^+}^2$, and:

- $\mathcal{E}_d = 1/N_p \sum_i f(P_i;p)^2$
  translates the algebraic relation between data points and the zero-level set. It gives a raw expression of the approximation problem.

- $\mathcal{E}_c = 1/\left(N_b(N_b-1)\right) \sum_{j \neq k} \left(\frac{s\sqrt{\rho_j\rho_k}}{|C_j - C_k|}\right)^{12} - 2\left(\frac{s\sqrt{\rho_j\rho_k}}{|C_j - C_k|}\right)^{6}$
  is Lennard-Jones energy. Each term is minimal (with value -1) for $|C_j - C_k| = s\sqrt{\rho_j\rho_k}$. $\mathcal{E}_c$ is repulsive for blobs closer than this distance, and attractive for blobs further away. It imposes some cohesion between neighboring blobs to avoid leakage where data points are missing, while preventing blobs from accumulating within the model.

- $\mathcal{E}_a = 1/N_p \sum_i \kappa(P_i)^2$
  $\kappa(P)$ is the mean curvature. It can be computed in a closed form at any point in space from the implicit formulation [Gol05]

  $$\kappa(P) = \frac{\nabla f^t H_f \nabla f - |\nabla f|^2 trace(H_f)}{2|\nabla f|^3}$$

  where ∇f is the implicit function gradient and H_f its Hessian matrix, both computed at point P. This energy smoothes the surface according to the minimal area criterion. In particular, the wavy effect that could stem from modeling a tubular shape with implicit spheres, is reduced.

Behind the rather classical form given above for the energy terms, it is important to notice that the whole energy is known under a closed-form expression. As a consequence, closed-form expressions were derived for its gradients with respect to the BM parameters $\{\rho_j\}$ and $\{C_j\}$.

Selection-Subdivision

Finding the appropriate number of blobs is very hard. Starting from one or few blobs, a subdivision scheme enables to progressively reach a compromise between a good model accuracy and a low complexity. The blob subdivision procedure proposed in the seminal work of Muraki was exhaustive and time consuming [Mur91]. A blob selection mechanism was added in [TBC95], measuring the contribution of each blob to $\mathcal{E}_d$ in a user-defined window, and choosing the main contributor. User input is not an option in our context where thousands of BMs should be handled. Moreover, we experimentally noted that this technique was prone to favor small blobs, thus focusing on details, before dealing with areas roughly approximated by one large blob. This behavior is caused by the selection mechanism using the algebraic distance to the implicit surface. Instead, our criterion relies upon the geometric distance approximation proposed by [Tau91] (see figure 2.12, middle left). First, we find the point P_{i^*} farthest to the surface:

$$i^* = \arg \max_{1 \leq i \leq N_p} \frac{|f(P_i; p)|}{|\nabla f(P_i; p)|} \tag{2.6}$$

Next, we select the blob $\#j^*$ whose isosurface is the closest to P_{i^*}:

$$j^* = \arg \min_{1 \leq j \leq N_b} \frac{|f_j(P_{i^*})|}{|\nabla f_j(P_{i^*})|} \tag{2.7}$$

with

$$f_j(P_{i^*}) = \rho_j \phi \left(\frac{|P_{i^*} - C_j|^2}{\rho_j^2} \right) \tag{2.8}$$

We thereby select the blob $\#j^*$ whose optimizatoin will most likely reduce the error at the worst fitted point P_{i^*}.

The subdivision step then replaces this blob with two new ones (figure 2.12, middle right). Their width ρ'_{j^*} is chosen such that two blobs, centered on C_{j^*}, of width ρ'_{j^*} would have the same isosurface as one blob centered on C_{j^*}, with width ρ_{j^*}. The first new blob is centered on C_{j^*}, while the second is translated by $\rho_{j^*}/10$ towards P_{i^*}. This small-shift procedure stabilizes the cohesion energy $\mathcal{E}_c$ which otherwise would become large when two blobs occupy the same location.

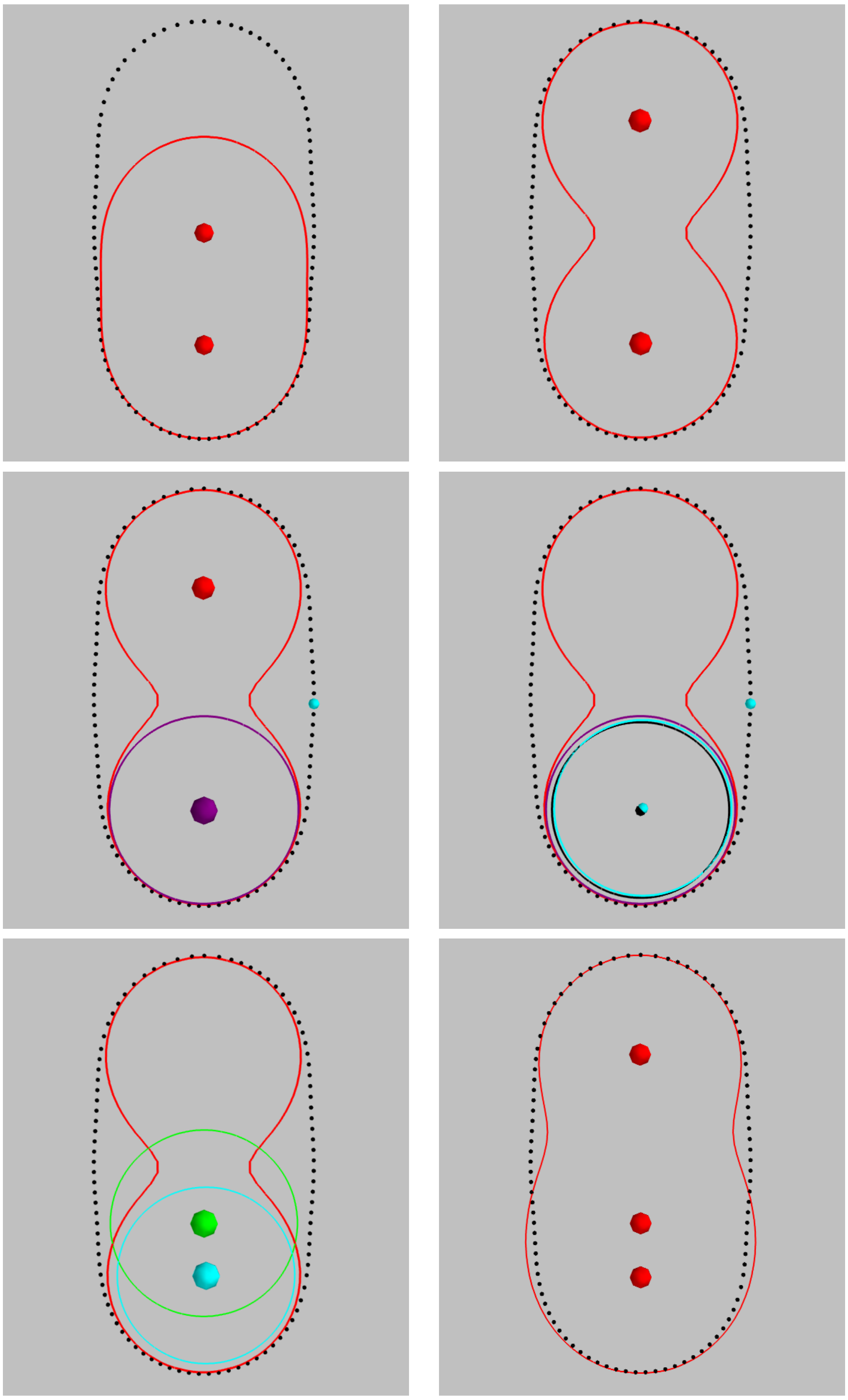

Fig. 2.12: The elementary reconstruction step in 2D. (a) Points (black) are to be reconstructed with two blobs (red contour). (b) First, all blobs are fine tuned over the centers and then, over the widths. (c) Second, find the point farthest to the contour (cyan) and the blob closest to it (purple). (d) Third, replace this blob with two blobs. The first (black contour) is placed at the same position (black) and the second (cyan contour) is translated in the direction of the farthest point (cyan). Widths are calculated so that both blobs centered at the black point generate the same isosurface as the fissioned blob (purple). (e) Fourth, the translated blob (cyan) is tuned over its center then width. (f) Finally, the BM is updated by integrating the recently tuned blob.

Optimization

Such an incremental subdivision procedure may lead to a dramatic increase in the number of blobs, and hence the size of the optimization problem. The locality of the kernel ϕ allows us to focus the optimization onto the newly created pair of blobs (figure 2.12, bottom left). More exactly, only the new blob that is slightly misplaced is optimized, the other blobs remaining constant. The energy is minimized using Polak-Ribiere (PR) gradient descent algorithm, taking advantage of the closed-form expressions of both the energy and its gradients. A single minimization loop consists in one PR minimization over the center (3 variables), followed by one on the width (1 variable). The optimization stops as soon as a maximum number of loops or a threshold accuracy t_g (as measured by Taubin's distance, see eq 2.6) is reached. In practice, a maximum of 5 loops proved sufficient. Threshold t_g will be discussed in Section 2.2.3.

Cleaning

Redundant blobs are either ejected far away from the surface during the optimization over the centers, or their width is reduced to almost zero during the minimization over the widths. A simple clean-up procedure was applied after each minimization loop: blobs relatively far from the node center (above 20 mm), and blobs whose width was below a certain size (0.02 mm i.e. one tenth of the voxel size) were removed from the BM. In combination with the subdivision process, this clean-up enables the algorithm to simulate large blob displacements, which is hardly possible with a local minimization, thereby adding robustness to poor initialization.

Initialization and global modeling

The vascular tree segmentation obtained with RBT is taken as input to our algorithm as a tree of nodes. In order to ensure smooth transitions between adjacent node BMs (figure 2.11, top right), the local data point sets $\mathcal{P}_t$ are concatenated so as to create overlaps between neighbors. The input point set considered to be fitted by LIM is therefore $\{P_i\}_t = \bigcup_{k \in \mathcal{N}_t} \mathcal{P}_k$ with $\mathcal{N}_t$ a neighborhood of the node of interest, defined by all nodes within a maximum topological distance $\mathcal{T} = 2$ in the tree in our implementation.

First, the initial BM is constituted of two blobs placed on either side of the node center C_t along the vessel direction $\vec{d_t}$ so that an elongated shape is formed. The

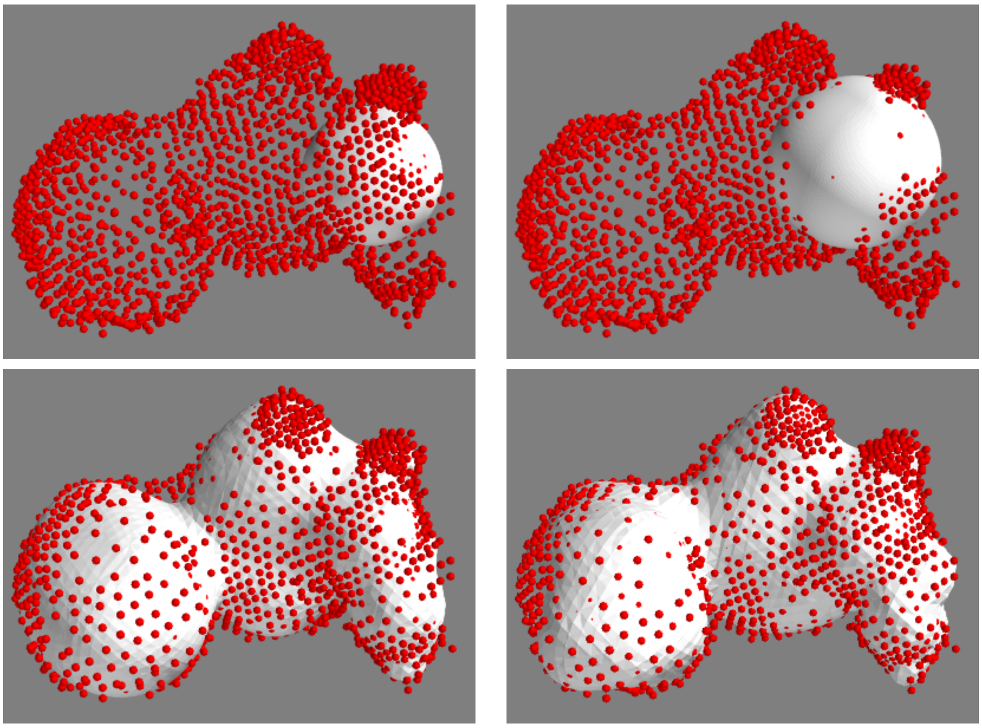

Fig. 2.13: Implicit modeling of an aneurysm. The points $\{P_i\}$ are in red. (From left to right) Initialization with a single blob; after the first minimization; after 25 subdivisions; final result (100 subdivisions)

width ρ_t is scaled to match the shape of a sphere with radius r_t (see figure 1.14, bottom middle. This match depends on ϕ).

Then, an implicit surface which fits the point set $\{P_i\}_t$ is produced through selection, subdivision and optimization of the blobs as described above. The process is repeated until the maximum distance of the blobby model to the point set falls below threshold t_g or a maximum number N_s of blobs is reached. Each local BM is treated independently of others, thus enabling parallel computation. Each initial node is enriched with a local BM $\mathcal{B}_t$, resulting in a global model of the vasculature as a tree of implicit functions.

Figure 2.13 illustrates the essential steps of this fitting algorithm and its capacity to model complex shapes, such as aneurysms, even from rough initialization.

2.2.3 Results

To show the strength of the proposed framework, we decomposed our assessment in two parts. First, we compared RBT against state-of-the-art Multiple Hypothesis Testing (MHT) algorithm [Fri+10] on clinical data. Next, the LIM algorithm was tested on synthetic and clinical data. A more complete description of the experimental protocol is available on our journal publication in *Medical Image Analysis* [Ker+17].

We considered 10 patients scheduled for the endovascular angioplasty of an intracranial aneurysm at the Department of Interventional Neuroradiology, University Hospital of Nancy, France. Each patient data set consisted of a 3D Rotational Angiography (3DRA) acquired on a vascular C-arm (Innova 4100, GE Healthcare) during the intra-arterial injection of the internal carotid artery. 3DRA volumes presented as a 512^3 isotropic voxel cubes, with a voxel size between 0.18-0.22 mm.

Evaluation of the RBT algorithm

Assessing the tracking ability A tracking was considered as successful if the resulting centerline remained inside the vessel of interest. All 744 vessels were visually inspected to compute this Success Rate (**SR**) in percents.

The MHT tracking failures were then visually, manually cut before the problem occurred (see figure 2.14 for an example). No such cut was ever required for RBT. The lengths of the centerlines were computed and summed up to give the Total tracked Length (**TL**) in millimeters.

Each vessel was thereafter classified as: *short*, *medium*, or *long*, if the centerline was respectively correct along less than 33%, 33-66%, more than 66% of the visually estimated length of the targeted vessel. The success rate was recomputed, considering as successes only medium and long vessels. We denote this score **SRL** in percent.

Then the Common path Length (**CL**, in millimeters) could be computed as the total tracked length on those vessels classified as medium or long by both algorithms.

We assessed the distance between two centerlines with a Modified Average Symmetrical Distance (**MASD**):

$$\mathrm{MASD} = \frac{1}{N' + M'} \left\{ \sum_{i}^{N} d_w(P_i, \mathcal{Q}) + \sum_{j}^{M} d_w(Q_j, \mathcal{P}) \right\} \qquad (2.9)$$

	MHT				RBT			
	SR	SRL	TL	CL	SR	SRL	TL	CL
mean	64.9	68.8	778.6	680.9	93.5	88.7	1446.1	727.6
min	48	57	555.4	389.0	81	77	833.9	403.6
max	74	77	1086.9	1074.1	100	99	2373.6	1164.7

Tab. 2.1: Evaluation of RBT compared to MHT. SR and SRL are given in percents, TL and CL are given in mm. The mean value was computed over the 10 patients.

where $\mathcal{P} = \{P_i\}_{i \in [1,N]}$ is the centerline produced by MHT, and $\mathcal{Q} = \{Q_j\}_{j \in [1,M]}$ is produced by RBT. d_w is the classical Euclidean distance between a point and a curve, but thresholded by w: it returns 0 whenever the Euclidean exceeds w. Consequently, N' and M' are the number of points respectively in $\mathcal{P}$ and $\mathcal{Q}$ where the distance was not thresholded. The MASD measure automatically selects the portions common to both centerlines and computes the mean distance between them (see last row of figure 2.14).

Two values were used for w: $w = 3$ and $w = \bar{r}$, the average radius of the tracked vessel. Similarly low results would prove the capacity of the measure to consistently select the correct common portions of the vessel centerlines.

Table 2.1 compares MHT to RBT according to the above measures, averaged over the 10 patients. Mean values are reported along with their minimum and maximum values.

RBT displays a SR of 93.5% compared to only 64.9% for MHT. This success rate is confirmed by the SRL, with two precisions. First, a slight increase was observed for MHT (68.8%) since the results were edited. It reintroduced vessels which, for example, were well tracked but for MHT failing to stop (see e.g. figure 2.14, top row, middle). Second, a small decrease in SRL was observed for RBT, confirming its tendency to sometimes stop prematurely. The 20-25% difference in the success rate scores was due to MHT often failing to track a vessel that came close to another dense structure, so-called Kissing Vessel (KV) issue, and to leak into that second structure. Figure 2.15 illustrates the difficulty of MHT to sometimes handle KV, while RBT demonstrates a high robustness to that problem and can therefore track even very tortuous vessels.

When both algorithms succeeded, on average, RBT went further (CL = 725.5 mm) than MHT (CL = 680.9 mm). Nonetheless, MHT definitively delivered a lesser number of successful trackings which impacted negatively the average tracked length per patient (TL) down to 778.6 mm against 1446.1 mm for RBT.

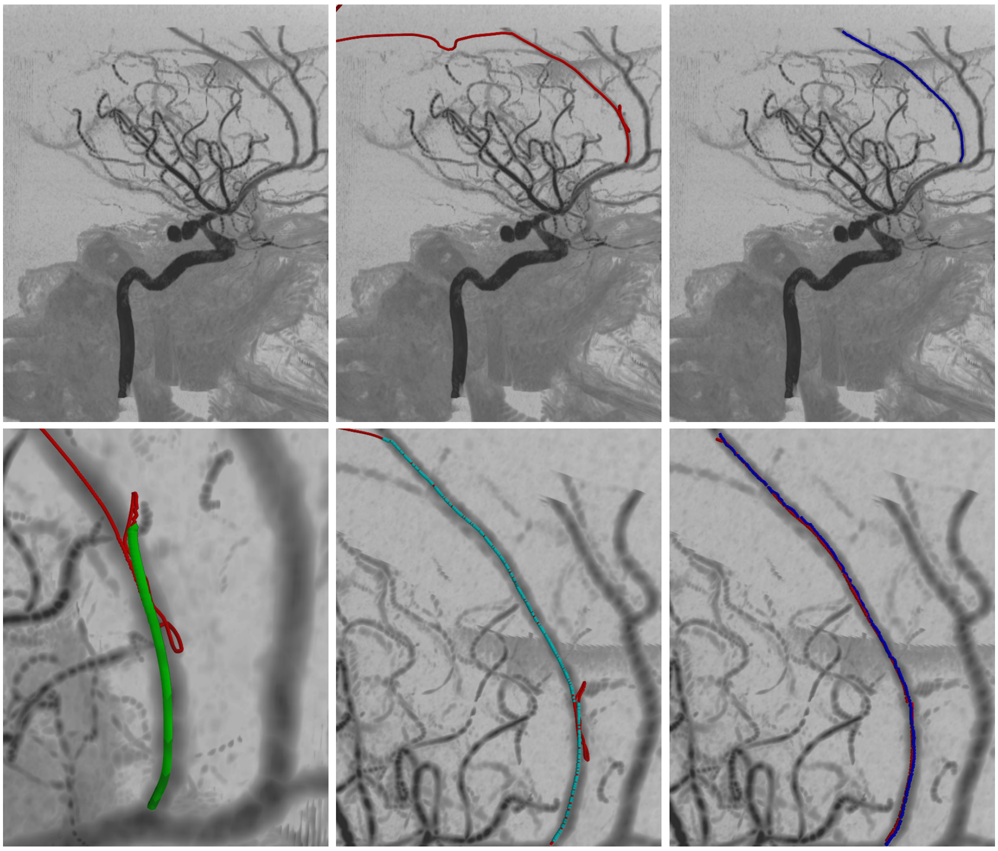

Fig. 2.14: Top: (left) Maximum Intensity Projection of one patient data. Centerline delineation produced by MHT (middle) and RBT (right). Bottom: (left) When the MHT centerline (red) does not remain inside the vessel wall, it is cut – for TL computation – before the problem arises (green). (middle) MHT centerline (red) and the points (cyan) selected for MASD computation ($w = \bar{r}$). (right) The resulting points for MHT (red) and RBT (blue, all the original points) used for MASD computation.

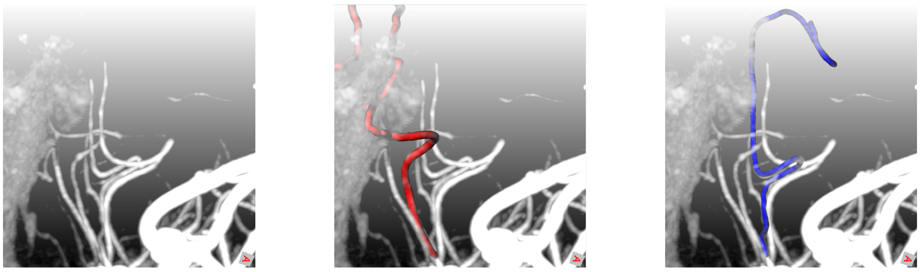

Fig. 2.15: (left) A tortuous branch of the posterior choroidal artery (0.6 – 0.7 mm of diameter) in Patient 3. (middle) MHT is misled by neighboring structures in the proximal portion of the artery whereas (right) RBT tracks the tortuous vessel and successfully handles the Kissing Vessel (KV) issue.

The average MASD between both centerlines, with both 3 voxels and the mean radius of the targeted vessel, was 0.18 mm (down to 2 figures of precision) and was below one voxel for all patients (min=0.16 mm, max=0.21 mm with a voxel size between 0.18 and 0.22 mm in our patient data set). This showed that RBT produced similar results as MHT.

Evaluation of our LIM algorithm

After applying RBT to the carotid artery of one patient, one node of the centerline was considered. The energy weights were tuned to provided energy terms of the same order of magnitude. The isolevel value T was chosen to be approximately half the voxel size. Other values were chosen to produce visually good results. In particular, for Lennard-Jones energy, s was set to 2: Two blobs with the same width ρ are thereby separated by 2ρ at the minimum for this energy. Values are summarized in Table **??** and where used for all synthetic and patient tests.

Synthetic experiment Four synthetic shapes were used in a first experiment. They consist in skeleton-based convolution surfaces:

- a capsule (**C**) based on a 4 cm segment skeleton
- the same capsule opened at both extremities (**o**C)
- an arc (**A**) based on a 4 cm radius half-circle
- a bifurcation (**B**) composed of two portions of arcs.

These shapes are displayed in blue on figure 2.16. There were tuned so that their width (distance to their skeleton) was 1 mm. Each shape was sampled on 300 points using an equi-distributed point-based sampling technique [**witkin94**]. These points served as input to the LIM algorithm (point set called $\mathcal{P}_t$ in section 2.2.2).

Protocol Each point in $\mathcal{P}_t$ was perturbed by a white Gaussian noise along the normal to the reference surface. The standard deviation of the noise varied from 0.025 to 0.25 mm (step 0.025, 10 levels of noise). LIM was applied 30 times for each noise level, with t_g set to 3 times the standard deviation. N_s was set to a large value (100) in order to evaluate the capacity of LIM to produce compact models (i.e. blobby models with a reduced number of blobs). LIM initial BM contained 2 (C and oC) or 5 (A and B) blobs. The accuracy of LIM was evaluated by robust statistics on the Euclidean distance between $\mathcal{P}_t$ (noise free version) and the resulting blobby

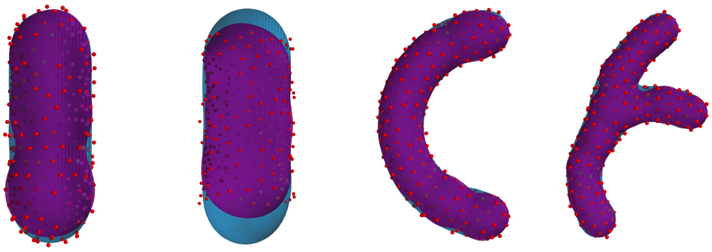

Fig. 2.16: Reference surface (blue) and the resulting BM (purple) for maximal values in Table 2.2. The 300 noisy input points are in red.

model: The output BM was sampled on 1000 points (again using [**witkin94**]) to compute the distance of each point in $\mathcal{P}_t$ to the BM and the 90th percentile was taken: this score is denoted d. The number of blobs in the output BM was also recorded.

LIM relies on the distance approximation to an implicit surface proposed by [Tau91]. We took here the opportunity to evaluate the adequacy of this approximation and computed it together with the Euclidean distance. The 90th percentile is also reported, and denoted d_a.

Result Table 2.2 reports the minimum, median and maximum of both d and d_a for the 300 tests, as well as the number of blobs in the final BM.

Excellent distance figures were recorded, with a low median value close to the minimum and a maximum value below the maximum standard deviation of the applied noise. A higher median value was observed for the open capsule oC which exposes a more challenging fitting problem due to its open extremities. Figure 2.16 displays LIM output for the recorded maximum d value. We can see that the points at maximum distance are located in the vicinity of the open extremities. This issue is tackled in our case by letting successive BMs overlap.

The number of blobs in the final BMs is typically low and demonstrate the capacity of LIM to produce compact models. Overly large BMs were seldom obtained when the noise process randomly applied large displacements to some points. LIM is indeed not robust but the filtering task is devoted to RBT.

The approximate distance d_a gave very similar results to d except for large values which it tended to underestimate. The ordering of points according to their distance to the implicit surface was nevertheless always the same with both distances, which makes the use of the approximate distance appropriate in LIM.

Shape		C	Co	A	B
d	min	0.015	0.039	0.016	0.048
	med	0.042	0.119	0.063	0.078
	max	0.189	0.233	0.174	0.334
d_a	min	0.015	0.038	0.016	0.046
	med	0.041	0.103	0.064	0.079
	max	0.164	0.175	0.146	0.211
N_b	min	5	5	8	12
	med	7	9	15	15
	max	89	83	102	15

Tab. 2.2: Evaluation of LIM accuracy and compacity on 4 synthetic shapes (capsule C, open capsule oC, arc A and bifurcation B) perturbed by a Gaussian noise. d is the 90th percentile of the Euclidean distance of noise free points in $\mathcal{P}_t$ to the output BM. d_a presents the same statistics using the approximate distance proposed by [Tau91]. N_b is the number of blobs in the output BM. Minimum (min), median (med) and maximum (max) values are reported over 300 tests.

Reconstruction on patient data Input data was provided by RBT algorithm which was first run on the carotid artery (the stem vessel of the vascular tree) and subsequently, all vessels were tracked (see Section 2.2.1). A total of 379 instances of RBT were needed (between 26-56 instances per patient). Moreover, a total of 11 aneurysms were segmented with the algorithm described in Section 2.2.1. A total of 87564 BMs were to be fitted by LIM on these patient data. Parameters used (see Table **??**) offer LIM good convergence properties for nice visual results. We first assessed this visual quality.

The accuracy however depends on two parameters that required more care to be fixed. N_s is the maximum number of subdivisions: the larger N_s, the more blobs, allowing for greater modeling versatility; t_g is the maximum error allowed for LIM: this error is used to determine $i^\star$ (see eq. 2.6). We tested 3 values for both N_s ({30,50,100}) and t_g ({0.2,0.3,0.5}, in mm). The resulting 9 configurations were evaluated based on precision and compacity of the output model.

Visual assessment Local BMs generated by LIM do not assemble into a representation suitable to the visualization of the global vessel tree. A rather good approximation can however be given by first meshing each local BM (we used marching cubes), then cropping each local surface into its Voronoi cell (see Section **??** for a precise definition). Finally all these local surfaces are visualized together for a given BM tree. An example is given in figure 2.17.

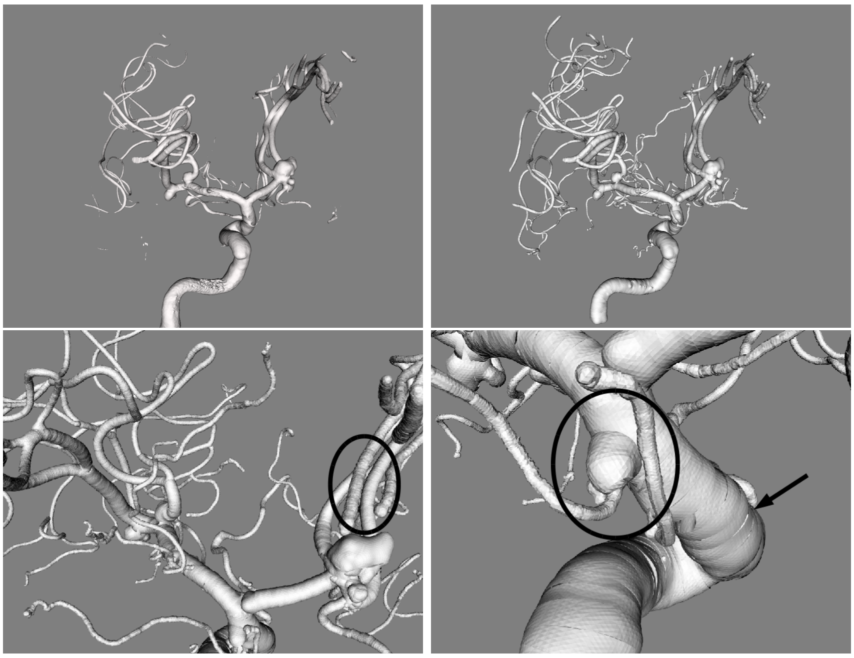

Fig. 2.17: Visual assessment of LIM: (top-left) isosurface of 3DRA data; (top-right) LIM result, showing much more vessels; (bottom-left) no unwanted blending at kissing vessels (encircled); (bottom-right) difficulty to sometimes model branching of a tiny vessel on a large one (encircled), small discontinuities are visible between adjacent BMs (arrow).

LIM was able to reconstruct both tiny and large vessels, and capture well even tortuous vessels. Even though each BM is processed independently from its neighbors, our overlapping neighboring point sets produced smooth transitions between BMs. A visual comparison with a classical isosurface extraction revealed that more vessels are visible with our proposal (see figure 2.17, second to left). Kissing vessels were well handled and no unwanted blending occurred (see figure2.17, second to right). Bifurcations were correctly handled. Some convergence issues were recorded in some places where a very small vessel branches onto a large vessel (e.g. the anterior choroidal artery on the internal carotid artery, see figure 2.17, right).

Precision In the absence of ground truth, we resorted to the statistics on the distance approximation called d_a in Section 2.2.3. Our synthetic experiment indicated d_a was a good estimate of the score d based on the Euclidean distance.

Blobby Model outputs (87654) were separated into 4 classes based on their d_a score: $C_1 \equiv d_a < 0.5\,v_s$, $C_2 \equiv 0.5\,C_3 \equiv v_s \leq d_a < v_s$, $C_4 \equiv v_s \leq d_a < 2\,v_s$ and $2\,v_s \leq d_a$. The voxel size v_s varies between 0.18 and 0.22 mm per patient and is related to the

t_g	0.5mm			0.3mm			0.2mm		
N_s	100	50	30	100	50	30	100	50	30
C_1	51.37	51.37	51.37	88.65	88.63	88.54	97.15	96.96	96.58
C_2	47.67	47.64	47.61	11.00	10.96	10.97	2.60	2.73	3.01
C_3	0.84	0.85	0.86	0.25	0.28	0.34	0.15	0.20	0.26
C_4	0.12	0.14	0.16	0.10	0.12	0.15	0.09	0.11	0.14

Tab. 2.3: Distribution in % of the BMs according to the error of fit d_a in 4 classes (left column): C_1 corresponds to BMs with $d_a < 0.5\,v_s$, C_2 to $0.5\,v_s \leq d_a < v_s$, C_3 to $v_s \leq d_a < 2\,v_s$ and C_4 to $2\,v_s \leq d_{bm}$. v_s is the voxel size. 9 algorithm configurations were investigated depending on parameters t_g (targeted precision of fit) and N_s (maximum model complexity). Computations implied 87564 BMs.

point extraction noise in RBT. Table 2.3 reports the distribution, in percents, of d_a among the 4 classes.

99% of BMs present sub-voxel d_a ($C_1 \bigcup C_2$) for all configurations. Moreover, N_s does not appear to have any influence on the precision of fit, which is governed by t_g. Besides, a precision of $t_g = 0.2$ mm led to less smooth models where LIM had a tendency to try and adjust to noise in the input point set. $t_g = 0.3$ mm was the best compromise between smoothness and precision.

Compacity A measure of compacity is given by the number of blobs in a BM. A first measure of compacity was the total number of blobs in the BMs required to model a patient's vasculature. We found out that this number did not depend on N_s and we hereby report only figures for $N_s = 100$. The average number of blobs per patient was: 33930 ($t_g = 0.5$ mm, average of 3.9 blobs per BM), 56395 ($t_g = 0.3$ mm, average of 6.4 blobs per BM), and 85733 ($t_g = 0.2$ mm, average of 9.5 blobs per patient).

The number of blobs is the number of primitives required to encode the implicit surface. In the case of a triangular mesh, a similar measure is given by the number of triangles. Therefore, we computed for each patient, the ratio between the number of triangles in a mesh representation of the surface, and the total number of blobs in the BMs used to implicitly model the whole vasculature: It indicates the ability of LIM to compress the surface representation. Results are reported in table 2.4. For a targeted precision $t_g = 0.3$ mm ($N_s = 100$), the expected compression ratio is over 100.

t_g (mm)	$\frac{\#\triangle}{N_b}$		
	min	med	max
0.5	159	234	308
0.3	73	104	138
0.2	44	58	77

Tab. 2.4: Ratio between the number of triangles $\#\triangle$ in a triangulated surface and the number of blobs N_b in the local implicit model for 3 values of t_g ($N_s = 100$). Minimum (min), median (med) and maximum (max) values are reported for 10 patients.

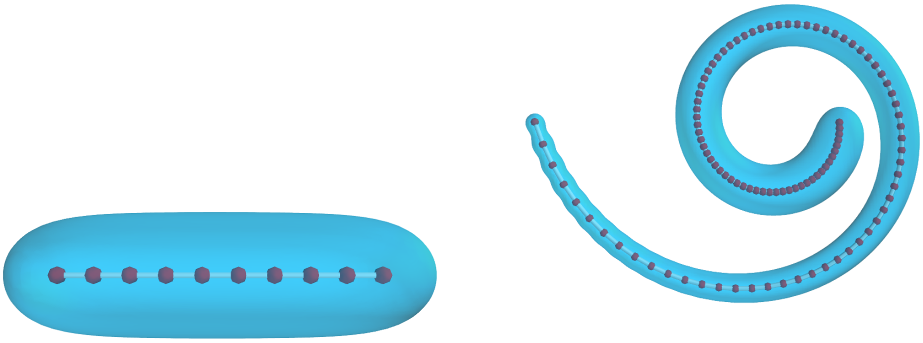

Fig. 2.18: Data used for validation: capsule (left) and spiral (right) surfaces. Both synthetic shapes presented respectively dimensions (width×height×depth) in mm: $11.9 \times 2.5 \times 2.5$ and $8.1 \times 6.12 \times 1.05$. A primitive was placed at each red dot composing the skeleton (white).

Use for interactive simulation

One expected benefit of using implicit surfaces is the reduced collision management time. To assess the relevance of LIM, we consider two synthetic models. A *capsule* (figure 2.18 left) was synthesized from a 10 mm line segment skeleton sampled on 10 points, with a radius of 1.25 mm. It provides the most simple vessel shape. A *spiral* (figure 2.18 middle) was generated from 100 points on a curve line with polar equation (ρ, θ) s.t. $\rho = \dfrac{\lambda\pi}{\theta^2}$ with $\lambda \in [15.75, 63]$ and $\theta \in [\pi, 4\pi]$. The shape radius varied from 0.15 mm to 0.5 mm. A smooth surface was obtained in both cases as a convolution surface using Cauchy kernel.

Collision with an implicit surface is easily detected through the sign of the implicit function: in our case, a point crossed the surface if f, the local BM function, became negative (see Equation 2.5). A node must be selected in the tree output by RBT and LIM to determine the local BM. The node, whose center is the closest to the colliding point, is not appropriate. First, between two time steps, the point could occasionally jump from one artery to another one, e.g. in the case of kissing vessels, which is mechanically impossible. Therefore, after motion, a point is associated to either the same node as before, or one of its topological neighbors in the tree (see figure 2.19).

Second, selecting the closest node resorts to finding the cell the point belongs to in the Voronoi diagram of the node centers. This strategy fails where a small vessel branches onto a larger one: The BM modeling the proximal portion of the small vessel might be selected while the tool point is still inside the large vessel. Using a power diagram enables to adapt the size of the cell to the estimated vessel radius r at the node. This diagram is generated with the power pseudo-distance :

$$d^p(X, C) = |X - C|^2 - r^2 \tag{2.10}$$

where X is the tool point, C the node center and r the estimated vessel radius at the node. After motion, the point is associated to its closest candidate node according to d^p.

At initialization, all the nodes in the tree are candidates for the proximal point of the tool. The d^p-closest node is selected for this point. Then, each point is successively associated to its d^p-closest node, in the neighborhood of the node selected for the previous point.

The average time taken to detect and solve one collision was measured both for implicit LIM and mesh models. Results are reported in Table 2.5.

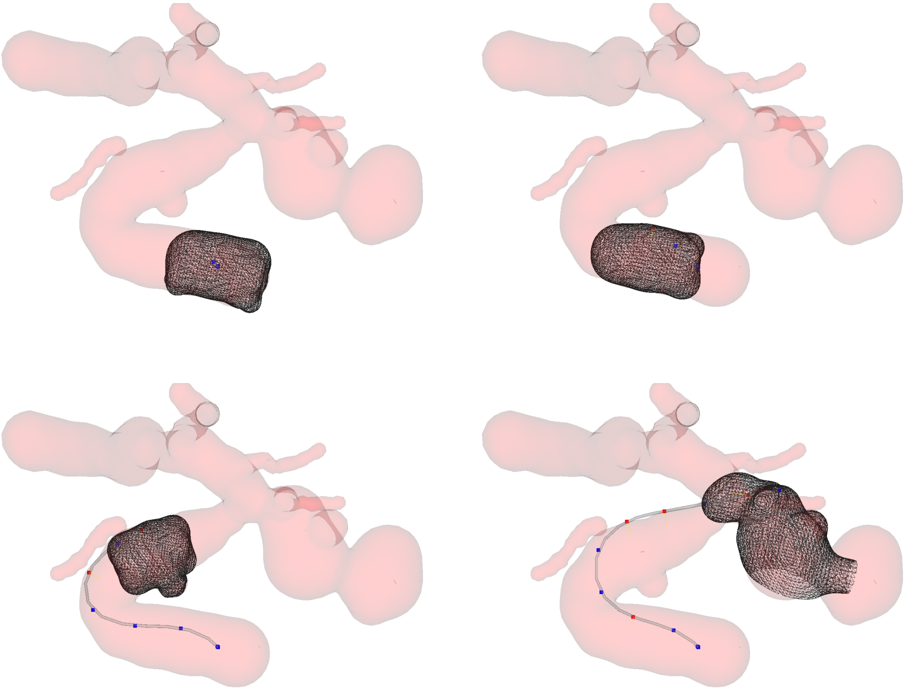

Fig. 2.19: The surface of the local BM selected to solve contact at the tool tip point is displayed in wire-frame for 4 simulation steps. The overall vessel surface is shown in transparent red as a mesh.

Collision management is significantly faster with LIM models than with triangular meshes (about two orders of magnitude). In fact, collision management time does not depend on the total number of primitives for LIM: the capsule have 12k blobs and the spiral 28k blobs but they display similar computation times. This time only depends on the number of blobs in the local selected BM, at most a few tens whatever the complexity of the global shape. BM selection is also done in constant time since we restrict the search to topological neighbors of the current BM.

2.3 Models for the pelvic system

The strategy conducted in the previous section shows the benefits of having geometric models dedicated for simulation. Skeleton-based implicit surfaces were convenient in the context of vascular geometry thanks to some assumptions that eases the process of defining the implicit function given a vessel network. However given an arbitrary geometry, the search for a implicit function may be computationally intensive. Other

	# of primitives	Time (msec)	# of contacts
Capsule (Mesh)	12k triangles	4.89	51
Capsule (LIM)	12k blobs	0.0232	50
Spiral (Mesh)	2.74k triangles	1.09	79
Spiral (Mesh)	11.3k triangles	1.84	80
Spiral (Mesh)	45k triangles	5.58	80
Spiral (LIM)	28k blobs	0.0219	80
Phantom (Mesh)	100k triangles	16.23	80
Phantom (LIM)	42k blobs	0.133	82

Tab. 2.5: Computation timings for collision detection on various deployment scenarios, using state of the art implementations. For a comparable amount of primitives, LIM outperforms triangular meshes for collision detection and makes it easier to achieve interactive simulation.

limitations needs also to be addressed: the possibility to track several organs / soft tissues simultaneously and to track them over time like in dynamic medical imaging (dynamic MRI for instance). Therefore this section uses another representation (B-splines) to represent anatomical structures that will undergo mechanical simulation. This section takes place in the context of female pelvic medicine, where image-based diagnoses of pelvic floor disorders like prolapse or endometriosis are performed. These pathologies rely on mechanical indicators, such as mobilities of organs and shear displacements between organs but image data do not provide directly precise and global values of these indicators. Since the methodology used for this problem is the same as previous, a short overview of the approach and the results will be presented. The reader may refer to [Jia17; Jia+15; Jia+17; Jia+18] for details.

2.3.1 Overview of the approach

The chosen approach can be formulated as an optimization procedure. Four key parts are involved in such optimization:

- input data (3D static and 2D dynamic MR images of the patient),
- a mathematical model with variables to be optimized (B-spline Model),
- a cost function, which links the model to the input data (e.g.integration on the domain of the model), and
- an optimizer, which finds the optimal values of the parameters to minimize the cost function.

The optimization process can be described as iterative updates of its DOFs. As we deform the geometric model, we optimize the DOFs that describe the geometrical shape. The geometric model is considered as a mapping from DOFs to the geometry. We introduce two mappings: (1) an affine transformation for the coarse registration and (2) a cubic B-spline as the shape descriptor for the deformable registration. The control points are the researched DOFs. Thus, similar with the typical image registration, our model-to-image registration method is also based on a multi-scale framework.

Input Data The input experimental image data consist of T2-weighted static and dynamic MRI of the female pelvic system. The use of these images of volunteers for our research was approved by the National Ethics Committee (*Comité d'Ethique de la Recherche en Obstétrique et Gynécologie CEROG 2012-GYN-06-01-R1*). The static MR images are obtained in the three planes (sagittal, axial and coronal), which provide information on the 3D anatomical organization. The dynamic MR images (or Cine MRI) refer to a temporal sequence of 2D images, which are widely used for diagnosing pelvic sagging pathologies. For our study, these 2D dynamic images were obtained in the same midline sagittal plane of the patient during pushing, for a given frequency (about 1.2fps). The choice of this middle plane keeps a standard procedure in the clinical routine because it is the most representative of the organ shapes and motions. In order to increase the image contrast of pelvic organs, a gel had been injected into the vaginal cavity and the rectum while patient drank liquid to highlight the bladder. In this way, pelvic organs were easily observable during MRI acquisition. We were interested in 2D segmentation of the three organs (bladder, vagina and rectum), for which both 2D sagittal static and dynamic MR images were used (spatial resolution from 0.47 to 1.17 mm/pixel).

B-Spline Model For modeling the geometries of the three organs, we used 2D B-spline of 3-degree that is a classical geometric modeling tool. In our case, each organ is modeled by a closed B-spline $\mathcal{M} : u \in [0,1] \to \mathcal{M}(u) \in \mathbb{R}^2$. Each position on the curve can be calculated by the value of u:

$$\mathcal{M}\left(u, [\mathbf{P}_0, \mathbf{P}_1, \cdots \mathbf{P}_l]\right) = \sum_{i=0}^{l} \mathcal{N}_{i,p}(u)\mathbf{P}_i \tag{2.11}$$

where $[\mathbf{P}_0, \mathbf{P}_1, \cdots \mathbf{P}_1]$ are the $l+1$ control points. However, the first and last control point of each curve are attached to form a closed curve: $\mathcal{M}(0) = \mathcal{M}(1) = \mathbf{P}_0 = \mathbf{P}_l$. Hence, our model is analytical and of $\mathcal{C}^2$ continuity except at the end point. Under

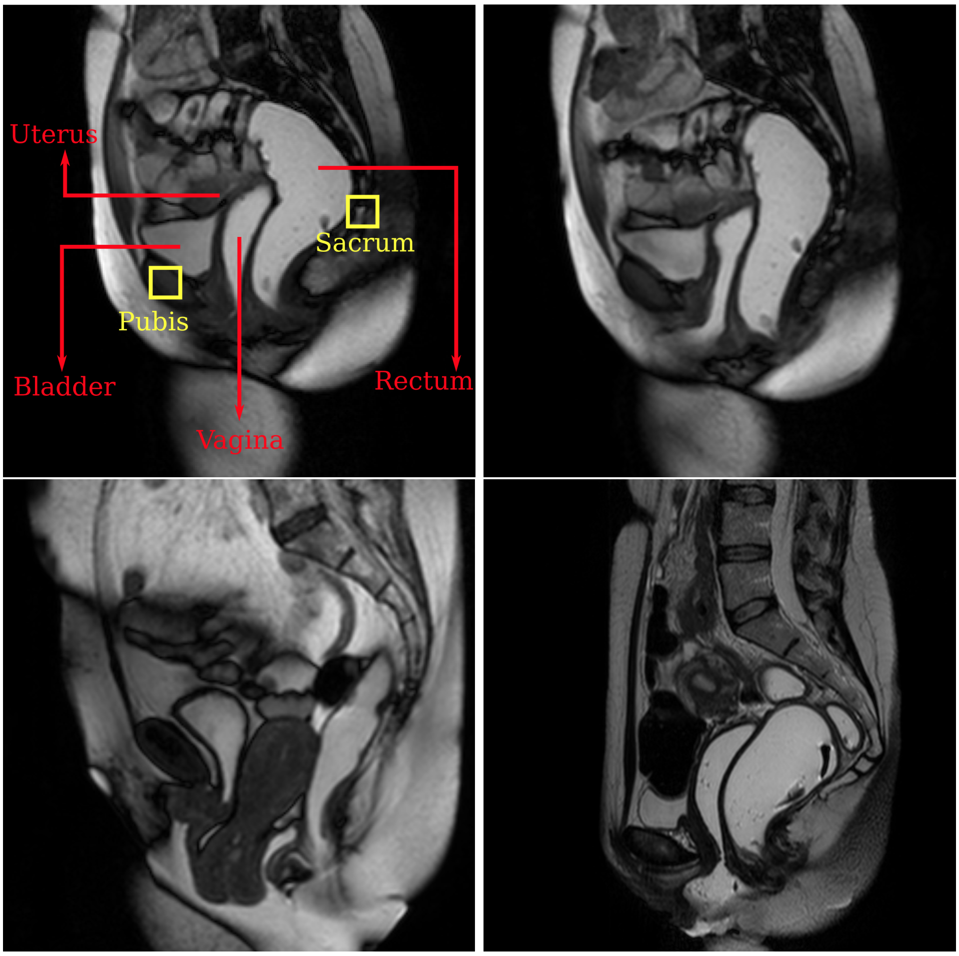

Fig. 2.20: Sagittal dynamic magnetic resonance (MR) image (spatial resolution = 1.17 mm/pixel, 256*256 pixels. (top): First and last images of a dynamic MRI sequence of a healthy volunteer. (bottom-left): dynamic MRI of a prolapsus where the uterus moved down. (bottom-right): static MRI of endometriosis

this configuration, the l control points are supposed to be the DOFs in the registration algorithm. Another advantage of the B-spline is its locality property, which means each control point is highly independent. In addition, for the affine transformation step, we have the relevant mapping $\mathcal{M}_A$, six DOFs of which are evaluated in this coarse step: $[T_{11}, T_{12}, T_{21}, T_{22}, T_x, T_y]$. Suppose $\mathcal{M}^0$ is the mapping function corresponding to the initial B-spline curve, and $\mathbf{C}$ the center, then the mapping function of the affine transformation becomes:

$$\mathcal{M}_A\left(u, [T_{11}, T_{12}, T_{21}, T_{22}, T_x, T_y]\right) = \begin{bmatrix} T_{11} & T_{12} \\ T_{21} & T_{22} \end{bmatrix} \left(\mathcal{M}^0(u) - \mathbf{C}\right) + \begin{bmatrix} T_x \\ T_y \end{bmatrix} + \mathbf{C} \tag{2.12}$$

Cost Function In order to define an appropriate cost function, we introduce a virtual image to form the first energy term. A so-called virtual image is generated from the model for calculation of a cost function, which finds the best correlation with the real image. This virtual image is created in the narrow band Ω along the contour with a certain width. The value of grey levels in this narrow band image is chosen to be similar to the ones in the real image (grey level MR image). This idea was first introduced and proved by Semin et al. [SFA10] to detect fiber-like objects in digital images. This approach was developed then by Réthoré et al. [RF14]. The intensity profile of the virtual image is defined by a levelset function $\mathcal{L} : v \in \mathbb{R} \to \mathbb{R}$ where v is the distance from a position $\mathbf{C}$ to the contour (Equation eq 2.13).

$$\mathcal{L}(v) = \begin{cases} A_{\text{max}} & \text{if } v < 0 \\ A_{\text{min}} + \frac{A_{\text{max}} - A_{\text{min}}}{2} * \left(1 + \cos\left(\frac{\pi v}{\tau}\right)\right) & \text{if } 0 \le v \le \tau \\ A_{\text{min}} & \text{if } v > \tau \end{cases} \tag{2.13}$$

where τ is the estimated width of narrow band Ω and A_{max} and A_{min} the grey levels inside and outside organ. The value of A_{max} and A_{min} are chosen by clicking on the foreground and background in the real image.

$$\mathcal{F}(D) = \begin{cases} A_{\text{max}} & \text{if} \quad D < -\lambda \\ \frac{A_{\text{max}}}{4\lambda^2}(D - \lambda)^2 & \text{if} \quad -\lambda \le D \le \lambda \\ 0 & \text{if} \quad D > \lambda \end{cases} \tag{2.14}$$

The virtual image I_Y is then computed on the discrete points cloud over the narrow band of the organ border. The discrete points form actually a bended grid, a position $\mathbf{X}(u, v)$ of which is defined in the curvilinear coordinate system based on tangent and normal direction of the contour. The virtual image value $I_v(\mathbf{X})$ is computed in the analytical way (Equation 2.15) so that the grid spacing size can even be much smaller than the pixel spacing in real image. Unlike the virtual image, the real one has a pixel-wise square grid; we should then project $\mathbf{X}$ and evaluate real image value $I_r(\mathbf{X})$ using a bi-cubic interpolation. Also, for these reasons, the virtual image is considered *virtual* and provides sub-pixel information compared with the real one. Furthermore, grey level values are merely evaluated in its definition domain Ω instead of the whole domain of the real image.

$$I_v(\mathbf{X}) = I_v(u, v) = \mathcal{L}(v) \tag{2.15}$$

The positions X can be evaluated by the analytical formulation of the parametric geometric model (Equation 2.16). Suppose a parametric curve : $\mathcal{M} : u \in \mathbb{R} \rightarrow \mathbb{R}^2$.

$$\mathbf{X}(u, v) = \mathcal{M}(u) + v\overrightarrow{\mathbf{N}}(u) \tag{2.16}$$

Thus, the computation of the virtual image is more natural and direct with a parametric model $\mathcal{M}$ but can be applied to any type of model. The cost function related to this virtual image for each organ can be computed with:

$$E_{\text{image}}\left([\mathbf{P}_0, \mathbf{P}_1, \cdots \mathbf{P}_l]\right) = \int_{\mathbf{X} \in \Omega(\text{Band})} \left[I_r(\mathbf{X}) - I_v(\mathbf{X})\right]^2 d\Omega \tag{2.17}$$

Thanks to the virtual image, our method is exempt from image pre-processing and based merely on reliable original data (no need of pre-processing the images). The method requires less computation, and in a mathematical point of view, the virtual image can be considered as a smoothing of gradient field that avoids local optimum in this non-convex problem.

To avoid the inter-penetration of the analytical functions defining the contours of organs during deformable registration, we introduce a collision term to penalize the movement of DOFs (control points). The second energy term is computed by using signed distance maps $\mathcal{D} : \mathbf{X} \in \mathbb{R}^2 \rightarrow \mathcal{D}(\mathbf{X}) \in \mathbb{R}$. Each contour retains its own distance map describing how far a position in the image domain is from the contour: $\mathcal{D}_{bl}$ for the bladder, $\mathcal{D}_{va}$ for the vagina and $\mathcal{D}_{re}$ for the rectum. The collision energy term is defined by a quadratic function with regard to the distance $D, \mathcal{F} : D \in \mathbb{R} \rightarrow \mathbb{R}^{+}$:

$$\begin{aligned} E_{Bl} &= \int_{\mathbf{X} \in \Omega_{Bl}(\text{Band})} \mathcal{F}\left(\mathcal{D}_{va}(\mathbf{X})\right) d\Omega_{Bl} \\ E_{Va} &= \int_{\mathbf{X} \in \Omega_{Va}(\text{Band})} \left[\mathcal{F}\left(\mathcal{D}_{bl}(\mathbf{X})\right) + \mathcal{F}\left(\mathcal{D}_{re}(\mathbf{X})\right)\right] d\Omega_{Va} \\ E_{Re} &= \int_{\mathbf{X} \in \Omega_{Re}(\text{Band})} \mathcal{F}\left(\mathcal{D}_{va}(\mathbf{X})\right) d\Omega_{Re} \end{aligned} \tag{2.18}$$

where λ defines the width of the possible intersection zone associated with the contour, so that it penalizes the possible intersections when one contour happen to approach the narrow band of another closely. As shown in Figure 2.20, the vagina is at the middle of the three organs, so the bladder and the rectum are never in contact. We use the following equations to compute the collision term for each contour:

$$\begin{aligned} E_{Bl} &= \int_{\mathbf{X} \in \Omega_{B/(\text{ Band })}} \mathcal{F}\left(\mathcal{D}_{va}(\mathbf{X})\right) d\Omega_{Bl} \\ E_{Va} &= \int_{\mathbf{X} \in \Omega_{Va}(\text{ Band })} \left[\mathcal{F}\left(\mathcal{D}_{bl}(\mathbf{X})\right) + \mathcal{F}\left(\mathcal{D}_{re}(\mathbf{X})\right)\right] d\Omega_{Va} \\ E_{Re} &= \int_{\mathbf{X} \in \Omega_{Re}(\text{Band})} \mathcal{F}\left(\mathcal{D}_{va}(\mathbf{X})\right) d\Omega_{Re} \end{aligned} \tag{2.19}$$

As the virtual image, $\mathcal{F}$ is used as a level-set function for computing the energy associated distance map. The map for each organ is redefined once at each iteration. Thus, for example, the value of $\mathcal{F}\left(\mathcal{D}_{va}(\mathbf{X})\right)$ for a given position $\mathbf{X}$ is obtained directly by projecting $\mathbf{X}$ onto the map of the vagina. We do not recompute the distance $\mathcal{D}_{va}(\mathbf{X})$ for each discrete point at the same iteration. Finally, these two energy terms are summed to form a global energy term as the cost function.

$$E_{global} = E_{\text{image}} + \alpha E_{\text{collision}} \tag{2.20}$$

E_{image} is to be associated with each organ. $E_{\text{collision}}$ is to be replaced by E_{bl}, E_{va} and E_{re}, respectively. The coefficient α is chosen empirically during tests; the same value is used for the images of the same spatial resolution.

Optimization In our registration procedure, optimization is the step connecting the cost function (energy) and the model. It updates iteratively the DOFs of the model. For such a non-linear optimization problem, the algorithm is based on gradient. We opt for a gradient descent algorithm in this paper, which is suitable for optimizing the position and the number of the control points, and for controlling the convergence with regards to the adaptive refinement step. However, the Newton–Raphson method can also be computed similarly, The searched direction of the DOFs depends on the derivatives of the cost function. Let Ti be one of the DOFs in Equation 2.12, the derivative is computed as follows:

$$\frac{\partial E_{\text{image}}}{\partial T_i} = \int_{\mathbf{X}\in\Omega(\text{Band})} -2\left[I_r(\mathbf{X}) - I_v(\mathbf{X})\right] \cdot \underbrace{\frac{\partial I_v}{\partial \mathbf{X}}}_{A} \cdot \underbrace{\frac{\partial \mathbf{X}}{\partial T_i}}_{B} \, d\Omega \tag{2.21}$$

As mentioned in the B-spline Model section, our model is optimized via a multi-scale registration procedure. At the initialization step, the user defines a point the inside of each organ as the center of B-spline curve. We have tested a new initialization, while asking the user to put the point approximatively at the zone where the portion of organ is larger. We have observed a better increase of the initial contours at the first steps. Concerning the number of the control points, thanks to the adaptive refinement that we consider as one of our major contributions, we think it may not have a real importance because the points are to be added and deleted automatically after. And we give 10 by default. Then, a circle-like B-spline with 10 control points is created for each organ, which is a basic and simple one-click initialization (see figure 2.21).

For the coarse registration, the parameters of affine transformation (Equation (3)) are optimised (search direction computed by Equation (13)). In Figure 7B, one can observe that after the affine transformation, the three circle-like shapes are transformed to ellipse-like ones, which give an approximate initialisation of the detection procedure. Following the first step, a finer registration is applied using deformations based on B-spline model. Thus, the positions of control points are DOFs to be updated to fit the organ contours by means of minimising a cost function:

$$\frac{\partial E_{\text{image}}}{\partial \mathbf{P}_i} = \int_{\mathbf{X}\in\Omega(\text{Band})} -2\left[I_r(\mathbf{X}) - I_v(\mathbf{X})\right] \cdot \underbrace{\frac{\partial I_v}{\partial \mathbf{X}}}_{A} \cdot \underbrace{\frac{\partial \mathbf{X}}{\partial \mathbf{P}_i}}_{B} \, d\Omega \tag{2.22}$$

The partial derivative A is the gradient of virtual image that can be computed by the derivative of the level-set function. The partial derivative B is the mapping function, which means B-spline interpolation function in this case. Thanks to the power of analytical formulation, the required derivatives are simple to compute. In addition, the chain rule of derivation shows the independence of geometric model and the image energy computed by the difference between the virtual image and the real one. Hence, one can use the virtual image approach with different geometric representations (or mapping function). The collision term $E_{\text{collision}}$ can be computed in a similar way. Because of the nature of gradient descent, after certain iterations,

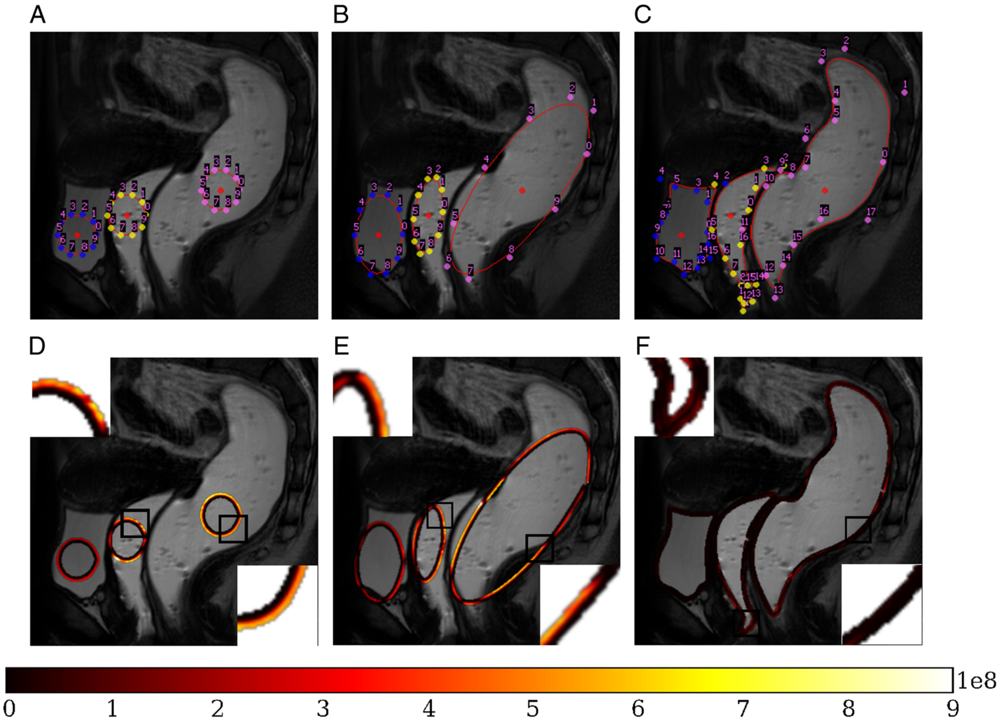

Fig. 2.21: Contour detection with the cost functions. (A) Three small circles initialised by user with 10 control points for each. (B) Positions after an affine transformation. (C) Final contours with optimal number of control points. (D–F) Illustration of the cost function metrics E_{image} along the organ contours: $[I_r(u,v) - I_V(u,v)]^2$, with u evolves in the tangent direction of the contour and v in the direction perpendicular to the contour.

it shows a phenomenon of local minimum (the energy does not evolve). We use this phenomenon as the criterion for adding control points. A test of local minimum is performed automatically for every 10 iterations. Let E_{max} be the maximum value of the cost function during this 10 iterations, E_{min} the minimum value and E_0 the initial value $\frac{\|E_{max}-E_{\text{min}}\|}{E_0} < \varepsilon$. If the criterion is satisfied, the optimization is supposed to reach a local minimum (low variation of the cost function); then, the curve is refined where the cost function needs to be reduced. The refinement step is treated automatically by inserting and removing control points based on the evaluation of cost function along the contour. Once the curve is refined, the optimization passes the local stability and continues to find the best correlation. This test and the adaptive refinement are performed repeatedly until the refinement can no more affect the cost function. By integrating insertion and removal of control points, our method can refine adaptively the geometric model with respect to images. The major advantage is that our B-splines fit properly the forms even in case of local aberrant curvature changes and avoid useless control points for description of the curve. This feature makes our method capable of a balance between model complexity and simplicity of optimization. The insert of control points does not change the B-spline curve by using its geometric algorithms. Every time when the gradient descent algorithm reaches its local minimum detected by a threshold of variation of the cost function, we refine the curve by subdividing the knot interval where there appears the maximum value of cost function. On the other hand, when two control points approach each other within a distance threshold, one is deleted for eliminating inter-cross of curve. In Figure 2.21F, we illustrate the distribution of cost function along the contour at the three stages (initialization, after affine transformation and the final position). The values of the cost function decrease significantly during the optimization. Moreover, the distance from a position on the contour to the organ border can be indicated by evaluating the metric map along contour. By zooming inside the contour, higher values occur when it is far from the real image border, which can be the indication for refinement.

2.3.2 Results

We validate our method of segmentation on a database of 19 patient images. The types of these patients include the witness, the prolapse and the endometriosis (a pathology of the pelvic system related to the hypo-mobility). Each patient data set consisted of a T2-weighted MRI of the pelvic system. We used for this 2D segmentation test the image in the mid-line sagittal plane of each patient, which is representative and useful for further study of the pelvic mobility. By the end of each optimization process, a medical doctor manually corrected the shape of organs by modifying the positions of control points so that the final curves and the contours of organs, to the medical doctor's opinion, were well fitted. These final curves were used as the reference in our validation. In Figure 2.22, we illustrated the detection and the validation for each type. Then, numerically, we compared the curves before manual corrections with the final ones by evaluating error with several metrics: Dice coefficient, Hausdorff distance and average curve distance (ACD). Figure 2.23 shows the computation of these metrics by using the right contour (green) and an arbitrary contour (red, and manually created to show a larger error). In this paper, suppose that F is the set of edge points on the semi-automatically segmented region and G is one of the manually segmented region. The ACD values represent the average (L1-norm) of distances in millimeter between the edge points on the manually segmented organ and the automatically detected organ. The minimum distance for the ith point in F to the set G is d_i^{FG}, thus the ACD values can be computed as in Equation 2.23. The number N_F and N_G were chosen to make sure that approximately an edge point was used by pixel.

$$\begin{aligned} &ACD^{FG} = \tfrac{1}{N_F} \textstyle\sum_{i=1}^{N_F} d_i^{FG} \\ &ACD^{GF} = \tfrac{1}{N_G} \textstyle\sum_{i=1}^{N_G} d_i^{GF} \\ &ACD = \left(ACD^{FG} + ACD^{GF}\right)/2 \end{aligned} \tag{2.23}$$

In addition, for the Dice coefficient values, a higher Dice value assesses a better segmentation quality. On the 19 patients data, we got a similarity of over 90% for bladder and 80–90% for vagina and rectum especially because the ends of these two organs are difficult to define. In Figure 2.24, we illustrated some exceptions of the detection due to the unwanted effect presented in the images. Generally, the bladder is well highlighted under acquisition, while as the injected gel can exit the cavity with the patient is pushing, blurs and incertitude will occur in the image for the vagina and the rectum (Figure 2.24B). Because of the complexity of the shape, crease will occur in the 2D plane of the rectum (Figure 2.24A) and intrinsic material generates spots in the rectum in the image (Figure 2.24C). All these unwanted effects would make the algorithm limited in certain cases. In these cases, the algorithm detected contours. However, the contours are not the anatomical contours of the organs. The quantitative results of our tests are shown in Table ??.

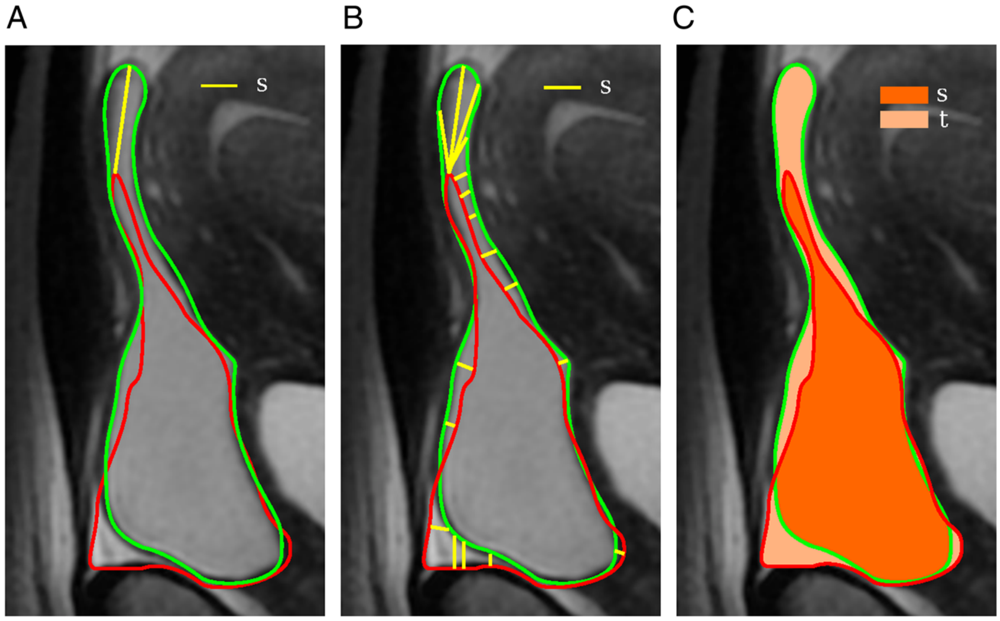

Fig. 2.22: Measurement of the detection error between a correct contour (green) and an arbitrary contour (red): (A) Hausdorff distance = length of s. (B) Average curve distance = average length of s. (C) Dice coefficient $= s/(s+t)$.

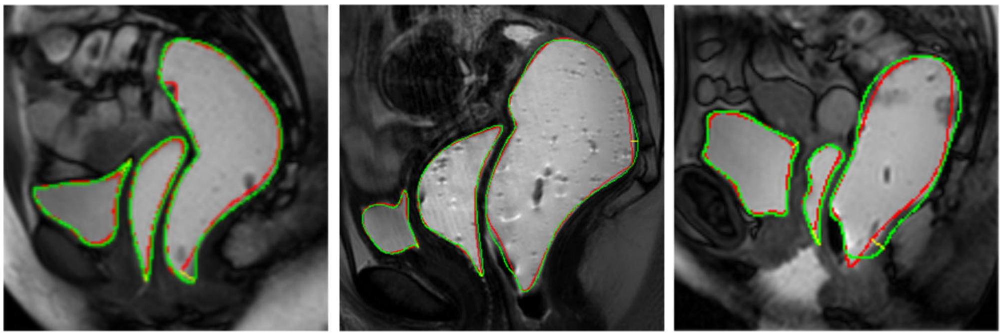

Fig. 2.23: Illustration of results: green curve shows the manually segmented organ as the reference, red curve shows the result of semi-automatic algorithm and yellow line shows the Hausdorff distance. (A) Witness patient (1.17 mm/pixel). (B) Patient with endometriosis (0.49 mm/pixel). (C) Patient with prolapse (1.17 mm/pixel).

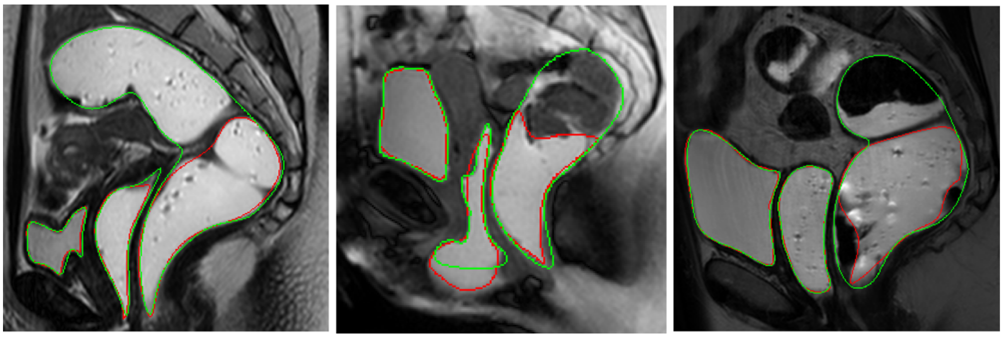

Fig. 2.24: Different exceptions of detection caused by unwanted effect in images:(A) As rectum may be folded somewhere,wrinkles appear in image as black rings. (B) The injected gel and intrinsic material may produce blur parts in image. (C) Intrinsic material show spots in rectum.

Patient (19)		Endometriosis (8)	Prolapse (8)	Witness (3)	Average
Bladder	DC(%)	91.4	89.5	95.1	91.2
	HD(mm)	9.46	10.87	5.74	9.46
	ACD(mm)	1.35	2.23	0.90	1.65
Vagina	DC(%)	93.0	83.8	84.8	89.4
	HD(mm)	6.14	11.34	3.02	7.84
	ACD(mm)	0.89	1.80	0.67	1.24
Rectum	DC(%)	83.4	82.2	78.6	82.2
	HD(mm)	31.12	25.91	33.59	29.32
	ACD(mm)	5.04	4.77	5.66	5.02

Tab. 2.6: Summary table for results of the error measures between manual and automatic segmentation – the three sub-tables present results of each organ in different pathological cases.

2.3.3 Application: Pelvic System Mobility

Female pelvic disorders have a large social impact, the diagnosis of which relies on a key indication: pelvic mobility. The normal mobility is present in a healthy patient, meanwhile the hyper-mobility can be a sign of prolapse and the hypo-mobility for endometriosis. The evaluation of pelvic mobility is based on medical images. However, the latter does not provide directly precise values of these indicators. Moreover, suspension devices play an important role in pelvic organ function, but can neither be observed on medical images. Our objective is to propose an image-based analysis tool for the quantitative evaluation of pelvic mobility and the shear strain which has an impact on suspension devices. Hence using the approach described in the previous section we have developed a tool based on an efficient and semi-automatic motion tracking of multiple pelvic organs: the bladder, vagina and rectum presented in dynamic magnetic resonance imaging sequences. The computed displacement and shear strain field provide important information on the quality of suspension devices between organs, (i.e. on the condition of fascia tissues), to the opinions of medical doctors, which are interesting for a fine diagnosis in the clinical context, for example the early diagnosis of pelvic organ prolapse and the localization of possible lesion zones before surgery.

Tracking Algorithm

Overview A Lagrangian description is used to define the motions of the principal pelvic organs under deformation. Following this description in continuum mechanics, for any particle of the object, the change of its position over the time is defined by a function of transformation, from its initial configuration (or reference) to the current configuration. In other words, at any instant, the computation of physical quantities such as the displacement is always associated with the same particle (or *material point*), compared to its initial configuration.

To achieve the objective of motion tracking, firstly, we initialize the B-spline geometric model at instant t_0 (the first image of the sequence) as the reference configuration. Secondly, the model is updated for fitting each following image in the sequence to form the configuration at instant t. The process is recursive: the model of instant t is deformed to fit the next image at instant $t+1$, and it is also based on an energy minimization formulation. Once the we obtain the models correspondent to all the instants, a displacement and shear field can be computed by using the analytical formulation of the models and following the Lagrangian description.

Meanwhile, we need to deal with the major concern about the plausibility of computed displacements. Normally, the description of the movement of material points remains in a fix landmark related to the initial configuration. So far the computation is based on the parametric coordinates, depending on the control points and their relative shift. But since these control points are not located on contours and they can freely drift along the contour. Thus the landmark for calculating the position of material points is mobile.

The idea is to fix some points on corners and to restrict the movement to perpendicular to the contour. For this purpose, the B-spline model is divided into piecewise cubic Bézier curves joined end to end. The ending point of one Bézier curve is attached with the starting point of another to form a connection point which is considered as a material point and where the curvature is higher than other-where. Here impose we an anatomical assumption that the salient points on the organ surface (or corners on the contour in a 2D plan) represent material points, which is based on the observation of medical images. Such material points, denoted as *features* in the remainder of this paper, are firstly tracked by the optical flow algorithm [LK+81], which consist in the beginning configuration for each recursive process of deformable registration from t to $t+1$.

Features definition We apply a new adjusted model (composite Bézier curve) and the connection points of Bézier curves become the material points. At the initial step, the choice of these features is performed automatically based on detection of the higher curvatures. Suppose that the contour of an organ in the initial configuration (instant t_0) is defined by a parametric B-spline curve $\mathcal{B}^0(u) = \sum_{i=0}^{n-1} \mathcal{N}_{i,3}(u)\mathbf{p}_i$. The curvature is related to the first and second derivative of the parametric function, which can be calculated by using the standard parametric coordinates as follows:

$$\kappa(u) = \frac{\left\| \mathcal{B}^{0\prime}(u) \times \mathcal{B}^{0\prime\prime}(u) \right\|}{\left\| \mathcal{B}^{0\prime}(u) \right\|^3} \tag{2.24}$$

where $\mathcal{B}^{0\prime}(u) = \frac{\mathrm{d}\mathcal{B}^0}{\mathrm{d}u}(u)$, $\mathcal{B}^{0\prime\prime}(u) = \frac{\mathrm{d}^2\mathcal{B}^0}{\mathrm{d}u^2}(u)$. Hence, the curvilinear curvature can be computed directly based on the initial B-spline model. In an automatic way, the algorithm enables to select a number of features where the curvature is higher by using the following criteria:

- `MaxNbFeatures` and `MinNbFeatures` maximal and minimal number of features to be selected;

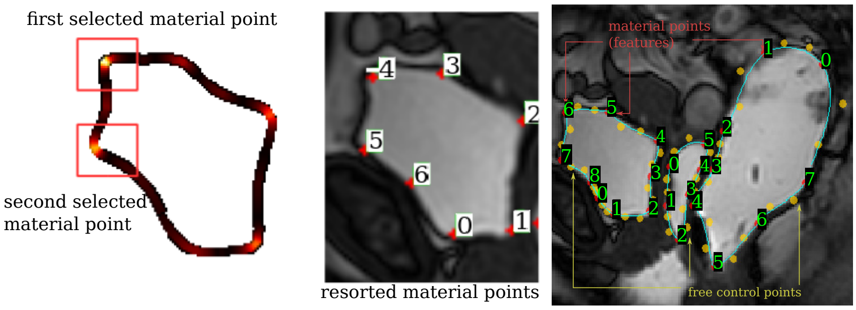

Fig. 2.25: (left-middle) Choice of the features along the B-spline contour. (right) Adjusted model at instant t_0, The figure is generated by our application.

- `MinDetectRadius` minimum distance between two adjacent features (used in order that the features are well spaced);
- `CurvThreshold` threshold of the curvature (used to avoid the features on flat segments).

Figure 2.25 (left, middle) shows the selected features with a curvature map bounding the contour. Meanwhile, the features are resorted with respect to the parametrization of the B-spline. Let $[\mathbf{pf}_0, \mathbf{pf}_1, \cdots, \mathbf{pf}_1]$ be the selected feature points, where $\mathbf{pf}_i = \mathcal{B}^0\left(u_{k_i}\right)$. $l+1$ piecewise Bézier curves can be created and joined at these points, who represent the same geometry as the initial B-spline and constitute the adjusted model. As defined in many standard texts, the Bézier curve is a special case of the B-spline who has four control points. In this case, for each piecewise Bézier curve, the two extremities are fixed by two adjacent features. Let us take the first Bézier segment between $\mathbf{pf}_0$ and $\mathbf{pf}_1$ as an example. This curve, denoted S_0, is defined by the Bernstein polynomial $\mathcal{M}_{i,p} : u \in [0,1] \to [0,1]$ as:

$$\begin{aligned} \mathcal{M}_{i,p}(u) &= \tfrac{p!}{i!(p-i)!} u^i (1-u)^{p-i} \\ \mathcal{S}_0(u) &= \textstyle\sum_{i=0}^{3} \mathcal{M}_{i,3}(u) \mathbf{p}_i \end{aligned} \tag{2.25}$$

where $p_0 = \mathbf{pf}_0$ and $p_3 = \mathbf{pf}_1$. Then the two free control points p_1 and p_2 are determined such that each Bézier curve fits the original B-spline contour on the interval $[u_{k_0}, u_{k_1}]$. The curve fitting method is well known as a standard approach by solving a system of linear equations. Figure 2.25 (right) shows the adjusted Bézier model as the initial configuration, created from the original B-spline model.

Features Tracking The approach of optical flow proposed by Lucas *et al.* [LK+81] can be well adapted into our needs. The method is based on the assumption of the constant pixel intensities and their low local variation. Because of the local

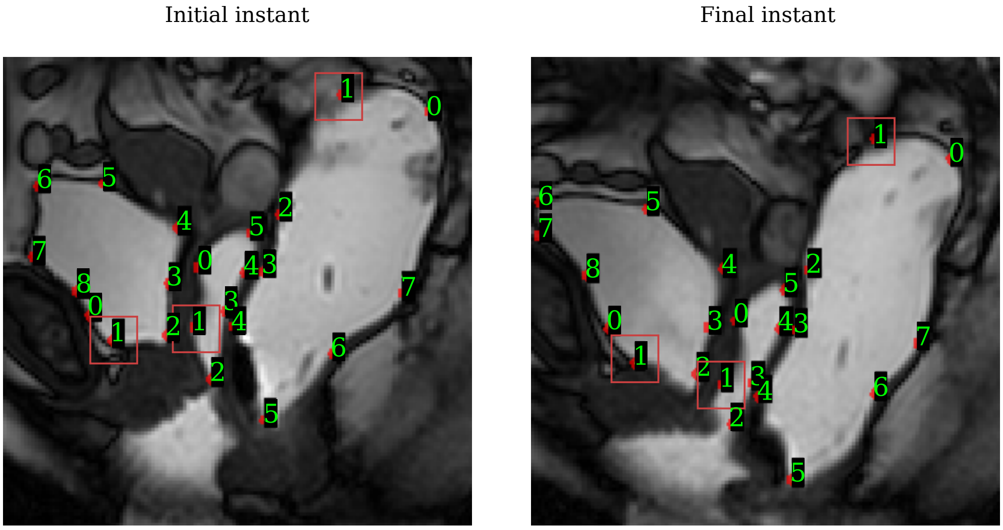

Fig. 2.26: Tracking of the features using the optical flow method: window grid size = 30 × 30 pixel.

evaluation, the method would fail if the deformation between images was large or the intensity in a region was uniform. However, in our case, the features to be tracked are located on the edge of organs where the variation of pixel intensities is large. Moreover, with the acquisition frequency of about one image per second, the deformation between two images (instant t and $t+1$) is relatively small. All these aspects permit a good performance of the optical flow tracking. In a practical view, it is necessary to choose the appropriate window grid size for the computation which respects the propriety of locality and where the image pattern is enough representative to be tracked. Generally, the choice of size depends on the image, we have adjusted this parameter empirically during tests (see Figure 2.26 for illustration of results). Once the tracking of features is completed using the optical flow, the transformation of each feature is to be applied over its two adjacent free control points to form the intermediate model at instant t^* (between t and $t+1$). Let always $\mathcal{S}_0$ be the first Bézier curve with four control points $[\mathbf{p}_0 = \mathbf{pf}_0, \mathbf{p}_1, \mathbf{p}_2, \mathbf{p}_3 = \mathbf{pf}_1]$. After applying the transformation, we obtain the following formula:

$$\begin{aligned} \mathcal{S}_0^*(u) = {} & \mathcal{M}_{0,3}(u) T_0\left(\mathbf{p}_0\right) + \mathcal{M}_{1,3}(u) T_0\left(\mathbf{p}_1\right) \\ & + \mathcal{M}_{2,3}(u) T_1\left(\mathbf{p}_2\right) + \mathcal{M}_{3,3}(u) T_1\left(\mathbf{p}_3\right) \end{aligned} \tag{2.26}$$

where $T_0\left(\mathbf{pf}_0\right) = \mathbf{pf}_{0^*}^*$ and $T_1\left(\mathbf{pf}_1\right) = \mathbf{pf}_1^*$ determined by the optical flow method (see Figure 2.27 for illustrations).

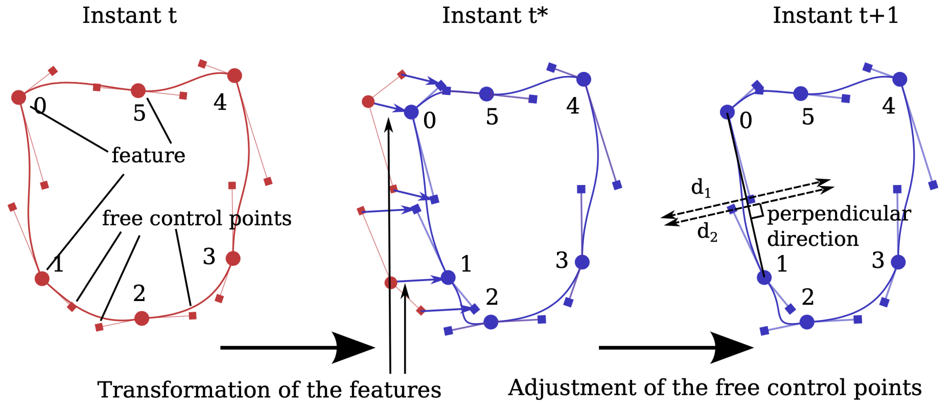

Fig. 2.27: Deformation of the model from instant t to $t+1$: firstly, the features are deformed using optical flow tracking method, for example the transformations of point 0 and 1 are computed by the optical flow equation. Then, the same transformations are applied on their neighboring free control points to form the intermediate model (instant t^*). Finally, the free control points (for example the ones situated between 0 et 1) are adjusted in the direction perpendicular to the segment using virtual image correlation, and produce the model at instant $t + 1$.

Optimization The last step consists in adjusting the free control points associated with each Bézier curve so that the model fits perfectly the organ in images. In order to minimize the drifting along the contour, the displacement (transformation) of these points is restricted to the direction perpendicular to the segment linking two adjacent features. And the magnitude of the displacement is also limited to be small because physically no new salient points will be produced during the deformation. Moreover, after the step of transformation based on the optical flow, the intermediate model has been already close to the deformed organ in the image. However, the adjustment allows a finer fit between the model and the image at instant $t + 1$. Following the same principle as the B-spline based detection, the adjustment of positions is carried out by minimizing the difference between the virtual image and the real one.

Displacements and Shears Our approach relies on a Lagrangian description which enables to compute continuous displacement field with our analytical geometric models. Following this description, the displacement field of each organ must be evaluated separately and each organ must have a reference configuration. This reference corresponds to the shape of the organ wall found at instant t_0 (on the first image, detected by our registration method). However, practically a given number of discrete points are sampled in the zone of interests in the initial configuration, and the analysis of mobility will rely on this discrete domain. The computation

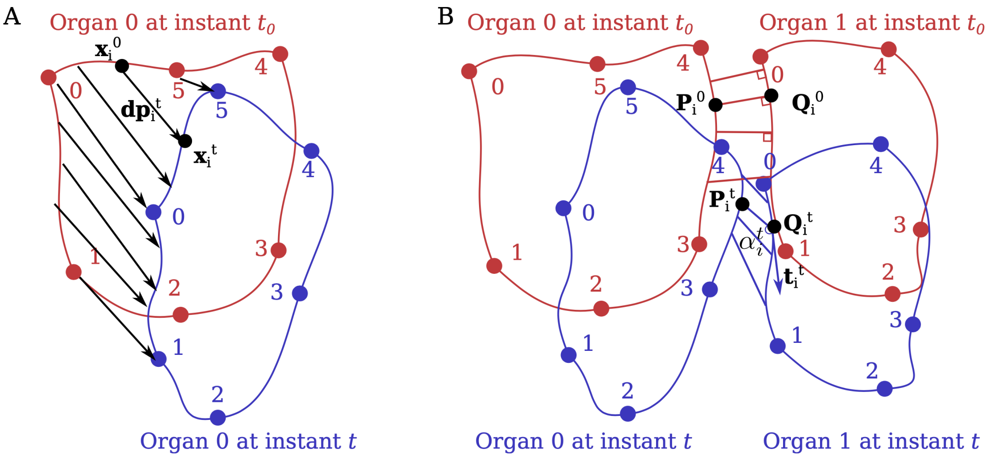

Fig. 2.28: Computation of the displacements (A) and shears (B), between instant t_0 and t.

of displacements and shears is then based on the parametric coordinates of Bézier curve

After computing the displacements for each Bézier curve respectively, we obtain a set of vectors $\mathbf{dp}_i^t$ which defines the displacements field at instant t, and this computation is repeated for each instant (image) of the dynamic MRI sequence. Concerning the shear strain between organs, the middle organ (vagina) is chosen to be the reference organ. Analogous to the computation of displacements, at the initial configuration we generate several couples of discrete points from different organs based on the zone of interest defined by users. These couples of points are linked by segments perpendicular to the vaginal wall. For example, firstly a part of the bladder contour is selected manually as the zone of interests for computing the shear between the bladder and the vaginal. Then M discrete points $\{\mathbf{P}_i^0\}$ are sampled on this zone. Given that the shear deformation is initially null, these points are projected orthogonally onto the contour of vagina to obtain M points $\{\mathbf{Q}_i^0\}$ who form segments with $\{\mathbf{P}_i^0\}$. Then in the presence of shear motion, the segments that are mostly normal to the vaginal walls will deviate from this direction and illustrate the shear effect. We use the variation of angles between the segments as a metric for quantification of the shear strain between organs. The positions of $\mathbf{P}_i^t$ and $\mathbf{Q}_i^t$ can be calculated by their displacements $\mathbf{dp}^t$. Let $\overrightarrow{\mathbf{t}}_i^t$ be the tangent vector of vagina at the point $\mathbf{Q}_i^t$ at instant t. The shear strain at this position is given by:

$$\begin{gathered}\alpha_i^t = \arccos\left(\frac{\overrightarrow{\mathbf{Q}_i^t\mathbf{P}_i^*}\cdot\overrightarrow{\mathbf{t}}_i^t}{\left\|\mathbf{Q}_i^t\mathbf{P}_i^\dagger\right\|\cdot\left\|\overrightarrow{\mathbf{t}}_i^t\right\|}\right)\\ \text{shear}_i^t = \tan\left(\tfrac{\pi}{2}-\alpha_i^t\right)\end{gathered} \tag{2.27}$$

Finally, after computing the shear strain for all the positions in the discrete domain, we obtain the set of the scalar values representing the shear strain field at instant t (see Figure 2.28 for illustration). Moreover, by combining the spatial distribution of shear strain over time (the dynamic MRI sequence), we will be able to complete a spatio-temporal representation of the shear between organs which is useful for the analysis of the impact of pathologies related to the weakness in the suspension devices.

Experimental Validation In this part, we would like to validate our approach with the material points (features) by the comparison of the two methods (the first one being using a classic B-spline). The idea is to apply two methods on the same data set for a quantitative comparison. The captured images consist of an orange, on which a rigid body displacement in the range of $0 - -90$ mm was applied. The image spatial resolution is 0.73 mm/pixel and the size is 149×261 pixels. The orange was rotated numerically by an angle of $0 - -20$ degrees in order to illustrate the sliding problem because generally the tracking algorithms are very sensible to the rotation. The computed angles of rotation are shown in Figure 2.29. Normally, the angles should be constant along the contour and equal to the imposed values. Nevertheless, it can be observed that the B-spline method is really rotational invariant. Especially, the rotation is not captured at all on the flat portion of the contour. The Bézier method compute better the rotation despite of few slight drifting (sliding effect) also on the flat portion, due to the limitations of the optical flow. As consequence, the values calculated by the Bézier method are much closer to the imposed ones. In order to highlight the difference, we show a more quantitative evaluation in Figure 2.30. The mean angles of rotation computed by the Bézier method remain proportional to the imposed ones. And their standard deviations are less than 1 degree. On the contrary, the result given by B-spline method deviates a lot from the theoretical result.

For the second step, we also compared these two methods for a real case in the context of normal mobility. The objective is to illustrate the drifting effect and then the uncertainty of the computed displacement and shear strain. The test was run on a dynamic MR sequence of a healthy witness which contains 35 images. The spatial resolution is 1.17 mm/pixel and the image size is 256 × 256 pixels. The visual comparison of the results given by two methods is shown in Figure 2.31. The displacements and shear at the middle of straining (the 20th image in the sequence) are used to highlight the difference and the drifting effect. Concerning the result given by the B-spline method, some displacements extremely towards the end of vagina are not reasonable. From the point of view of the physio-anatomy, there exits

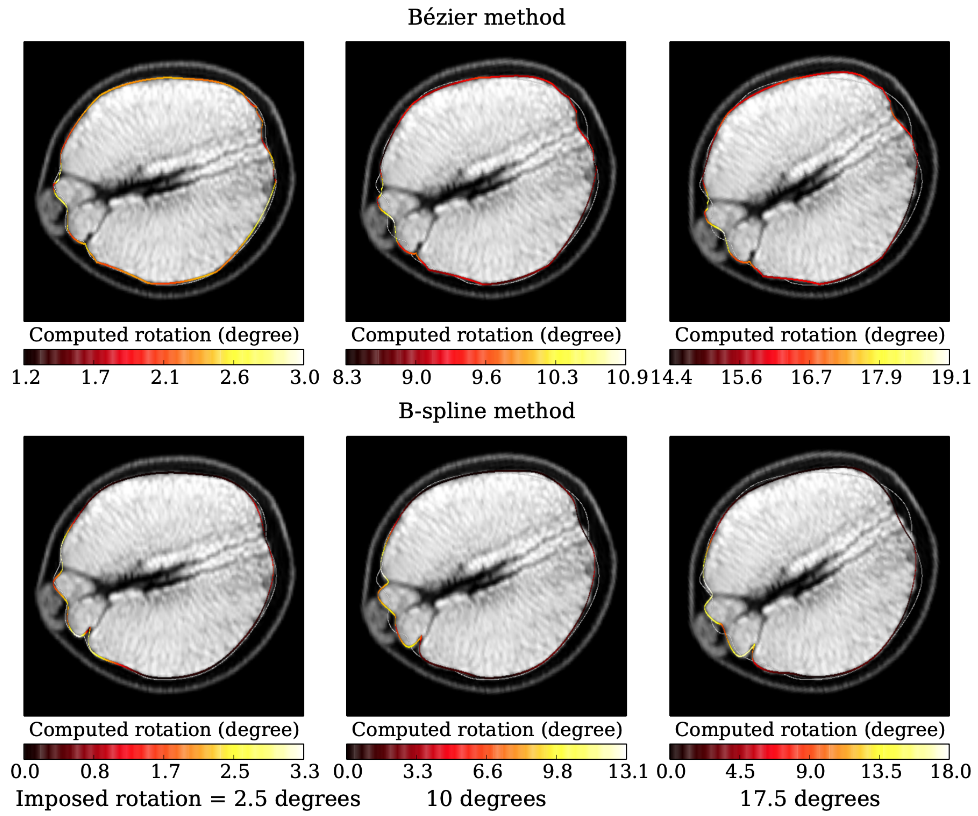

Fig. 2.29: Comparison of the angles of rotation computed by two methods: the results given by Bézier method are shown on the top and the ones given by B-spline method are on the bottom. The white contour is the initial one. The imposed rotations are 2.5, 10.0 and 17.5 degrees. The color map illustrate the variation along the contour in two cases.

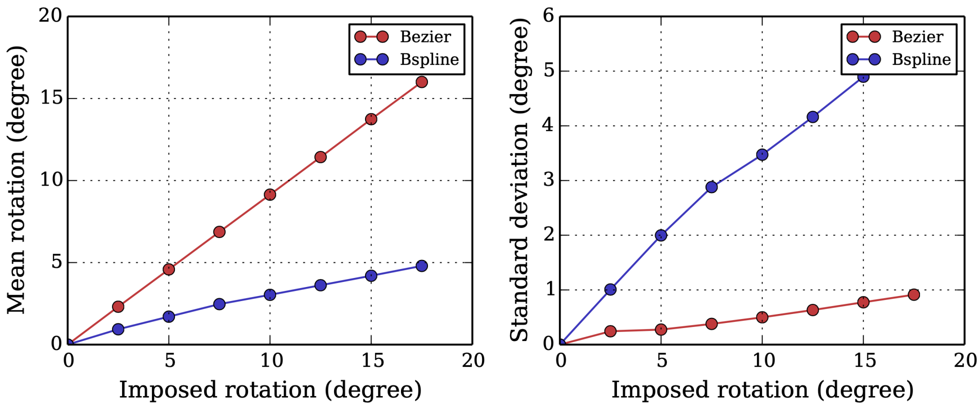

Fig. 2.30: Comparison of the angles of rotation computed by two methods: the results given by Bézier method are shown on the top and the ones given by B-spline method are on the bottom. The white contour is the initial one. The imposed rotations are 2.5, 10.0 and 17.5 degrees. The color map illustrate the variation along the contour in two cases.

some structures such as the fascias in the zone between bladder and vagina. The bladder, vagina and fascias adhere to each other. Such material is not supposed to stretch considerably without constraint even during the deformation, especially in the normal mobility context. So that the organ walls should neither move freely. Hence the abnormal discontinuity of the displacements on the anterior vaginal wall seems unphysical. The same observation can be found on the posterior vaginal wall. The quantitative comparison is shown in Figure 2.32 As proved in [Lec+15], the zone around the pubis and rectosacral attachment is the low mobility area. From the point of view of anatomy, the bladder and the rectum are attached to these bones during the deformation over time. The two methods give similar results. However, with the B-spline method, we predefined a fix point for each organ as the beginning and ending point (the same point) of the B-spline to position the initial contours. Hence it is normal for the B-spline method to find these low mobility areas. On the anterior and posterior vaginal wall (zone between the vagina and the rectum) and the lower part of the rectum, high mobility can be observed, where the displacements given by the Bézier method attain a magnitude of around 22 mm. Compared to the results in [Lec+15], the displacements are still a bit larger on the anterior vaginal wall. However, through all these comparisons between the results given by the B-spline method, Bézier method and [Lec+15], we are biased in favor of the Bézier method which is more physical.

We performed the same Bézier registration method on a dynamic MR sequence of a patient with prolapse. Because of large displacements in the context of hypermobility, the algorithm had some limitations especially when the uterus descended

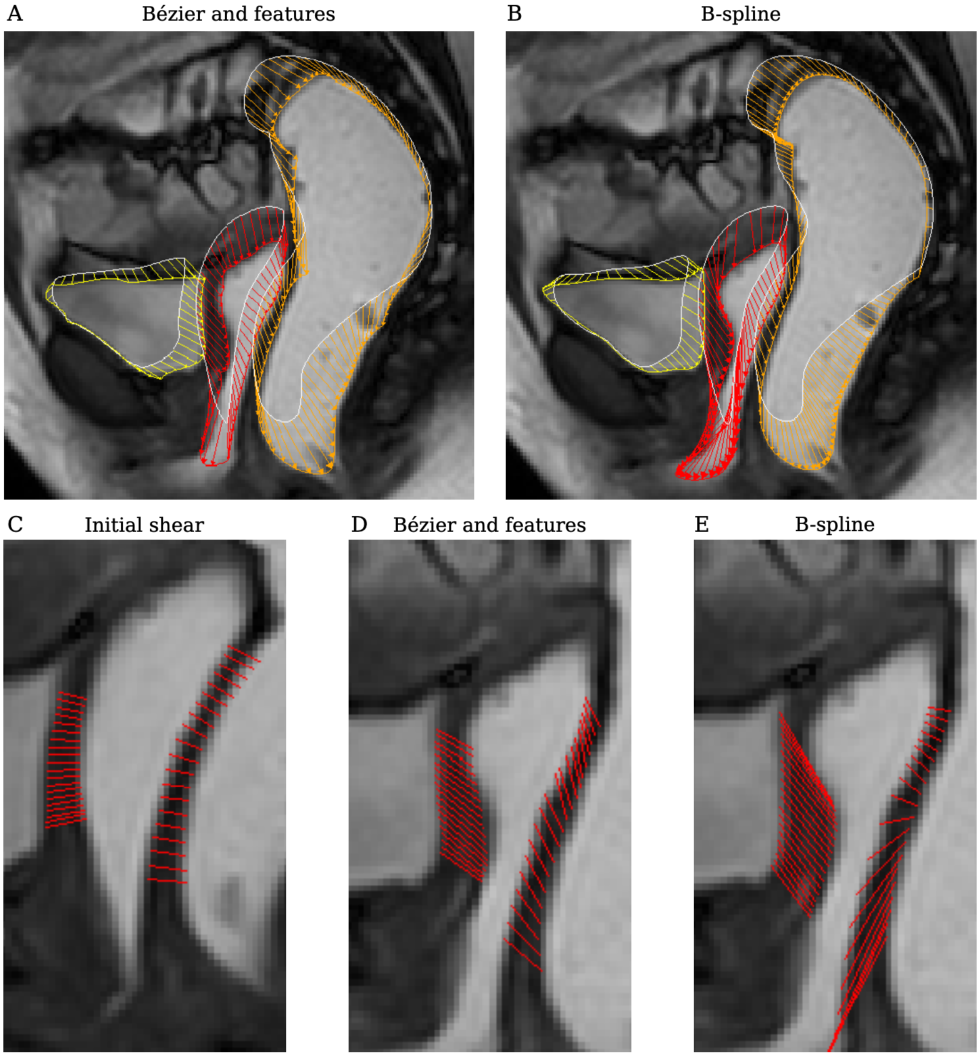

Fig. 2.31: Illustration of visual comparison between two method. On the top: displacements at the middle of straining computed by (A) Bézier method and (B) B-spline method. The white contours are the initial ones. On the bottom: (C) initial position of segments illustrating the absence of shear, and deviation of the segments at the middle of straining computed by (D) Bézier method and (E) B-spline method.

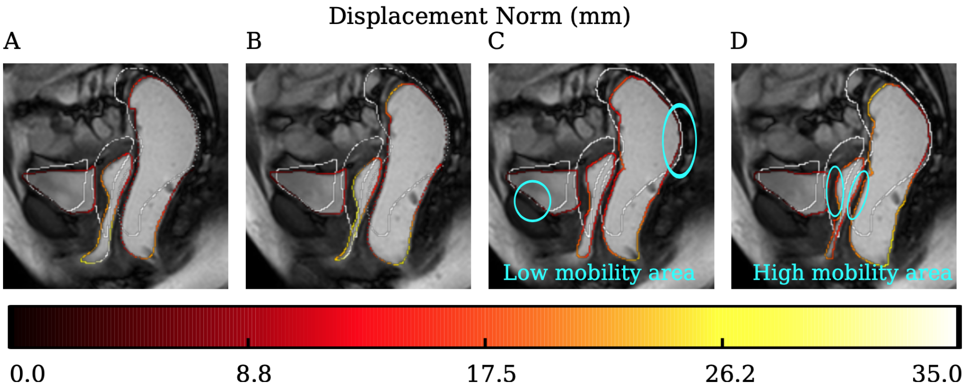

Fig. 2.32: Quantitative comparison of the displacements computed by two methods: (A,B) Displacement computed by B-spline method at the middle and end of straining, (C,D) Displacement computed by Bézier method at the middle and end of straining.

to the bottom. We would like also mention other limitations due to unwanted effect in the image: the injected gel can flow through the cavity while the patient is pushing and some intrinsic material of the organs can blur the image. All these effect can make the contours deviate from the truly anatomical contours. The restricted sequence from the beginning to the middle of straining contains 14 images, the spatial resolution of which is 1.15 mm/pixel and the size is 240 × 240 pixels. It can be observed that in the high mobility area (posterior vagina) the displacements (Figure 2.33B) are higher than in the normal case (Figure2.32C). The magnitude of displacement is close to 25 mm compared to 15 mm.

The same process was applied on a data set of patient with endometriosis. The sequence contains 32 images of 256 × 256 pixels and the spatial resolution is 1.17 mm/pixel. Due to the presence of wrinkles of the rectum in the image, only the inferior part of the rectum was taken into account for the analysis. In the high mobility area, the magnitude of displacement attained around 10 mm even at the end of straining, which corresponds to the context of hypo-mobility.

Conclusion In this section we present a deformable registration approach based on analytical models for multi-organ motion tracking in dynamic MRI sequence. The measured motion is then used for the evaluation of the mobility of pelvic system. The organ was defined by an analytical and parametric model, a composite Bézier curve joined at features (considered as material points). This definition can ensure better the plausibility of the measured motion. The model was then deformed to fit the organ in the dynamic image sequence by using the optical flow method and the virtual image correlation. Finally thanks to the analytical formulation, we computed

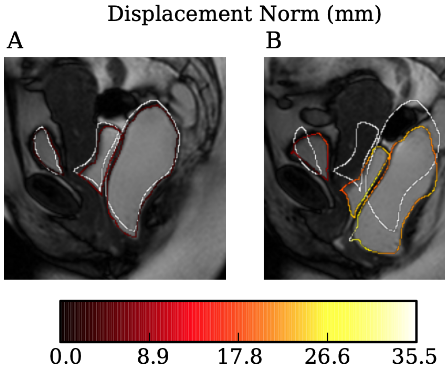

Fig. 2.33: Quantitative evaluation of the displacement field in the context of hyper-mobility: (A) Displacements at the beginning of straining and (B) at the middle of straining. The white contours are the initial ones.

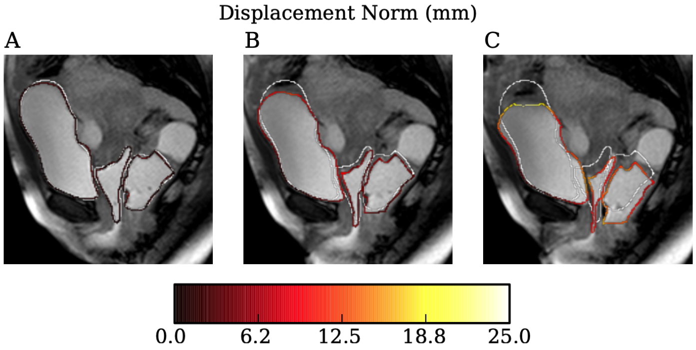

Fig. 2.34: Quantitative evaluation of the displacement field in the context of hypo-mobility: (A) Displacements at the beginning of straining, (B) at the middle of straining and (C) at the end of straining. The white contours are the initial ones.

the displacement field and shear strain of the moving organs. Hence, the developed numerical tool, linked with the B-spline based detection, can provide a quantitative evaluation of organ motion for patient-specific cases. The first perspective of this work is to assess and validate the computation of the shear strain deformations using more ground truth data. The quantification of the shear strain could be used to analyze the abnormal pelvic mobility and to localize the pathological areas related to the suspension devices which can not be observed on medical images. Such evaluation would provide objective diagnoses and help in early diagnosis of pelvic organ prolapse.

Medical and Robotic Applications

3

> *[...]but I tell you that all these things—yes, from that star that has just shone out in the sky to the solid ground beneath our feet—I say that all these are but dreams and shadows; the shadows that hide the real world from our eyes. There is a real world, but it is beyond this glamour and this vision, beyond these 'chases in Arras, dreams in a career,' beyond them all as beyond a veil.*
>
> — **Arthur Machen**
> The Great God Pan

3.1 Augmented Reality for Per-Operative Guidance

As exposed in the introduction, minimally invasive procedures are quite complex for a surgical standpoint mainly because the visual feedback is relatively incomplete or poor and due to the the loss of direct organs manipulation. With recent Augmented Reality techniques, those issues can be circumvented. Internal structures computed from pre-operative scans such as tumors and vessels can be superimposed onto the intra-operative images in order to guide the surgeons during the procedure. Our study is focused on minimally invasive hepatic surgery. In order to establish a full augmented reality system for *MIS* a number of difficult problems have to be solved [Nic+11]. The abdominal cavity undergoing laparoscopic surgery remains a very challenging environment for computer vision tasks. The surgical instruments interacting with the liver may cause large occlusions, the illumination variations caused by the endoscopic light and the liver bleeding or smokes due to electrocautery may disturb organ motion tracking and 3D structures recovery. Among the most difficult issues is the capacity to tackle, in real time, elastic deformations of the liver. The liver can undergo large deformations due to surgical tools interaction or due to respiratory motion and heart beating. Currently, most existing AR systems handle rigid motions of organs and only a very limited number of papers address the problem of elastic organs deformation.

Though the problem of elastic registration or tracking has been largely addressed in the medical community, elastic deformation in *AR* systems is only addressed, to our knowledge, in a very limited number of papers, and mainly applied to 3 organs: kidney, heart and liver. Kidneys do not actually undergo elastic deformations during surgery but rather move independently from their surrounding tissues. As such, related works resort to performing a rigid 3D-3D registration e.g. based on implanted markers [Teb+09] or an Iterative Closest Point (ICP) surface matching [Su+09]. Recently Puerto-Souza et al. [PM13] proposed a matching algorithm called Hierarchical Multi-Affine capable of long-term tracking for augmentation during partial nephrectomy. This approach estimates a set of affine transformations from clusters of features in order to relocate occluded or missing features for a coherent spatio-temporal mesh registration. Figl et al. [Fig+10] also express the non-rigid registration problem as a rigid registration between stereoscopic views and a 4D model of the heart built from 4D scan data, thus leveraging the cyclicity of the organ motion. A 4D scan of the heart is also used in [Pra+10], but is coupled with a biomechanical model to relate the surface motion to external forces. A local tuning of the deformation is therefore possible and the surface deformation is correctly propagated to in-depth invisible structures. No periodic or rigid pattern can be relied upon in the liver case. Unpredictable, possibly large, deformations can be observed. Furthermore, volume tracking is required since we are interested in in-depth augmentation whereas many approaches are dedicated to the tracking of surfaces. In a similar context, Kim et al. [Kim+12] propose a solution that is both applicable in a monoscopic setup and integrate a robust image feature reconstruction approach. But their method only retrieves surface deformation and cannot ensure an accurate augmentation of inner structures. Mechanical-based deformable models have proven to be relevant for volume deformation since they allow to define elastic properties of the shape and thus to infer in-depth structure motion [Spe+11; SLH10; Ser+03]. Registration is done either by solving mechanical equations given image constraints provided by reconstructed 3D points [Spe+11] or using the concept of active models where an energy is minimized which takes into account the internal behavior of the model -through the biomechanical constraints- and external image constraints that measure the adequacy between the model and the recovered 3D data [SLH10; Ser+03].

In this section, we present some results on Augmented Reality for Hepatic surgery accounting for large liver deformations. We present an approach that relies on the

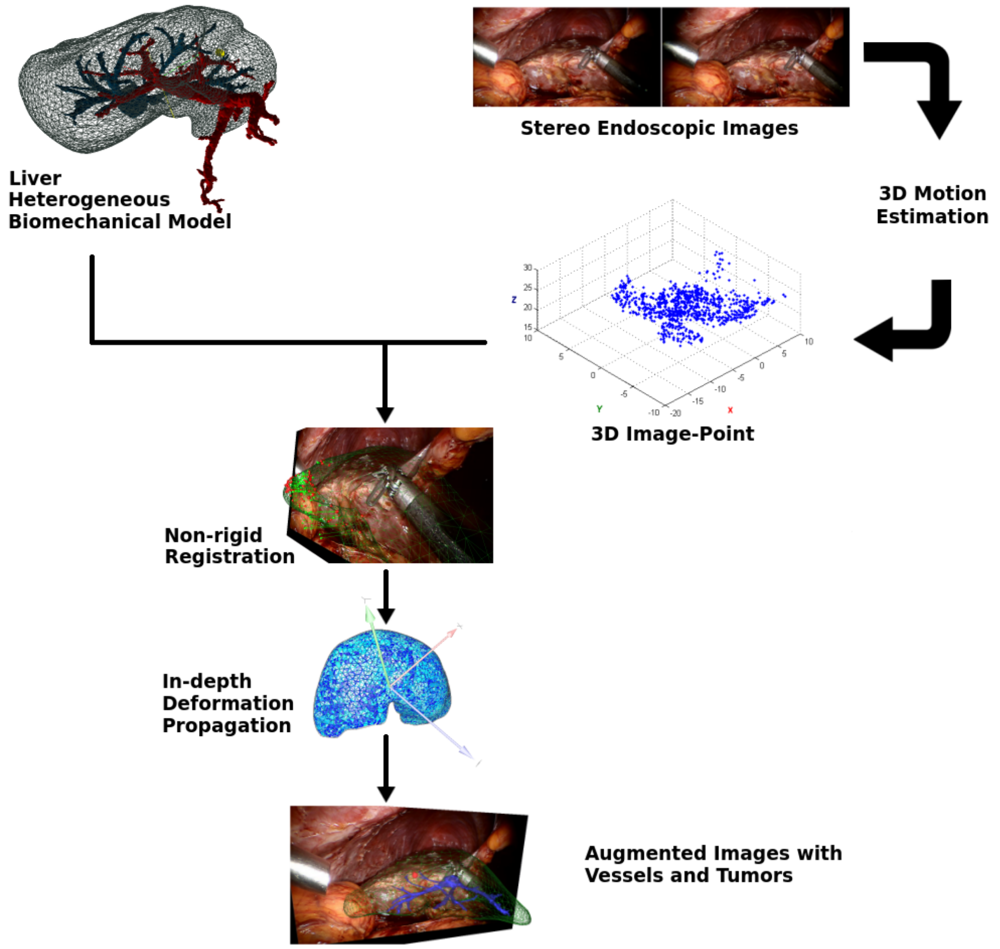

Fig. 3.1: Computational flow of the method: The biomechanical model guided by the 3D image-points recovered from intra-abdominal image pair permits to propagate partial tissue de- formations to vessels and tumors.

estimation of liver motion to drive a heterogeneous mechanical model capable of deforming the liver. The overview of the method is illustrated in figure 3.1.

3.1.1 Mechanical Modeling

Parenchyma Model

Most biomechanical studies concerning the constitutive models of the liver parenchyma (see [Ker06] for instance) report the non-linear and viscoelastic behavior of the organ tissue. Since in our case, we do not focus on the transient part of the deformation but rather the static equilibrium under some specific loading conditions, we do not take into account the viscous properties of the tissue. On the other hand, we aim at modeling large deformations correctly, since during the surgical interventions, important displacements of tissue (e.g. the liver lobes) occur due to the action of surgical tools. For this reason we have opted for finite element method based on co-rotational formulation presented in [Fel00] which allows for large displacements while relying on a linear expression of the stress-strain relationship. Different methods exist for computing the local rotation of each element; in this paper we use a geometric approach proposed in [NPF05] which respects the rotational invariance needed for correct rendering of large deformations (it also has been used in 1.5.1)

In the co-rotational approach, the stiffness matrix $\mathbf{K}$ depends on the deformation $\mathbf{u}$ and the equation relating the external forces to the displacements can be written as

$$\mathbf{f} = \mathbf{K}(\mathbf{u})\mathbf{u} \quad \text{with} \quad \mathbf{u} = \mathbf{x} - \mathbf{x}_0 \tag{3.1}$$

where $\mathbf{x}_0$ and $\mathbf{x}$ represent nodal positions in rest and actual positions, respectively, and $\mathbf{f}$ are the external forces.

Assuming that linear tetrahedral $P1$ elements are employed in the FE formulation of the parenchyma model and the mesh is composed of $N_{\mathbb{P}}$ nodes, the resulting system has $3N_{\mathbb{P}}$ degrees of freedom, i. e. $\mathbf{u}_{\mathbb{P}}$, $\mathbf{f}_{\mathbb{P}}$ are vectors of size $3N_{\mathbb{P}}$ whereas $\mathbf{K}_{\mathbb{P}}$ is a $3N_{\mathbb{P}} \times 3N_{\mathbb{P}}$ matrix, where the subscript $\mathbb{P}$ denotes the parenchyma.

It should be noted that our method is not limited to the co-rotational model, which can be replaced by hyperelastic formulation such as the technique based on *multiplicative Jacobian energy decomposition* presented in [Mar+10].

Vessel model

The vascular system is regarded as the main source of heterogeneity which has a global influence on the mechanical response of the vascularized tissue. The model employed here is based on work presented in [PDC12]. Besides describing the model in the actual scenario, additional details concerning the assembling of the composite system are given in the following text. Is should be emphasized that a potential viscoelastic response due to the liquid (i. e. blood) circulating in the vessels is not taken into account as only quasi-static scenario is assumed.

From the mechanical point of view, the vascular system is modeled with serially linked beam elements in a similar way as proposed previously in the manuscript (see 1.3) for simulating catheters and guide-wires. We introduce some modifications to the model to take into account the particular nature of vessels, in particular through specific cross section profiles and moments of inertia (see [Prz68] for details). The static formulation for the deformation of a beam is described by a system similar to Eq. 3.1 with constituents $\mathbf{u}_{\mathbb{V}}$, $\mathbf{f}_{\mathbb{V}}$ and $\mathbf{K}_{\mathbb{V}}$. However, as each node is equipped with 6 degrees of freedom due to the rotational components, the size of vectors $\mathbf{u}_{\mathbb{V}}$ and $\mathbf{f}_{\mathbb{V}}$ is $6N_{\mathbb{V}}$ and $\mathbf{K}_{\mathbb{V}}$ is a $6N_{\mathbb{V}} \times 6N_{\mathbb{V}}$ matrix where $N_{\mathbb{V}}$ is the size of beam mesh representing the geometry of vessels.

Mechanical coupling

Mapping of tumors and parenchyma The size of tumors being relatively small comparing with the whole parenchyma, we assume that its influence on the overall mechanical behaviour is negligible and therefore the coupling with parenchyma can be only geometric. However, a purely geometric mapping may deform the shape of the tumor which may cause erroneous measurements. For this reason the tumor is modeled as a solid object with a very stiff Young's Modulus. This modeling does not affect the performance of the simulation and permits a conservation of the shape of the tumor while allowing correct in-depth propagation of the deformation. With the same formulation as the parenchyma (co-rotational model), coupling between tumors and parenchyma is done using mapping mechanism provided by SOFA [Fau+12] which corresponds to the principle of virtual works used in solid mechanics.

Coupling between vessels and parenchyma In order to build the composite model of vascularized tissue, we adopt the method proposed in [PDC12]. Since no relative motion between the vessels and parenchyma is observed in reality, the mapping between the two components can be modeled as a constant coupling. In each step of the simulation, the actual displacements of the parenchyma nodes are mapped to the vessel nodes and reciprocally, the force contribution due to the deformation of the vessel is propagated to the parenchyma. The mapping of forces is based on a principle of virtual work. Additionally, the mechanical contribution of the vessels is added to the global system.

The complete mechanical system of the liver is then: a 3D co-rotational FEM mesh for the parenchyma and the tumors and beam model for the vasculature inside the parenchyma. These 3 models are coupled mechanically (see figure 3.2).

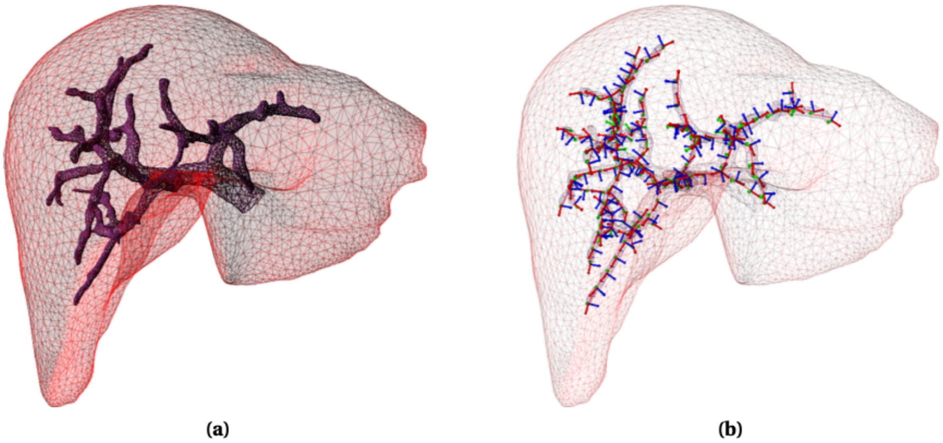

Fig. 3.2: 3D heterogeneous biomechanical model of the liver with : (a) heterogeneous liver including the vascular network in wire-frame, in (b) beams generated along the vessels.

3.1.2 Non-rigid Registration

Non-rigid registration consists of a 3D point-to-point registration that links the image-based 3D features representing the liver motion to the degrees of freedom of the liver physical model. Registration is done at each frame captured by the endoscopic camera in order to correctly pilot the mechanical model, and thus to estimate the correct position of the underlying tumors. An important key for an efficient registration is the initialization step as it will impact the estimated deformation of the parenchyma and the estimated location of tumors.

Initialization

Initialization refers to the step where the alignment of the 3D surface mesh on the laparoscopic image at $t = 0$. This step is critical and is known as an ill-posed problem where we aim at registering two sets of 3D points without knowing the matching between these two sets. In addition, since gas is insufflated (surgical step named as *pneumoperitoneum*) to increase the working space [Ban+12], the preoperative data may no longer correspond to the intra-operative image. Due to this complexity and despite the numerous AR techniques in surgery, very few works have investigated the initial alignment between laparoscopic images and the three-dimensional model. Some have investigated this issue but mostly relies on intra-operative data that are complex to acquire in a clinical routine: for instance [DBB08] use an ultrasound probe to ease the automatic registration process while [Okt+13] use intra-operative

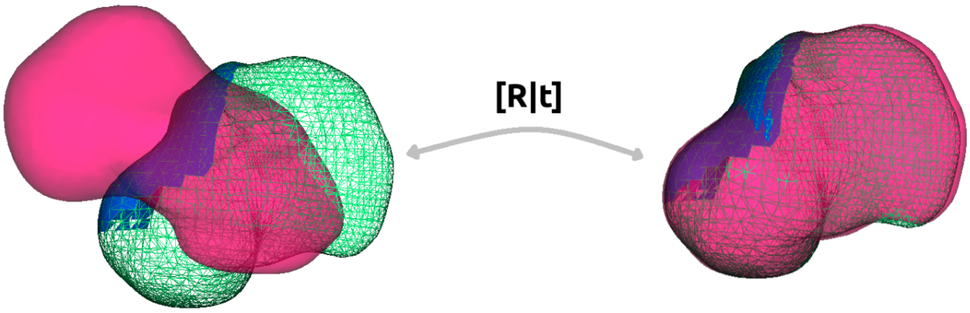

Fig. 3.3: Initial model alignment (simulated data): The mesh in purple represent the 3D model computed from CT scans in a different reference, the mesh in blue represents the MLS surface reconstructed from laparoscopic image pair. It represents around 30% of the whole liver that is represented in green.

CT scans. Currently, no technique is mature enough to permit an automatic initial alignment with conditions acceptable to clinical routine, and this issue remains a challenge to be solved by the scientific community. This is why, we rely on a manual initial alignment to reduce errors that may emanate from a bad initialization (see figure 3.3): 3D surface reconstruction is built on the first pair of laparoscopic images using the MLS surface approximation and the liver mesh is rigidly aligned using salient geometrical landmarks such as liver contours or surrounded ligaments which enables to provide the rigid transformation (rotation and translation) to align the two datasets. However, this rigid transformation is insufficient to correctly initialize the registration. Indeed, due to gas insufflation, pre-operative data (liver mesh computed for CT-scans) geometrically differs form intra-operative data. To solve this issue, we constrain the biomechanical model (including the vessels and the tumors) with external forces so that it better fits the visible liver surface recovered.

Runtime point correspondence

Tracking the liver tissue Tracking object of interest is the most important component within Augmented Reality applications. Several previous works have investigated the motion estimation of non-rigid objects in 3D such as [SF10; WLS12; Mor+09] but are not applicable in our clinical context because they either rely on additional data or make strong assumptions on the range of possible deformations.

The visual tracking we used follows the work by Elhawary and Popovic [EP11] who relies on the combination of Lucas-Kanade (LK) [LK+81] optical flow and SURF detector [Bay+08] for robotic-guided endoscopy. This study showed the robustness and accuracy of this combination and its usability for conventional laparoscopic surgery (see figure 3.4 for some experiments). However one major drawback of

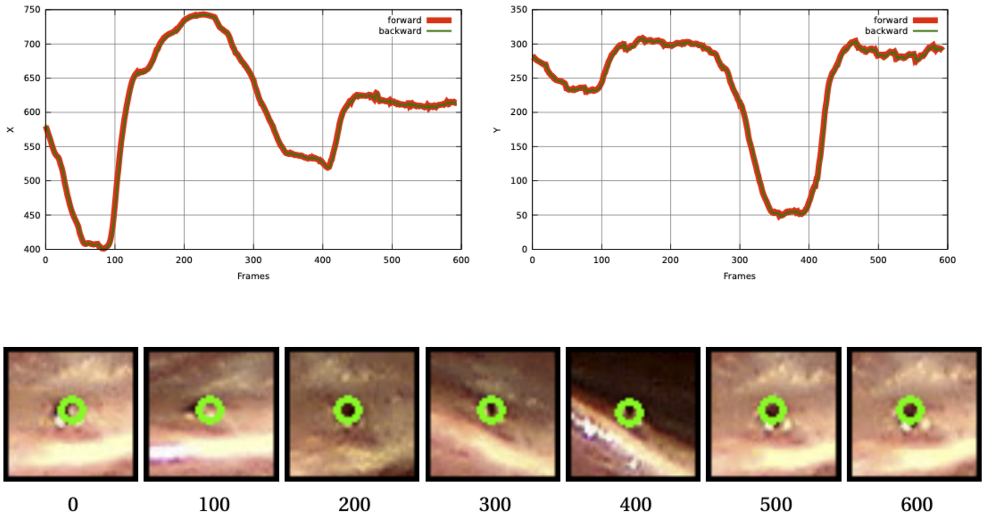

0 100 200 300 400 500 600

Fig. 3.4: A SURF feature being tracked over time (600 frames) using LK optical flow. (top) tracking performed in both a forward and a backward time direction. Graph shows X and Y coordinates as a function of time. (bottom) 50 × 50 pixel window centered around the feature location at every 100 frames.

this combination is the fact that features loss can happen with the optical flow, preventing to perform long-term tracking. In order to ensure a long term stability for the non-rigid registration, we add an additional layer to the direct tracking. This layer called Cluster-based Filter (CbF) allows to create a set of n 3D control points, denoted by a $3\text{Ö}n$ coordinate vector y that guides the biomechanical model. Instead of constraining the model directly with the extracted features, the CbF computes a displacement field for each control point based on the adjacent features (see figure 3.5). Its benefits are twofold: a) It ensures the minimization to remain stable since the number of control points (and the amount of external forces) is less subject to lost features. Moreover, it permits to avoid to over-constrain the corresponding tetrahedral element which can often tend towards instability. b) it allows to keep only the needed features. Indeed, we can here exploit the capability of the mechanical model to estimate deformations with a reduced number of external loads. The figure 3.6 illustrates the complete approach were a silicone cube is deformed.

Point correspondence The temporal non-rigid registration is a point-to-point registration where we need to map 2D image pixels onto the 3D surface mesh. This procedure is done using ray casting [Rot82] which is simple to implement and because it provides several benefits: a) it permits to directly correspond the set of points to the degrees of freedom of the mechanical model, b) only the 3D points

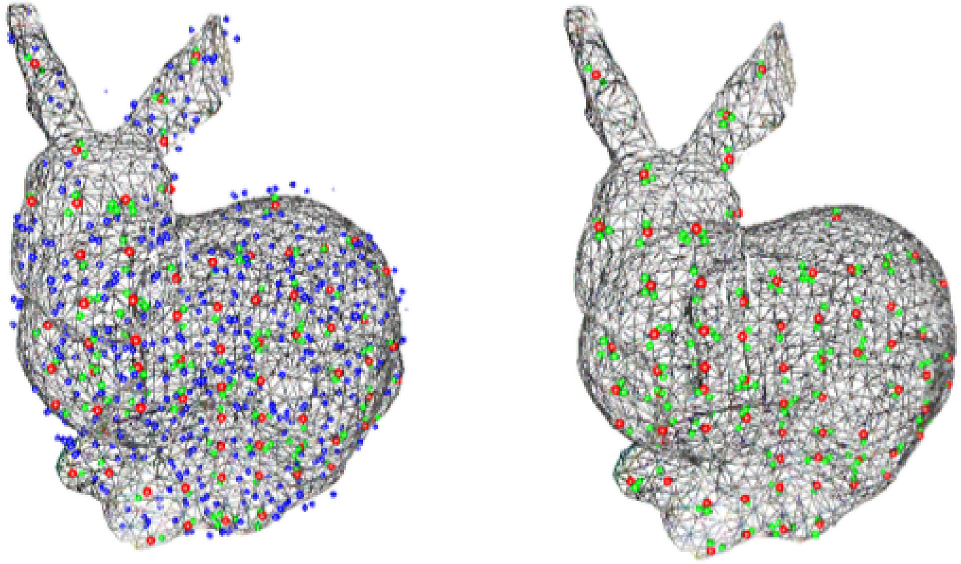

Fig. 3.5: Clustering phase : (left) The two views of 3D point cloud estimated from stereo matching. The Blue sphere represents the rejected features. (right) Image is a representation of the clusters. Red sphere represents the Control Points and the Green sphere the essential features (neighbors).

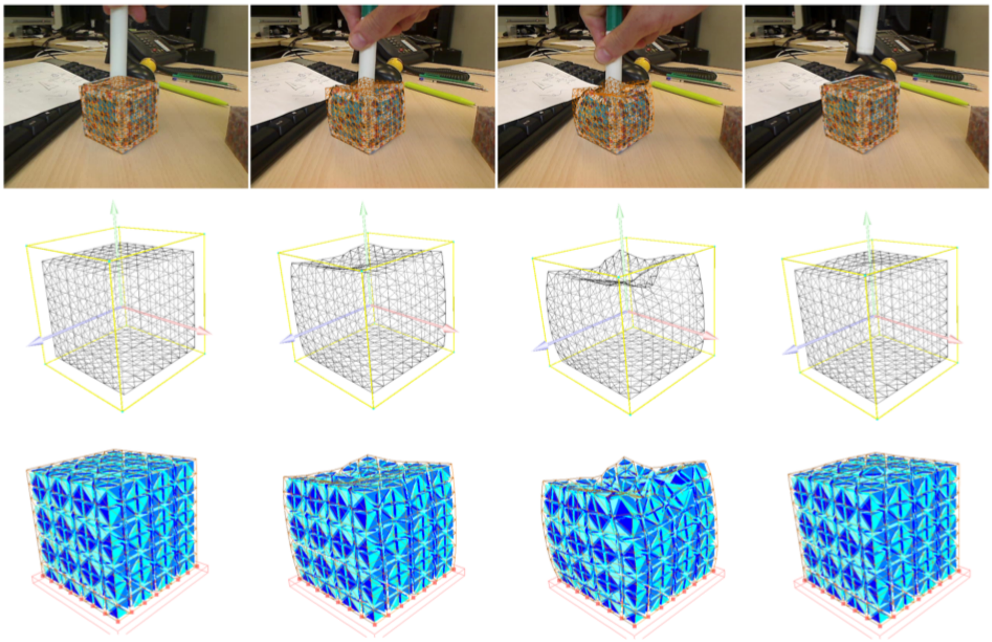

Fig. 3.6: A sequence of images showing a cube being deformed. (Top) augmented reality images where the mesh in wire-frame is superimposed on the video stream, (Middle) the deformed mesh, (Bottom) the volumetric mesh composed of tetrahedra.

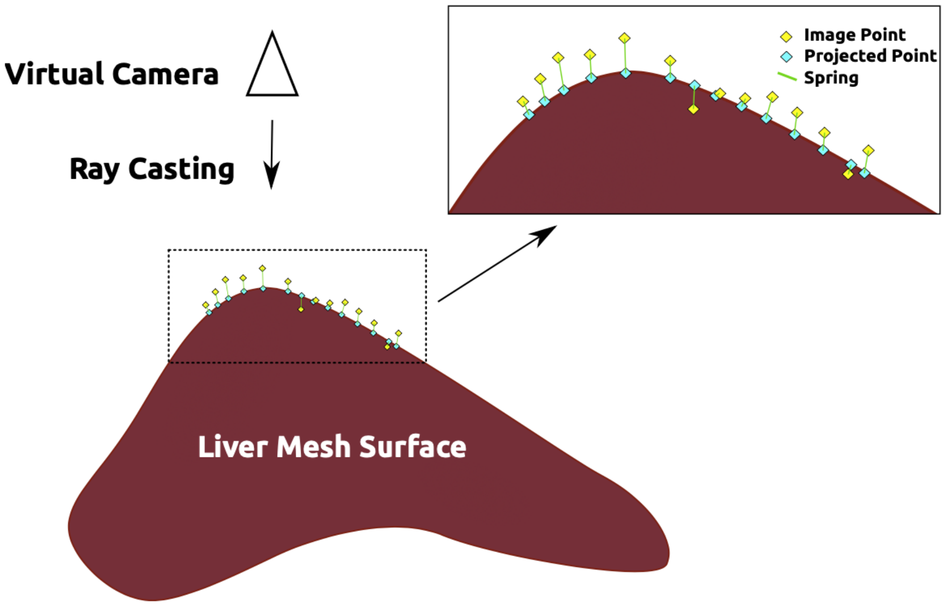

Fig. 3.7: Initial model alignment (simulated data): The mesh in purple represent the 3D model computed from CT scans in a different reference, the mesh in blue represents the MLS surface reconstructed from laparoscopic image pair. It represents around 30% of the whole liver that is represented in green.

that intersect the liver surface after ray-casting are kept, the features that do not belong to the liver are filtered out from laparoscopic images (see figure 3.7).

3.1.3 Implementation details

Non-rigid registration can be seen as a stretching energy minimization between the three dimensional features recovered from laparoscopic images that represent the tracking energy and the biomechanical model derived from preoperative CT data. External forces are defined by pairing the m 3D points y to the n degrees of freedom x of the biomechanical model. $\mathbf{f}_t(\mathbf{y}) = k\left(\mathbf{y} - \mathbf{y}^0\right)$ where $\mathbf{y}^0$ defines the tracked control points at time $t = 0$ and k can be defined as a stiffness. The tracked coordinates can be expressed using barycentric coordinates of adjacent degrees of freedom $\mathbf{y} = \mathbf{L}\mathbf{x}$.

To be as accurate as possible, boundary conditions representing the falciform ligament (ligament that attaches the liver to the front body wall) and the underlying fat needs to be defined. These boundaries conditions represents fixed parts of the liver that could not move or deform over time. The figure 3.8 illustrates boundary conditions on our model.

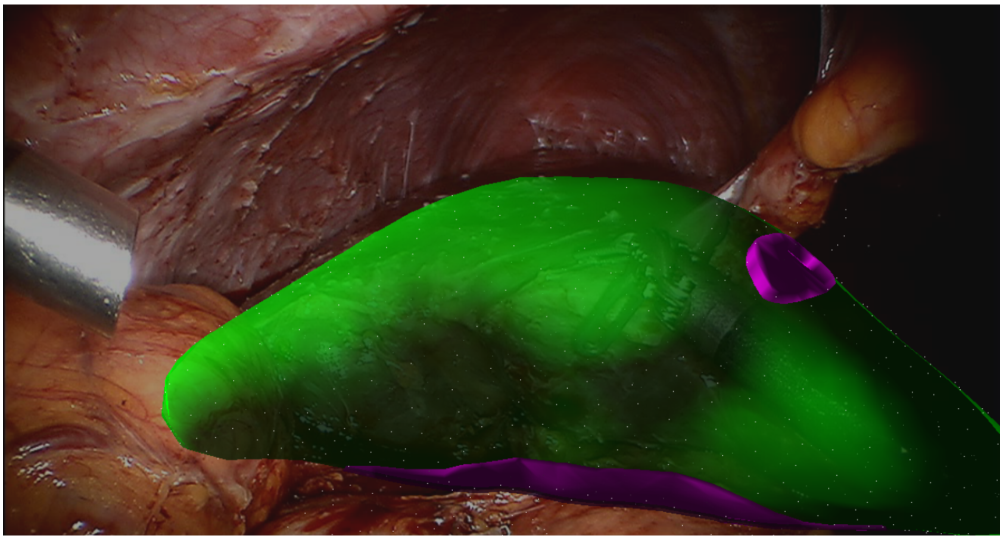

Fig. 3.8: Boundary conditions: The liver model (in green) is constrained by fixed vertices (in purple) that represent the falciform ligament and the underlying fat.

Given these additional concerns, the simulation is then performed at every time steps and external forces due to image tracking as well as internal forces due to liver model are computed.

3.1.4 Experimental Results

The validation of such framework is complex as clinical context makes it difficult to build an assessable, reproducible set-up in order to evaluate the performance of each element of the proposed pipeline. The thesis of Nazim Haouchine [Hao15] details the methodology we used in order to validate our approach: virtual validation with computer-generated data, *in-silico* experiment with silicone phantom, *ex-vivo* experiments with pig liver and *in-vivo* experiments with human data. The figure 3.9 illustrates some images extracted from a AR sequence where the liver has been successfully deformed based on the motion tracking. For the complete study and the quantitative results, we encourage the reader to refer to the PhD thesis of Nazim Haouchine.

3.2 Inverse FEM simulation for adaptive radiotherapy

Radiation therapy (or *radiotherapy*) is one of the possible treatments for head and neck cancers. It uses high-energy X-rays to destroy the cancer cells. A treatment is

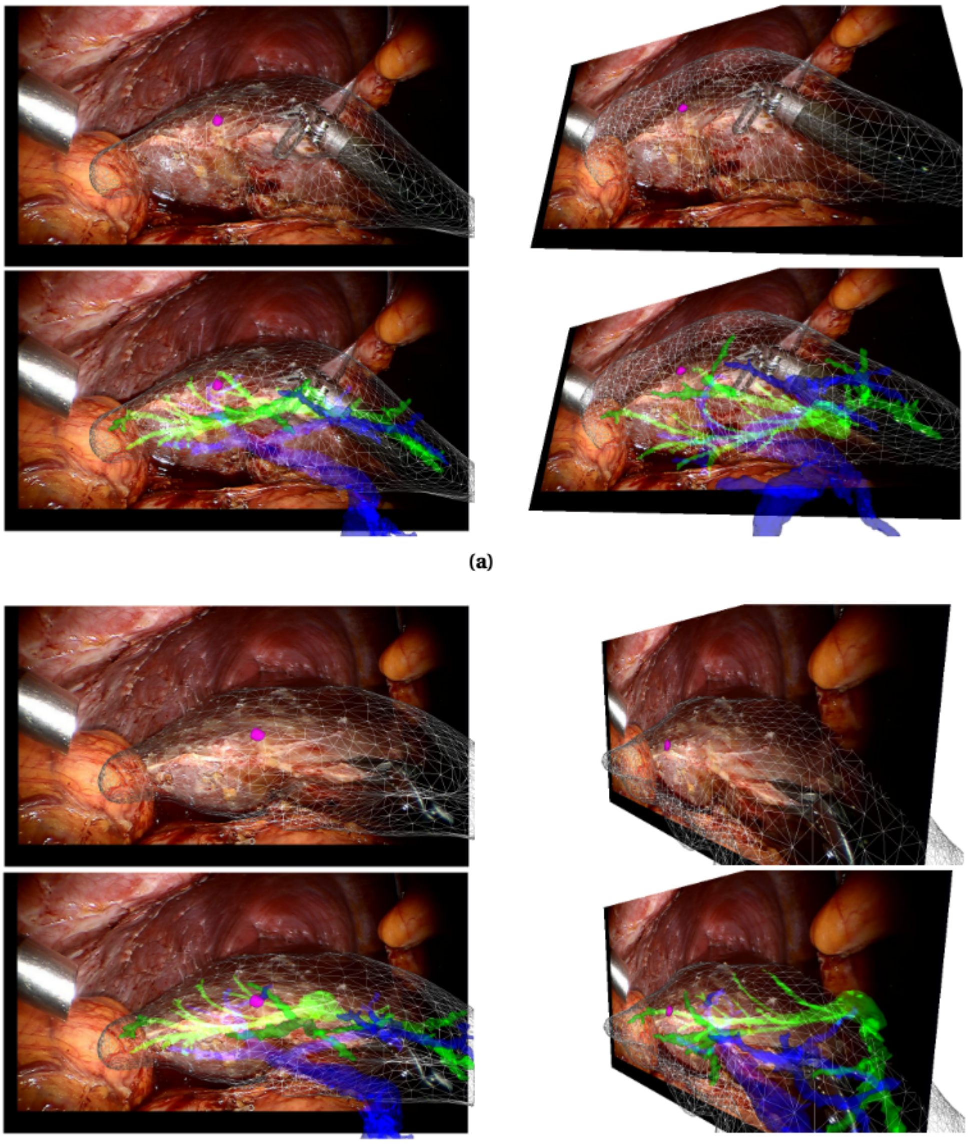

(a)

Fig. 3.9: A sequence of images showing the superimposition of the real-time biomechanical model onto the human liver undergoing deformation due to surgical instrument interaction. On the left virtual camera with the original laparoscopic angle and right a different angle.

established by using a treatment planning system (TPS) [Web03] which combines patient medical images, radiation transport simulations and optimization algorithms in order to expose tumors to X-rays while sparing healthy structures. The treatment plan is then applied 5 days per week during 6 to 7 weeks in order to destroy the tumors. During these 7 weeks, the patient is exposed to several side effects, and in particular an important weight loss. This induces the motion and deformation on the anatomical structures and the TPS does not take into account these topography changes, which may lead to an important X-ray exposure of healthy tissues [Nel+12] [Vei+14]. For instance it is reported [DNV06] that xerostomia (loss of saliva) is due to a higher (*than planned*) exposure of the parotid glands while treating throat cancers.

The main objective in this section is to adapt the planning to account for morphological modifications in order to limit the radiation exposure of healthy structures. It has been shown that non-rigid registration and daily computation of the dose can reduce the radiations [Vei+14]. But the challenge remain on the registration method over the 7-week period. While significant works have been achieved recently in the field of automatic non-rigid registration (the reader may refer to [CHH04] for a recent survey), these methods do not provide an easy control for the physicians. These algorithms also lack robustness and consistency when images are very complex. On the contrary, dealing with manual segmentations and/or registrations is time-consuming for the physicians and is not a viable solution for adapting the planning along with the treatment of the patients.

Our approach will be the same as in the previous section: using images to guide FEM models that represent the anatomical structures we want to track over time. But we want to improve it by avoiding to apply forces (or displacements) through the analysis of images since the physics of these boundary conditions is not correct (for a mechanical standpoint) as it mixes physics-based forces with image-based forces. As a result we will solve an inverse FEM simulation where several landmarks will guide the resolution of the problem.

3.2.1 Real-time Inverse FEM

Starting from what has been described in section 1.2, we extend the equations used for the resolution of real-time static FEM model. During each step i of the simulation, a linearization of the internal forces is computed:

$$\mathbf{f}(\mathbf{x_i}) \approx \mathbf{f}(\mathbf{x_{i-1}}) + \mathbf{K}(\mathbf{x_{i-1}})d\mathbf{x} \tag{3.2}$$

where $\mathbf{f}$ provides the volumetric internal stiffness forces at a given position $\mathbf{x}$ of the nodes, $\mathbf{K}(\mathbf{x})$ is the tangent stiffness matrix that depends on the actual position of the nodes and $d\mathbf{x}$ is the difference between consecutive positions in time $d\mathbf{x} = \mathbf{x_i} - \mathbf{x_{i-1}}$. The lines and columns that correspond to fixed nodes are removed from the system to improve the condition number of the matrix $\mathbf{K}$. Static equilibrium (the sum of external and internal force equals to zero) is sought at each step:

$$-\mathbf{K}(\mathbf{x_{i-1}})d\mathbf{x} = \mathbf{p} + \mathbf{f}(\mathbf{x_{i-1}}) + \mathbf{J}^T\boldsymbol{\lambda} \tag{3.3}$$

where $\mathbf{p}$ represents the external forces (*e.g.* gravity) that are known and $\mathbf{J}^T\boldsymbol{\lambda}$ gathers the contributions of the Lagrange multipliers. Three types of multipliers are defined:

- **boundary multipliers $\boldsymbol{\lambda}_b$**: we use these constraints to describes the external efforts applied on the boundary conditions that creates the deformation. The location of the boundary conditions are supposed to be known, the directions of the effort $\mathbf{J}^T$ can be updated at each step, and $\boldsymbol{\lambda}_b$ is the unknown intensity of the efforts on boundaries. We can set (and update at each step i) an interval of potential values $min \leq \boldsymbol{\lambda}_b \leq max$.

- **parameters multipliers $\boldsymbol{\lambda}_p$**: these parameters influence the computation of the internal forces.We use a local derivation of the internal force by the parameter p: $\mathbf{f}(\mathbf{x}, p + dp) \approx \mathbf{f}(\mathbf{x}, p) + (\delta\mathbf{f}(\mathbf{x}, p)/\delta p)dp$. In that case, $\mathbf{J}^T = \delta\mathbf{f}(\mathbf{x}, p)/\delta p$ and $\boldsymbol{\lambda}_b = dp$ is the variation of the parameter. To keep the validity of the local derivation over a step i, we can set $-\epsilon \leq \boldsymbol{\lambda}_p \leq \epsilon$.

- **registration multipliers $\boldsymbol{\lambda}_r$**: set interactively by the user to do a local manual registration on a small number of points.

Contrary to a lot of existing registration methods, we do not put any force (or energy) to the association of points or on image pixels so $\boldsymbol{\lambda}_r = 0$. Even if null, these multipliers are useful to build the optimization problem.

Indeed, the next step consists of the projection of the FEM model equations into the constraint space: the size of matrix $\mathbf{K}$ is often very large so an optimization in the motion space would be computationally very expensive. Instead, using the Schur complement (also called Delassus operator) of the constraint problem, we do a projection that dramatically reduces the size of the research space.

Three steps are followed, that are *standard* in a constraint solving process:

- **Step I**, a free configuration $\mathbf{x}_{\text{free}}$ of the deformable model is found by solving equation (3.3) with $\boldsymbol{\lambda} = 0$. For the constraint defined on registration point, we compute a *violation* noted $\boldsymbol{\delta}_r^{\text{free}}$ which provides a vector between the registered position of the points and the position given during the free motion.

- **Step II**: This step is central in the method. It consists in projecting the mechanics into the constraint space. As the constraints are the inputs (registered points) and outputs (parameters and efforts on boundary) of the inverse problem, we obtain the smallest possible projection space for the inverse problem:

  $$\boldsymbol{\delta}_r = \underbrace{\left[\mathbf{J}_r\mathbf{K}^{-1}\mathbf{J}_p^T\right]}_{\mathbf{W}_{rp}} \boldsymbol{\lambda_p} + \underbrace{\left[\mathbf{J}_r\mathbf{K}^{-1}\mathbf{J}_b^T\right]}_{\mathbf{W}_{rb}} \boldsymbol{\lambda_b} + \boldsymbol{\delta}_r^{\text{free}} \tag{3.4}$$

  $\boldsymbol{\delta}_r$ represents a vector between registered and actual positions of points chosen by the user. Then a Quadratic Programming (QP) problem is set by minimizing the norm of this vector.

  $$min(\frac{1}{2}\boldsymbol{\delta}_r^T\boldsymbol{\delta}_r) = min(\frac{1}{2}\begin{bmatrix}\boldsymbol{\lambda_p}\\ \boldsymbol{\lambda_b}\end{bmatrix}^T\begin{bmatrix}\mathbf{W}_{rp}^T\\ \mathbf{W}_{rb}^T\end{bmatrix}\begin{bmatrix}\mathbf{W}_{rp} & \mathbf{W}_{rb}\end{bmatrix}\begin{bmatrix}\boldsymbol{\lambda_p}\\ \boldsymbol{\lambda_b}\end{bmatrix}+\begin{bmatrix}\boldsymbol{\lambda_p}\\ \boldsymbol{\lambda_b}\end{bmatrix}^T\begin{bmatrix}\mathbf{W}_{rp}\\ \mathbf{W}_{rb}\end{bmatrix}\boldsymbol{\delta}_r^{\text{free}})$$

  $$\text{subject to}\ \ min \leq \boldsymbol{\lambda_b} \leq max \quad \text{and} \quad -\epsilon \leq \boldsymbol{\lambda_p} \leq \epsilon \tag{3.5}$$

  The size of the QP problem is much smaller than solving the problem in the motion space of equation 3.3, allowing to solve this problem in real-time. In practice, the QP matrix is always positive and definite iff the size of $\boldsymbol{\delta}_r$ is greater than the number of optimized values in $\boldsymbol{\lambda_p}$ and $\boldsymbol{\lambda_b}$.

- During **Step III**, the final configuration of the deformable model is corrected by using the value of the constraint response using $\mathbf{x}_i = \mathbf{x}_{\text{free}} + \mathbf{K}^{-1}(\mathbf{J}_p^T\boldsymbol{\lambda}_p + \mathbf{J}_b^T\boldsymbol{\lambda}_b)$. In practice, we use a LDL^T factorization of the matrix $\mathbf{K}$ and not $\mathbf{K}^{-1}$ during the computation.

3.2.2 Experimental validation

In this section, we present the application of the method in the context of radiotherapy of the neck (throat cancer) where patient weight loss induces deformations of anatomical structures that are not taken into account in the treatment. At the beginning of each therapy session, a scan of the patient is taken and a rigid registration of the planning to the actual position of the patient is realized. In order to facilitate this registration, the patient is wearing a rigid mask. Notably, the deformations of the parotids make them move towards the center of the neck and eventually intersect the main target volume of the therapy (see figure 3.10). Consequently parotids may be irradiated more than initially planned leading to xerostomia (20% of patients).

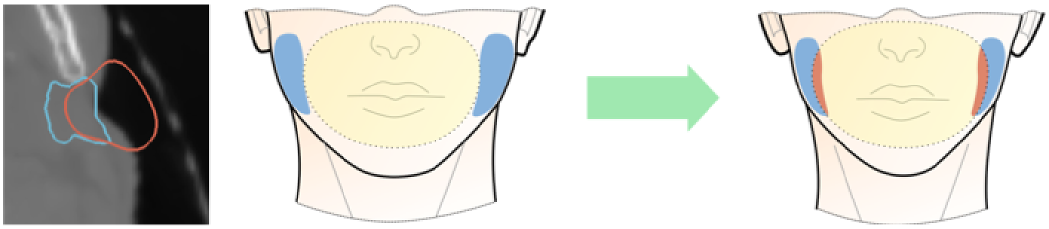

Fig. 3.10: Volume loss of parotids: (Left) segmentations of the parotids at weeks 1 (red) and 6 (blue). It is worth noticing the volume loss of the parotid as well as the motion of the center of mass. These two parameters have been used to characterize the deformation of parotids in [Bar+04]. (Right) Due to weight loss, parotids may intersect the target volume (in yellow).

Yet, with a robust registration performed just before the therapy, the planning could be adjusted. We emphasize that the parotids are poorly visible in the images, making the automatic registration not robust. With our inverse approach, the radiotherapist can use his expertise (knowledge of anatomy and meaningful parameters used in medical studies) to perform the registration and he/she will have a direct control of the parameters used for the registration. For instance [Bar+04], studied the parotids deformation by performing CT scans of the patient three times a week during the entire treatment. Form that study, the deformation of the parotids is characterized by two parameters: the volume loss of the parotids and the motion of its center of mass (due to the volume loss of other structures). Parotids deformations observed are large (more than 30 % the size of the structure) and can not be captured with linear models.

The current medical routine does not adapt the treatment since it involves the manual segmentation of the structures -which is time and manpower consuming- and the computation of the new planning. However our method can dramatically reduce the time required to adapt the planning while achieving comparable accuracy to manual segmentation. We tested our approach on a *ground truth* set of 7 patient datasets that contains the 3D images of the CT scan done every week of the therapy (total: 7*6 images). Comparison between manual segmentations of the parotids (performed by the radiologists) and our method is achieved on all available images (42) by computing the DICE coefficient. A single dataset (6 images) has been manually segmented by two radiologists and an average DICE coefficient of 0.7 has been computed to serve as a reference for the quality of our method. On these data, our method can be executed very quickly (completion of the registration is done in a single minute) with respect to a full manual segmentation making it compatible with the time constraints of a clinical routine. The graph 3.11 (left) illustrates that the parotids deformation is significant and second that our method exhibits really good similarity compared to manual segmentation (average DICE between [0.8;0.9]).

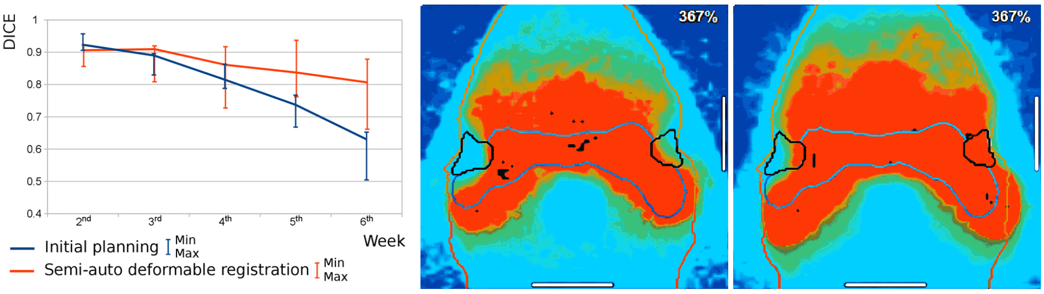

Fig. 3.11: Validation: (left) similarity between the initial segmentation and *ground truth* geometry in blue curve illustrates the deformation of the parotids (DICE decreasing), the red curve exhibits the good similarities between our semi-automatic registration and the *ground truth* geometry; (middle) planning adaptation using our registration vs no planning adaptation (right). The measured radiation is much lower when the planning is adapted.

Efficiency of the whole approach: A dataset was selected for which the deformations were important and the parotids were not infiltrated by the tumor (therefore out of the target volume). We have a closer look at the last session of the therapy and particularly at the irradiation map of the parotids without considering planning adaptation 3.11 (right) and with planning adaptation using our method to register the right parotid (middle). The resulting maps from the TPS show that the irradiation of the right parotid is significantly reduced and may limit the appearance of irradiation side-effects.

3.3 Motion Control for Interventional Radiology Procedures

Using FEM in an inverse problem as in the previous section has been then an approach that we have used in many robotics application for instance to build a closed-loop control for a robot [Zha+16] or to perform visual servoing [Zha+17] or to combine computer vision and inverse model to use the robot as a cheap force sensor [ZDD18b]. We choose not to detail all these works as the reader can refer to them, but we will focus on a work that combine robotics and interventional radiology. We already have explained in the previous chapters (more specifically in chapter 1.5.2) that interventional radiology procedures requires excellent eye-hand coordination and strong expertise to anticipate how the radiology devices (*catheters, guide-wires*...) will behave inside the vascular network. Complementary to the training and planning tools we have proposed, a clinical application providing the automatic or semi-automatic control of a robotized catheter actuated by cables. Without removing the radiologist from *the loop*, we would like to consider a clinical scenario where the radiologist defines a path that the catheter must follow given some per-operative medical images and our control algorithm actuates the robotized catheter to follow this trajectory. This work has been conducted in collaboration with Junghwan Back and Hongbin Liu from Kings College London and the catheter robot used was an upgraded version of [Bac+18]. This catheter robot has a polymer material structure which is MR-compatible, has a diameter of 7mm in order to

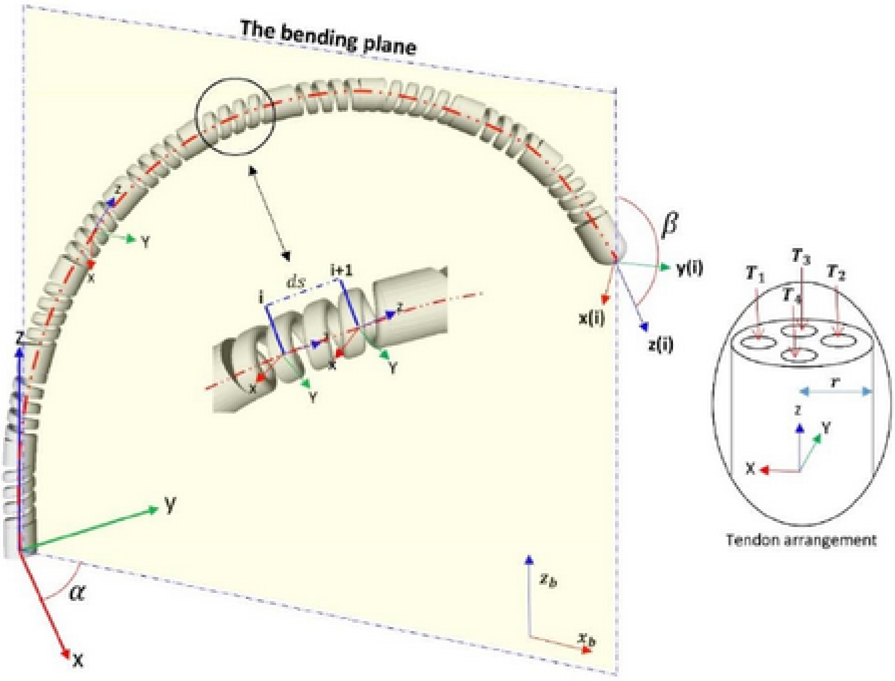

Fig. 3.12: Catheter robot from Kings College London with a polymer structure and 4 tendons that enables the robot tip to bend.

3.3.1 Simulation with actuation and contacts

The control of soft robot like the catheter we use requires the simulation of soft structures. The simulation of soft robots is no different from the simulation of anatomical structures and as a consequence we will use the methods we have detailed so far in this manuscript. More specifically the control of the robot requires to solve an inverse problem and we will use the methodology described in the previous section. Given the equilibrium equation, we use the Schur complement of the constraint problem, then the FE model equation can be projected into the constraint space that drastically reduces its size. Then, we can compute the following variables at any step k given variables at step $k-1$:

$$\delta_{e,k} = \mathbf{W}_{ea}\left(\mathbf{x}_{k-1}\right)\lambda_{a,k} + \mathbf{W}_{ec}\left(\mathbf{x}_{k-1}\right)\lambda_{c,k} + \delta_{e,k}^{free} \tag{3.6}$$

$$\delta_{a,k} = \mathbf{W}_{aa}\left(\mathbf{x}_{k-1}\right)\lambda_{a,k} + \mathbf{W}_{ac}\left(\mathbf{x}_{k-1}\right)\lambda_{c,k} + \delta_{a,k}^{free} \tag{3.7}$$

$$\delta_{c,k} = \mathbf{W}_{ca}\left(\mathbf{x}_{k-1}\right)\lambda_{a,k} + \mathbf{W}_{cc}\left(\mathbf{x}_{k-1}\right)\lambda_{c,k} + \delta_{c,k}^{free} \tag{3.8}$$

where the following variables are defined as:

- subscript a refers to the actuators, subscript e refers to the end-effector and subscript c refers to the contacts
- $\delta_{e,k}$ Position vector of effectors at step k
- $\delta_{a,k}$ Position vector in the actuator space at step k
- $\delta_{c,k}$ Position vector in the contact space at step k
- each matrix $\mathbf{W}_{ij}$ is defined as $\mathbf{W}_{ij}\left(\mathbf{x}_k\right) = \mathbf{J}_i\left(\mathbf{x}_k\right)\mathbf{K}^{-1}\left(\mathbf{x}_k\right)\mathbf{J}_j^T\left(\mathbf{x}_k\right)$. The couples (i,j) could take the values $(i,j) = (e,a); (e,c); (a,a); (a,c); (c,a); (c,c)$. Then:
  - $\mathbf{W}_{ea}(\mathbf{x})$ is the compliance matrix between effectors and actuators,
  - $\mathbf{W}_{ec}(\mathbf{x})$ is the compliance matrix between effectors and contacts,
  - $\mathbf{W}_{aa}(\mathbf{x})$ is the compliance matrix between actuators
  - $\mathbf{W}_{ac}(\mathbf{x})$ is the compliance matrix between actuators and contacts,

  - $\mathbf{W}_{ca}(\mathbf{x})$ is the compliance matrix between contacts and actuators,
  - $\mathbf{W}_{cc}(\mathbf{x})$ is the compliance matrix between contacts.
- $\lambda_{a,k}$ is the force contribution vector of actuators (at step k)
- $\lambda_{c,k}$ is the force contribution vector of contacts (at step k)
- $\delta_{a,k}$ is the position vector in the actuator space (at step k). $\delta_{a,k}^{free}$ represents the corresponding position vector when no forces are applied ($\lambda_{a,k} = 0$ and $\lambda_{c,k} = 0$)
- $\delta_{e,k}$ is the position vector of effectors (at step k). $\delta_{e,k}^{free}$ represents the corresponding position vector when no forces are applied ($\lambda_{a,k} = 0$ and $\lambda_{c,k} = 0$)
- $\delta_{c,k}$ is the position vector in the contact space (at step k).$\delta_{c,k}^{free}$ represents the corresponding position vector when no forces are applied ($\lambda_{a,k} = 0$ and $\lambda_{c,k} = 0$)

Without contacts and with actuation only, the position of the soft robot is defined as:

$$\mathbf{x}_{k+1} = \mathbf{K}_k^{-1}\mathbf{H}_a^T \cdot \lambda_k + \mathbf{x}_k^{\text{free}} \tag{3.9}$$

When contacts are considered, the collision response is based on the Signorini's law [Sig33]. For every contact point, there is a complementarity relation between the interpenetration gap $\delta_{c,k}$ and the contact force $\lambda_{c,k}$ among the normal direction. The complementarity relation can be written as [DAK04]:

$$\mathbf{0} \leq \delta_{c,k} \perp \lambda_{c,k} \geq \mathbf{0} \tag{3.10}$$

where $\perp$ is the complementarity operator. It states that each step k of the simulation either the forces due to contacts ($\lambda_{c,k}$) are null or that no DOF is in contact with obstacles ($\delta_{c,k} \neq 0$). Using equations 3.8 and 3.10, the LCP could be written as:

$$\mathbf{W}_{ca}\lambda_a + \mathbf{W}_{cc}\lambda_c + \delta_c^{free} \geq 0 \tag{3.11}$$

$$\lambda_c \geq 0 \tag{3.12}$$

$$\lambda_c^T \left(\mathbf{W}_{ca}\lambda_a + \mathbf{W}_{cc}\lambda_c + \delta_c^{free} \right) = 0 \tag{3.13}$$

3.3.2 Control design

In a constrained environment, [YC14] have highlighted two canonical problems for the control design of continuum robots if contacts are not taken into account in the closed loop design: artificial singularity and inverted mapping (see figure 3.13). Without taking contacts into accounts, the control could lead to a positive-feedback loop. Both the artificial singularity and the inverted mapping are generated by the coupling between the insertion and bending. Therefore, to avoid the two canonical problems, we propose a decoupled control strategy by decoupling the insertion and the bending. Besides, it aims to increase the insertion safety because it enables automatic bending control and manual insertion control.

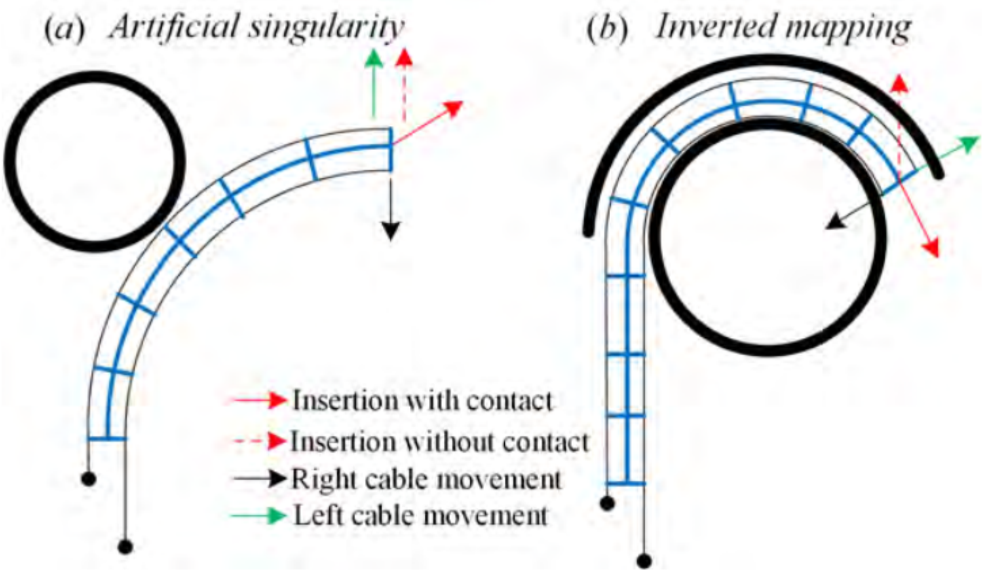

Fig. 3.13: Two canonical cases described where the contacts highly influence the kinematics of the catheter robot. Arrows are the motion directions of the tip for imposed motion at the base: insertion, right cable movement, left cable movement. (a) artificial singularity and (b) inverted mapping result in the deterioration and even the positive-feedback loop.

The proposed closed-loop strategy (see figure 3.14) needs to combine both the catheter robot and its FE model which is simulated in real-time. The FE model is employed to compute the Jacobian matrix and to detect collisions between the robot and the environment. The same insertion input δ_{in} is sent to both the catheter robot and its FE model.

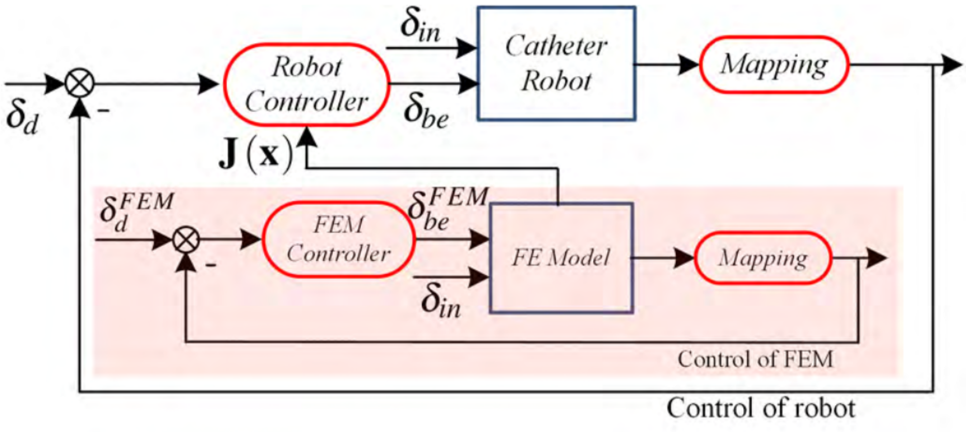

Fig. 3.14: Framework of decoupled closed-loop bending control for catheter robot through contacts. For the implementation, the FE model of catheter robot and its environment is simulated in real-time. The insertion and bending are decoupled by the projection block which is introduced in Section IV.A. Two independent controllers are employed for the control of catheter robot and its FE model respectively. δ_d and δ_{be} are respectively the desired position and the bending control inputs for the catheter robot, while and δ_{FEM} are the corresponding variables for the FE model. δ_{in} insertion input for both the catheter robot and the FE model.

Projection step

The projection component is used to decouple the insertion and the bending for the catheter robot. The movement of catheter robot is modeled in 3D space defined by the coordinate system $OXYZ$. To achieve the projection, the local coordinate system $Pxyz$ is computed at each step based on the 3D tip position and the predefined trajectory so that it moves with the insertion of catheter robot. After the projection process, the movement of catheter tip in 3D space is converted to the insertion along the tangent axis x and the bending movement in 2D plane defined by the normal axis z and the projection axis y.

FEM Controller design

The objective of the closed-loop controller for the FE model is that the effector of the FE model (δ_e) converges towards the desired location (δ_d). We can define an optimization problem where we want to find the forces λ that minimizes the objective function Γ:

$$\Gamma(\lambda) = \frac{1}{2} \left\| \mathbf{W}_e \lambda + \delta_e^{free} - \delta_d \right\|^2 \tag{3.14}$$

We can add some constraints on the forces that should be generated such as $0 \leq \lambda_c \leq \lambda_{c,max}$ to limit the magnitude of contact forces or $\lambda_{a,\min} \leq \lambda_a \leq \lambda_{a,\max}$ to take into account the physical limitations of actuators. This optimization problem is rewritten as a QP-problem that can be solved using dedicated software packages. The reader may refer to our journal paper [Zha+19b] for equations details. In this end we obtain a standard QP-problem:

$$\begin{array}{ll} \min_\lambda \frac{1}{2} \lambda^T \mathbf{Q} \lambda + \mathbf{c}^T \lambda & \\ \text{s.t.} \quad 0 \leq \lambda \leq \lambda_{\max} & \\ \text{and} \quad \mathbf{W}_c \lambda + \delta_c^{free} \geq 0 & \end{array} \tag{3.15}$$

where we make the assumption that the defined trajectory is always reachable. In practice, with assumption of static environment, we plan it off-line and make sure that it is always reachable by our robot.

Robot Controller design

Given equations formulated in subsection 3.3.1, we can express the position of the effector given compliance matrices in:

$$\delta_{e,k+1} = \delta_{e,k} + \mathbf{J}\left(\mathbf{x}_k\right) \Delta \delta_{a,k} \tag{3.16}$$

where $\mathbf{J}\left(\mathbf{x}_k\right) = \mathbf{W}_{ea}\left(\mathbf{x}_k\right) \mathbf{W}_{aa}^{-1}\left(\mathbf{x}_k\right)$ is the Jacobian matrix of the robot. Given this Jacobian, the control vector $U_k = \mathbf{J}\left(\mathbf{x}_k\right) \Delta \delta_{a,k}$ allows to rewrite the kinematic model as:

$$\delta_{e,k+1} = \delta_{e,k} + U_k \tag{3.17}$$

The tracking error is defined as $e_k = \delta_{e,k} - \delta_{d,k}$. In the task space, the control vector U_k can be designed as:

$$U_k = -K_P e_k - K_D \left(e_k - e_{k-1}\right) \tag{3.18}$$

where K_P and K_D are constant parameters for the proportional gain and differential gain respectively. Then, the Pseudo-inverse based control allocation is employed to obtain a unique solution:

$$u = \mathbf{J}^{+}\left(\mathbf{x}_k\right) U_k \tag{3.19}$$

$$u = -\mathbf{J}^{+}\left(\mathbf{x}_k\right)\left[K_P e_k + K_D\left(e_k - e_{k-1}\right)\right] \tag{3.20}$$

3.3.3 Experimental validation

In order to validate this approach, we use a commercial electromagnetic tracking system (Aurora tracking from NDI company) with the sampling frequency 20Hz and the sub-millimetric accuracy. A rigid tube (diameter 28mm) is fixed with respect to the base of the catheter robot. Positions of seven feature points are captured by the tracking system and are employed for the calibration between the coordinate system of the sensor and that of the robot. The movement of catheter robot consists of bending and insertion.

Fig. 3.15: Experimental setup for the motion control of a catheter robot through contacts. (a) NDI electromagnetic tracking system: Aurora; (b) a rigid tube for the experiment. The white points are the feature points which are used for the calibration; (c) the cable-driven continuum catheter robot which has four step motors to actuate the bending and one step motor to control the insertion.

The positioning results are shown in figure 3.16 which includes two cases with different catheter length (60 mm and 166 mm). The tracking error converges faster when the length of catheter is shorter. For both cases, the positioning errors converge to a small bound (around 0.2mm). Usually a longer length of catheter robot generates a larger convergence bound if there is no interaction with the environment. However, in our experiments, the contacts limit the deflection and therefore reduce the convergence bound.

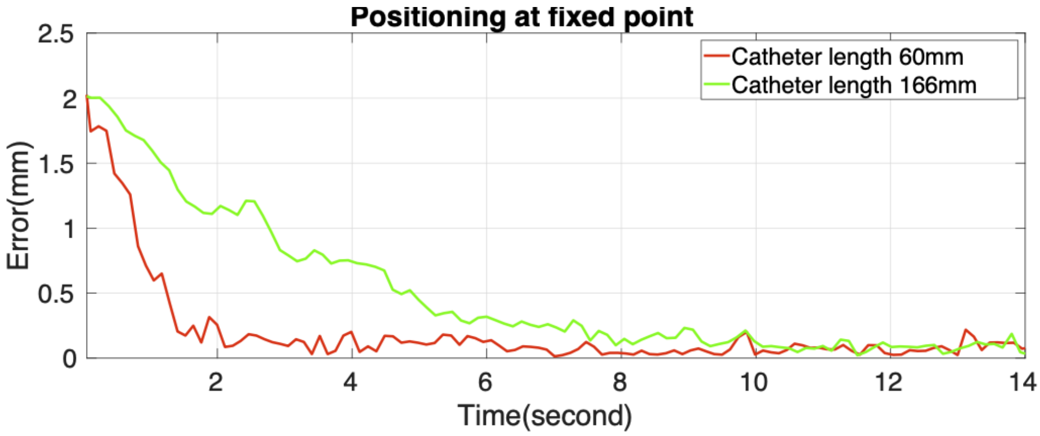

Fig. 3.16: Experimental setup for the motion control of a catheter robot through contacts. (a) NDI electromagnetic tracking system: Aurora; (b) a rigid tube for the experiment. The white points are the feature points which are used for the calibration; (c) the cable-driven continuum catheter robot which has four step motors to actuate the bending and one step motor to control the insertion.

Additional experiments were conducted using only simulation in order to focus on the control algorithms themselves and can get rid of the sensor noise, imprecise modeling of robot and contacts. As shown in figure 3.17, the catheter robot can be controlled from the initial configuration (a) to the finial configuration (b) with the decoupled control strategy. If the insertion and bending are coupled between each other, the Jacobian matrix is inverted during the movement. However, the decoupled control strategy can successfully avoid the problem of the Jacobian matrix rotation when the robot interacts with the contacts.

The trajectory tracking can also be achieved when the catheter robot interacts with soft contacts. The decoupled control strategy is employed and validated using simulation which is shown in figure 3.18. To estimate the Jacobian matrix and contact forces, both catheter robot and soft tube are modeled using FE method and are simulated in real-time.

3.4 Perspectives

The three different applications presented in this chapter illustrate how the foundational works presented in the manuscript could open up for new high-value applications in different fields. The combination of interactive (or at least *fast*) simulation of

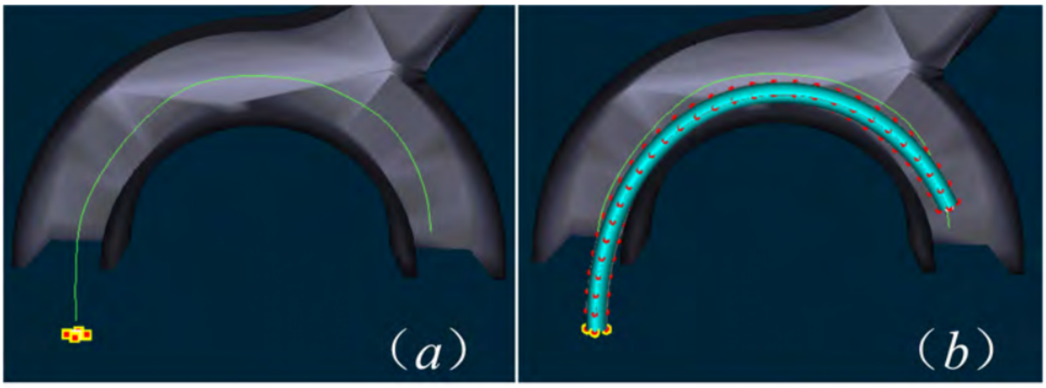

Fig. 3.17: Experimental setup for the motion control of a catheter robot through contacts. (a) NDI electromagnetic tracking system: Aurora; (b) a rigid tube for the experiment. The white points are the feature points which are used for the calibration; (c) the cable-driven continuum catheter robot which has four step motors to actuate the bending and one step motor to control the insertion.

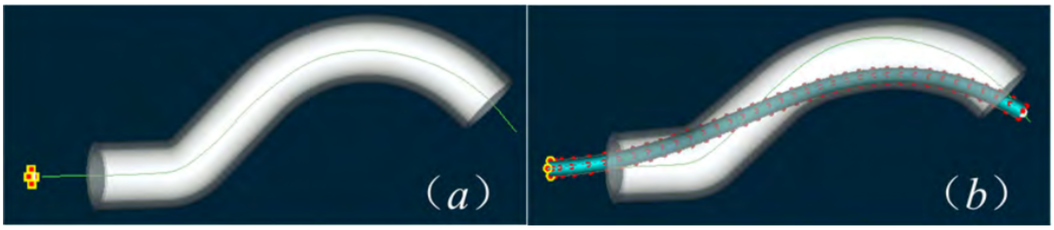

Fig. 3.18: Experimental setup for the motion control of a catheter robot through contacts. (a) NDI electromagnetic tracking system: Aurora; (b) a rigid tube for the experiment. The white points are the feature points which are used for the calibration; (c) the cable-driven continuum catheter robot which has four step motors to actuate the bending and one step motor to control the insertion.

deformable objects with computer vision and automatic control could provide many beneficial outcomes in surgery, interventional radiology or robotics. We also want to emphasize on the fact that these applications require real multi-disciplinary approach to be really efficient: some components are developed throughout the manuscript but some technical others like software programming, algorithm optimization and modular software platform are mandatory to achieve these applications. A standard unified platform that includes all these aspects would help the simulation and robotics community but the standard is still to emerge. SOFA[1] is an attempt to answer these technical deadlocks and all the applications or simulations presented in this manuscript were built using SOFA.

---

[1] www.sofa-framework.org

Conclusion

> *I didn't think; I experimented.*
>
> — **Anthony Burgess**

This manuscript presented several research works conducted these past year. Focusing on interactive simulations for deformable objects, we have proposed some contributions to the modeling of deformable solids, to the optimization of simulation and some training applications that can be derived from these works. We also shown that these simulations need to rely on accurate data to be really useful. Since medical images are used extensively in clinical routine, we have proposed some methods to build simulation-compatible data from images and we have also illustrate how the data, if acquired in run-time, could be used to guide or increase the prediction capabilities of simulation. The combination of interactive simulations and computer vision algorithm have led to several applications whose outcomes are more than training tools... and we have illustrate some examples such as a planning tool for radiotherapy or an augmented reality tool that enables interactive per-operative guidance for surgeons. These successful combination is not limited to augmented reality / virtual reality applications for medicine but can also be employed in robotics. The algorithmic principles can be derived and using automatic control methods we have developed some applications for automatic controls of soft robots.

Several perspectives for my research works can be issued from this summary and the state-of-the-art. A lot of attention has been directed to artificial intelligence / supervised (*deep*) learning and these past few years have seen numerous papers using model-free methods based on AI to solve simulations or automatic controls issues... this has led to an opposition between model-free researchers and model-base researchers. While the benefits of supervised learning are indisputable, the main limitation is the huge volume of data to train the neural networks used for the learning. Some application contexts can provide relatively easy all the data needed but our experience in medical applications shows that large and most important relevant data are really complex to acquire: medical images are abundantly available but they should pass through several filters some social (ethical committees, anonymization. . .) some technical (segmentation, reconstruction. . .) and there are still some limitations such as the acquisition speed in case of dynamic images or the fact that these images contain mostly geometric data... which are not sufficient for mechanical simulation. Our vision for the next few years to combine the prediction capabilities of AI with the scenario generation of simulations: simulation can create a virtual testbed that can produce / reproduce many clinical procedures, pathologies, complications... that can be recorded to be used to train the supervised learning algorithms. For that context, interactive applications is not necessarily a requirement but the faster the simulations the faster it can produce the amount of data needed. Thus all the deadlocks related to simulation speed or simulation optimizations that we have mentioned in chapter Interactive Physics-based Simulation are still relevant and worthy to investigate. We had a collaboration with a company (Robocath) about the automatic navigation of catheter in cardiac interventional radiology that uses the combination of approaches and the results are promising. Some of these results have been published in [Sch+22] and [Zha+22] and we plan to extend them in the future.

A second perspective is mostly related to the previous one, as (dynamic) 2D / 3D imaging techniques are available through medical imaging devices, 3D scanners or cameras... the amount of geometric data generated is huge. These data, while directly usable for visualization or rendering, are not suited for mechanical simulation: topologies may exhibit some unexpected artifacts like unwanted holes, very low mesh quality (lots of degenerated triangles)... As a consequence, a time-consuming and tedious post-processing step is mandatory and most of the times this is done with the expertise of someone that possess simulation and geometric modeling skills. Moreover since modeling softwares uses triangular mesh representation for virtual objects, they lack the ability to define volumetric properties that are required by 3D mechanical simulation and they are the best representation for 3D objects. In the chapter Geometric Modeling for Interactive Simulation, we have made an attempt to use implicit surfaces as object representation because of its intrinsic properties (geometric continuity, smoothness) and because it speeds-up drastically the computation time of the collision detection step in the simulation. With the rise of new graphics cards that include hardware ray casting (which can be used for collision detection as well as rendering) like in the RDNA Architecture from AMD, we could expect significant speed-ups in the simulation by using these features with implicit surfaces. The major scientific deadlock remains how to build implicit surfaces with an arbitrary geometry (be it a triangular mesh or a point cloud). What we have proposed in the second chapter is relevant for tubular structures but it cannot be derived for arbitrary shapes. Therefore we want to investigate this field with having always interactive simulation as a target (thus aiming for a compact representation of surfaces).

A third perspective is related to the difficulties encountered for the experimental validation of our approaches. We lack ground truth data in the medical simulation community or in the soft robotics community. Since we aim at providing methods that can be derived into medical applications used in clinical routine or robotics applications used in industry or surgery, special care should be taken to validate experimentally in scenario that are close to *in-vivo* situations. A gradual approach ranging from computer validations to *in-vivo* validations stepping by *in-silico* and *ex-silico* validations appears to be relevant, it cannot be done in every context. Silicone phantoms that we have used numerous time in the chapter Medical and Robotic Applications enables to provide a reproducible and assessable testbed for validations. They, however, lack dynamic features (motion and deformation) that can mimic anatomical soft structures. Our proposal for the next years is to build controllable and instrumented soft robots that reproduce anatomical soft bodies. This research direction combines simulation, automatic control and soft robots design in order to produce a validated testbed where motion can be controlled (to mimic cardiac cycle for cycle), elastic deformations are known or measurable, forces are measured. . . over time. We think this step is mandatory to fasten the time needed to go from the research paper to the pre-industrial prototype. In order to accelerate on this perspective, I submitted a proposal for an european call that includes researchers from university of Copenhagen, Universidad Rey Juan Carlos (Madrid) and Vrije Universiteit Brussel to build soft robotized twins of organs and anatomical structures.

These three research directions are not only extensions of the three chapters presented in this manuscript. From the capitalization of our research experience these past 10 years and the integration of recent works and recent collaborations, we have identified these three topics were we can have an impact and provide original contributions. The first two can be investigated in parallel while the third one is more transverse and multi-disciplinary and will require a network of collaborations to fill the different expertise we need.

Bibliography

[AC04] Gallagher AG and Cates CU. “Approval of virtual reality training for carotid stenting: What this means for procedural-based medicine”. In: *JAMA* 292.24 (2004), pp. 3024–3026 (cit. on p. 2).

[AKN07] T. Alderliesten, M.K. Konings, and W.J. Niessen. “Modeling Friction, Intrinsic Curvature, and Rotation of Guide Wires for Simulation of Minimally Invasive Vascular Interventions”. In: *Biomedical Engineering, IEEE Transactions on* 54.1 (Jan. 2007), pp. 29–38 (cit. on p. 54).

[Bac+18] Junghwan Back, Lukas Lindenroth, Kawal Rhode, and Hongbin Liu. “Three dimensional force estimation for steerable catheters through bi-point tracking”. In: *Sensors and Actuators A: Physical* 279 (2018), pp. 404–415 (cit. on p. 130).

[Ban+12] Jordan Bano, Alexandre Hostettler, SA Nicolau, Stephane Cotin, Christophe Doignon, HS Wu, MH Huang, Luc Soler, and Jacques Marescaux. “Simulation of pneumoperitoneum for laparoscopic surgery planning”. In: *International Conference on Medical Image Computing and Computer-Assisted Intervention*. Springer. 2012, pp. 91–98 (cit. on p. 118).

[Bar+04] Jerry L Barker Jr, Adam S Garden, K Kian Ang, Jennifer C O’Daniel, He Wang, Laurence E Court, William H Morrison, David I Rosenthal, KS Clifford Chao, Susan L Tucker, et al. “Quantification of volumetric and geometric changes occurring during fractionated radiotherapy for head-and-neck cancer using an integrated CT/linear accelerator system”. In: *International Journal of Radiation Oncology* Biology* Physics* 59.4 (2004), pp. 960–970 (cit. on p. 128).

[Bar+94] Victor Barrios, J Torres, Guillermo Montilla, Lilia Hernandez, Naykiavic Rangel, and A Reigosa. “Cellular edge detection using a trained neural network explorer”. In: *Engineering in Medicine and Biology Society, 1994. Engineering Advances: New Opportunities for Biomedical Engineers. Proceedings of the 16th Annual International Conference of the IEEE*. IEEE. 1994, pp. 1075–1076 (cit. on p. 54).

[Bay+08] Herbert Bay, Andreas Ess, Tinne Tuytelaars, and Luc Van Gool. “Speeded-up robust features (SURF)”. In: *Computer vision and image understanding* 110.3 (2008), pp. 346–359 (cit. on p. 119).

[BM94] Dennis G Begos and Irvin M Modlin. “Laparoscopic cholecystectomy: from gimmick to gold standard.” In: *Journal of clinical gastroenterology* 19.4 (1994), pp. 325–330 (cit. on p. 23).

[Ber+13] Matthew Berger, Joshua A Levine, Luis Gustavo Nonato, Gabriel Taubin, and Claudio T Silva. “A benchmark for surface reconstruction”. In: *ACM Transactions on Graphics (TOG)* 32.2 (2013), pp. 1–17 (cit. on p. 63).

[BHC93] JC Bezdek, LO Hall, and LP Clarke. “Review of MR image segmentation techniques using pattern recognition”. In: *Medical Physics* 20.4 (1993), p. 4 (cit. on p. 54).

[Bil14] Alexandre Bilger. “Patient-specific biomechanical simulation for deep brain stimulation”. PhD thesis. Université des Sciences et Technologie de Lille, 2014.

[BTC95] Eric Bittar, Nicolas Tsingos, and Marie-Paule Cani. “Automatic Reconstruction of Unstructured 3D data : Combining Medial Axis and Implicit Surfaces”. Anglais. In: *Eurographics*. Ed. by Frits Post and Martin Göbel. Vol. 14. 3. Published under the name Marie-Paule Gascuel. Maastricht, Pays-Bas: Blackwell Publishers, 1995, pp. 457–468 (cit. on pp. 70, 72).

[Bli82] James F. Blinn. “A Generalization of Algebraic Surface Drawing”. In: *ACM Trans. Graph.* 1.3 (July 1982), pp. 235–256 (cit. on p. 70).

[Blo95] Jules Bloomenthal. “Skeletal design of natural forms”. PhD thesis. Calgary, Alta., Canada, Canada, 1995 (cit. on p. 58).

[BA11] Craig A Blum and David B Adams. “Who did the first laparoscopic cholecystectomy?” In: *Journal of minimal access surgery* 7.3 (2011), p. 165 (cit. on p. 23).

[CG01] T. Chaperon and F. Goulette. “Extracting cylinders in full 3D data using a random sampling method and the Gaussian image”. In: *Vision Modeling and Visualization Conference (VMW’01)*. 2001, pp. 35–42 (cit. on pp. 67, 68).

[CW06] Christian Beder and Wolfgang Förstner. “Direct solutions for computing cylinders from minimal sets of points”. In: *9th European Conference on Computer Vision (ECCV’06)*. Vol. 3954. LNCS. May 2006, pp. 135–146 (cit. on p. 67).

[Cle+08] Logan W Clements, William C Chapman, Benoit M Dawant, Robert L Galloway Jr, and Michael I Miga. “Robust surface registration using salient anatomical features for image-guided liver surgery: algorithm and validation”. In: *Medical physics* 35.6Part1 (2008), pp. 2528–2540.

[Clo+00] Harry J Cloft, Gregory J Joseph, Frank C Tong, Jonas H Goldstein, and Jacques E Dion. “Use of three-dimensional Guglielmi detachable coils in the treatment of wide-necked cerebral aneurysms”. In: *American Journal of Neuroradiology* 21.7 (2000), pp. 1312–1314 (cit. on p. 50).

[CCD10] Olivier. Comas, Stéphane Cotin, and Christian Duriez. “A Shell Model for Real-Time Simulation of Intra-ocular Implant Deployment”. In: *International Symposium on Computational Models for Biomedical Simulation*. Vol. 5958. Lecture Notes in Computer Science. Springer, 2010, pp. 160–170 (cit. on p. 43).

[Cou+10] Hadrien Courtecuisse, Hoeryong Jung, Jérémie Allard, Christian Duriez, Doo Yong Lee, and Stéphane Cotin. “GPU-based Real-Time Soft Tissue Deformation with Cutting and Haptic Feedback”. In: *Progress in Biophysics and Molecular Biology* 103.2-3 (Dec. 2010). Special Issue on Soft Tissue Modelling, pp. 159–168 (cit. on p. 43).

[CHH04] William R Crum, Thomas Hartkens, and DLG Hill. “Non-rigid image registration: theory and practice”. In: *The British journal of radiology* 77.suppl_2 (2004), S140–S153 (cit. on p. 125).

[DBB08] Benoit Dagon, Charles Baur, and Vincent Bettschart. “A framework for intra-operative update of 3D deformable models in liver surgery”. In: *2008 30th Annual International Conference of the IEEE Engineering in Medicine and Biology Society*. IEEE. 2008, pp. 3235–3238 (cit. on p. 118).

[De +11] Hans De Visser, Marcus O Watson, Olivier Salvado, and Joshua D. Passenger. “Progress in virtual reality simulators for surgical training and certification”. In: *Medical Journal of Australia* 194.4 (2011), S38 (cit. on p. 2).

[DOG04] Daniel Dekkers, Kees van Overveld, and Rob Golsteijn. “Combining CSG modeling with soft blending using Lipschitz-based implicit surfaces”. English. In: *The Visual Computer* 20.6 (2004), pp. 380–391 (cit. on p. 70).

[DNV06] Piet Dirix, Sandra Nuyts, and Walter Van den Bogaert. “Radiation-induced xerostomia in patients with head and neck cancer: a literature review”. In: *Cancer: Interdisciplinary International Journal of the American Cancer Society* 107.11 (2006), pp. 2525–2534 (cit. on p. 125).

[Dog13] Issam Doghri. *Mechanics of deformable solids: linear, nonlinear, analytical and computational aspects*. Springer Science & Business Media, 2013 (cit. on p. 26).

[Dou+06] Craig C. Douglas, Jonathan D. Beezley, Janice Coen, Deng Li, Wei Li, Alan K. Mandel, Jan Mandel, Guan Qin, and Anthony Vodacek. “Demonstrating the Validity of a Wildfire DDDAS”. In: *Computational Science – ICCS 2006: 6th International Conference, Reading, UK, May 28-31, 2006. Proceedings, Part III*. Springer Berlin Heidelberg, 2006, pp. 522–529.

[Dur+06] C. Duriez, S. Cotin, J. Lenoir, and P. F. Neumann. “New Approaches to Catheter Navigation for Interventional Radiology Simulation”. In: *Computer Aided Surgery* 11 (2006), pp. 300–308 (cit. on pp. 30, 31).

[DAK04] Christian Duriez, Claude Andriot, and Abderrahmane Kheddar. “Signorini’s contact model for deformable objects in haptic simulations”. In: *2004 IEEE/RSJ International Conference on Intelligent Robots and Systems (IROS)(IEEE Cat. No. 04CH37566)*. Vol. 4. IEEE. 2004, pp. 3232–3237 (cit. on p. 132).

[EP11] Haytham Elhawary and Aleksandra Popovic. “Robust feature tracking on the beating heart for a robotic-guided endoscope”. In: *The international journal of medical robotics and computer assisted surgery* 7.4 (2011), pp. 459–468 (cit. on p. 119).

[Fau+12] François Faure, Christian Duriez, Hervé Delingette, Jérémie Allard, Benjamin Gilles, Stéphanie Marchesseau, Hugo Talbot, Hadrien Courtecuisse, Guillaume Bousquet, Igor Peterlik, et al. “Sofa: A multi-model framework for interactive physical simulation”. In: *Soft tissue biomechanical modeling for computer assisted surgery*. Springer, 2012, pp. 283–321 (cit. on p. 117).

[Fig+10] Michael Figl, Daniel Rueckert, David Hawkes, Roberto Casula, Mingxing Hu, Ose Pedro, Dong Ping Zhang, Graeme Penney, Fernando Bello, and Philip Edwards. “Image guidance for robotic minimally invasive coronary artery bypass”. In: *Computerized Medical Imaging and Graphics* 34.1 (2010), pp. 61–68 (cit. on p. 114).

[Fis+02] Bruce Fischl, David H Salat, Evelina Busa, Marilyn Albert, Megan Dieterich, Christian Haselgrove, Andre Van Der Kouwe, Ron Killiany, David Kennedy, Shuna Klaveness, et al. “Whole brain segmentation: automated labeling of neuroanatomical structures in the human brain”. In: *Neuron* 33.3 (2002), pp. 341–355 (cit. on p. 54).

[FU06] J. Florens and D. Urma. “Dynamical Issues at the Low Level of Human/Virtual Object Interaction”. In: *2006 14th Symposium on Haptic Interfaces for Virtual Environment and Teleoperator Systems*. Mar. 2006, pp. 315–320 (cit. on p. 26).

[Fri+10] O. Friman, M. Hindennach, C. Kühnel, and H.-O. Peitgen. “Multiple hypothesis template tracking of small 3D vessel structures”. In: *MedIA* 14.2 (2010), pp. 160–171 (cit. on pp. 67, 77).

[Gol05] Ron Goldman. “Curvature formulas for implicit curves and surfaces”. In: *Comput. Aided Geom. Des.* 22.7 (Oct. 2005), pp. 632–658 (cit. on p. 72).

[HL00] E Mark Haacke and Zhi-Pei Liang. “Challenges of imaging structure and function with MRI”. In: *IEEE Engineering in Medicine and Biology Magazine* 19.5 (2000), pp. 55–62 (cit. on p. 54).

[HK76] J.C. Halpin and J.L. Kardos. “The halpin-tsai equations: a review”. In: *Polymer Engineering Science* 16 (1976), pp. 344–52 (cit. on p. 33).

[Hao15] Nazim Haouchine. “Image-guided simulation for augmented reality during hepatic surgery”. PhD thesis. Université des Sciences et Technologie de Lille - Lille I, 2015 (cit. on pp. 5, 123).

[HK98] SA Hojjatoleslami and Josef Kittler. “Region growing: a new approach”. In: *IEEE Transactions on Image processing* 7.7 (1998), pp. 1079–1084 (cit. on p. 54).

[Hum03] Jay D Humphrey. “Review Paper: Continuum biomechanics of soft biological tissues”. In: *Proceedings of the Royal Society of London A: Mathematical, Physical and Engineering Sciences*. Vol. 459. The Royal Society. 2003, pp. 3–46 (cit. on p. 2).

[Iwa+11] Naoya Iwamoto, Ryusuke Sagawa, Shoji Kunitomo, and Shigeo Morishima. “Estimating fluid simulation parameters from videos”. In: *ACM SIGGRAPH 2011 Posters*. 2011, p. 3.

[Jel+02] James S Jelinek, Mark D Murphey, James A Welker, Robert M Henshaw, Mark J Kransdorf, Barry M Shmookler, and Martin M Malawer. “Diagnosis of Primary Bone Tumors with Image-guided Percutaneous Biopsy: Experience with 110 Tumors 1”. In: *Radiology* 223.3 (2002), pp. 731–737 (cit. on p. 1).

[Jia17] Zhifan Jiang. “Évaluation des mobilités et modélisation géométrique du système pelvien féminin par analyse d’images médicales”. PhD thesis. Université des Sciences et Technologie de Lille, 2017 (cit. on pp. 5, 88).

[KWT88] Michael Kass, Andrew Witkin, and Demetri Terzopoulos. “Snakes: Active contour models”. In: *International journal of computer vision* 1.4 (1988), pp. 321–331 (cit. on p. 54).

[Ker06] Amy E Kerdok. “Characterizing the nonlinear mechanical response of liver to surgical manipulation”. In: (2006) (cit. on p. 115).

[Kim+12] Jae-Hak Kim, Adrien Bartoli, Toby Collins, and Richard Hartley. “Tracking by detection for interactive image augmentation in laparoscopy”. In: *International Workshop on Biomedical Image Registration*. Springer. 2012, pp. 246–255 (cit. on p. 114).

[KP93] S Kumar and A Petho. “An algorithm for the numerical inversion of a tridiagonal matrix”. In: *Communications in Numerical Methods in Engineering* 9.4 (1993), pp. 353–359 (cit. on p. 33).

[Lec+15] Pauline Lecomte-Grosbras, J-F Witz, Mathias Brieu, N Faye, Michel Cosson, and Chrystele Rubod. “Quantification of pelvic mobility on dynamic magnetic resonance images: using mechanical insight to help diagnose pelvic pathologies”. In: *Strain* 51.4 (2015), pp. 301–310 (cit. on p. 108).

[Len+05] Julien Lenoir, Stéphane Cotin, Christian Duriez, and Paul Neumann. “Interactive physically-based simulation of Catheter and Guidewire”. In: *Second Workshop in Virtual Reality Interactions and Physical Simulations (VRIPHYS)*. Pisa - Italy, Nov. 2005 (cit. on p. 33).

[LK+81] Bruce D Lucas, Takeo Kanade, et al. “An iterative image registration technique with an application to stereo vision”. In: (1981) (cit. on pp. 101, 102, 119).

[Mar+10] Stéphanie Marchesseau, Tobias Heimann, Simon Chatelin, Rémy Willinger, and Hervé Delingette. “Fast porous visco-hyperelastic soft tissue model for surgery simulation: application to liver surgery”. In: *Progress in biophysics and molecular biology* 103.2-3 (2010), pp. 185–196 (cit. on p. 116).

[Mar+97] J. A. Martin, G. Regehr, R. Reznick, H. MacRae, J. Murnaghan, Hutchison C., and Brown M. “Objective Structured Assessment of Cataract Surgical Skill”. In: *The British journal of surgery* 84 (2 1997), pp. 273–278 (cit. on p. 46).

[Mor+09] Francesc Moreno-Noguer, Mathieu Salzmann, Vincent Lepetit, and Pascal Fua. “Capturing 3D stretchable surfaces from single images in closed form”. In: *2009 IEEE Conference on Computer Vision and Pattern Recognition*. IEEE. 2009, pp. 1842–1849 (cit. on p. 119).

[Mul+10] Patrick Mullen, Fernando De Goes, Mathieu Desbrun, David Cohen-Steiner, and Pierre Alliez. “Signing the unsigned: Robust surface reconstruction from raw pointsets”. In: *Computer Graphics Forum*. Vol. 29. 5. Wiley Online Library. 2010, pp. 1733–1741 (cit. on p. 63).

[Mur91] S. Muraki. “Volumetric shape description of range data using Blobby Model”. In: *SIGGRAPH Comput. Graph.* 25 (4 1991), pp. 227–235 (cit. on pp. 70, 72, 73).

[Nea+06] Andrew Nealen, Matthias Müller, Richard Keiser, Eddy Boxerman, and Mark Carlson. “Physically based deformable models in computer graphics”. In: *Computer graphics forum*. Vol. 25. 4. Wiley Online Library. 2006, pp. 809–836 (cit. on p. 26).

[Nel+12] Benjamin E Nelms, Greg Robinson, Jay Markham, Kyle Velasco, Steve Boyd, Sharath Narayan, James Wheeler, and Mark L Sobczak. “Variation in external beam treatment plan quality: an inter-institutional study of planners and planning systems”. In: *Practical radiation oncology* 2.4 (2012), pp. 296–305 (cit. on p. 125).

[NPF05] Matthieu Nesme, Yohan Payan, and François Faure. “Efficient, physically plausible finite elements”. In: 2005 (cit. on p. 116).

[Nic+11] Stéphane Nicolau, Luc Soler, Didier Mutter, and Jacques Marescaux. “Augmented reality in laparoscopic surgical oncology”. In: *Surgical Oncology* 20.3 (2011), pp. 189–201 (cit. on p. 113).

[Oht+05] Yutaka Ohtake, Alexander Belyaev, Marc Alexa, Greg Turk, and Hans-Peter Seidel. “Multi-level partition of unity implicits”. In: *Acm Siggraph 2005 Courses*. 2005, 173–es (cit. on p. 63).

[Okt+13] Ozan Oktay, Li Zhang, Tommaso Mansi, Peter Mountney, Philip Mewes, Stéphane Nicolau, Luc Soler, and Christophe Chefd’hotel. “Biomechanically driven registration of pre-to intra-operative 3d images for laparoscopic surgery”. In: *International Conference on Medical Image Computing and Computer-Assisted Intervention*. Springer. 2013, pp. 1–9 (cit. on p. 118).

[PDC11] Igor Peterlik, Christian Duriez, and Stéphane Cotin. “Asynchronous haptic simulation of contacting deformable objects with variable stiffness”. In: *2011 IEEE/RSJ International Conference on Intelligent Robots and Systems*. IEEE. 2011, pp. 2608–2613 (cit. on p. 37).

[PDC12] Igor Peterlık, Christian Duriez, and Stéphane Cotin. “Modeling and real-time simulation of a vascularized liver tissue”. In: *International Conference on Medical Image Computing and Computer-Assisted Intervention*. Springer. 2012, pp. 50–57 (cit. on pp. 116, 117).

[Pha01] Dzung L Pham. “Robust fuzzy segmentation of magnetic resonance images”. In: *Computer-Based Medical Systems, 2001. CBMS 2001. Proceedings. 14th IEEE Symposium on*. IEEE. 2001, pp. 127–131 (cit. on p. 54).

[Pra+10] Philip Pratt, Danail Stoyanov, Marco Visentini-Scarzanella, and Guang-Zhong Yang. “Dynamic guidance for robotic surgery using image-constrained biomechanical models”. In: *International Conference on Medical Image Computing and Computer-Assisted Intervention*. Springer. 2010, pp. 77–85 (cit. on p. 114).

[Prz68] J.S. Przemieniecki. *Theory of Matrix Structural Analysis*. McGraw-Hill, 1968 (cit. on pp. 30, 116).

[PM13] GA Puerto-Souza and GL Mariottini. “An augmented-reality system for laparoscopic surgery robust to complete occlusions and fast camera motions”. In: *International Conference on Robotics and Automotion*. 2013 (cit. on p. 114).

[RF14] Julien Réthoré and Marc François. “Curve and boundaries measurement using B-splines and virtual images”. In: *Optics and Lasers in Engineering* 52 (2014), pp. 145–155 (cit. on p. 91).

[RKK03] Josef Rösch, Frederick S Keller, and John A Kaufman. “The birth, early years, and future of interventional radiology”. In: *Journal of Vascular and Interventional Radiology* 14.7 (2003), pp. 841–853 (cit. on p. 22).

[Rot82] Scott D Roth. “Ray casting for modeling solids”. In: *Computer graphics and image processing* 18.2 (1982), pp. 109–144 (cit. on p. 120).

[Sal+07] Georges M. Saleh, V. Gauba, Arijit Mitra, Andre S. Litwin, Andrew K. K. Chung, and Larry Benjamin. “Objective Structured Assessment of Cataract Surgical Skill”. In: *Archives of Ophthalmology* 125 (3 2007), pp. 363–366 (cit. on p. 46).

[SF10] Mathieu Salzmann and Pascal Fua. “Linear local models for monocular reconstruction of deformable surfaces”. In: *IEEE Transactions on Pattern Analysis and Machine Intelligence* 33.5 (2010), pp. 931–944 (cit. on p. 119).

[Sat+98] K Satoh, J Satomi, S Matsubara, and S Nagahiro. “Measurement of volume ratio to predict coil compaction, on aneurysmal embolization”. In: *Interventional Neuroradiology* 4.1_suppl (1998), pp. 179–182 (cit. on p. 50).

[Sch22] Pierre Schegg. “Autonomous Catheter and Guidewire Navigation for Robotic Percutaneous Coronary Interventions”. PhD thesis. Université des Sciences et Technologie de Lille, 2022 (cit. on p. 5).

[SFA10] Benoit Semin, Marc Louis Maurice François, and Harold Auradou. “Analytical shape determination of fiber-like objects with Virtual Image Correlation”. In: *arXiv preprint arXiv:1001.2636* (2010) (cit. on p. 91).

[SV16] N Senthilkumaran and S Vaithegi. “Image segmentation by using thresholding techniques for medical images”. In: *Computer Science & Engineering: An International Journal* 6.1 (2016), pp. 1–13 (cit. on p. 54).

[Ser+03] Maxime Sermesant, Clément Forest, Xavier Pennec, Hervé Delingette, and Nicholas Ayache. “Deformable biomechanical models: Application to 4D cardiac image analysis”. In: *Medical image analysis* 7.4 (2003), pp. 475–488 (cit. on p. 114).

[SLH10] Tian Shen, Hongsheng Li, and Xiaolei Huang. “Active volume models for medical image segmentation”. In: *IEEE transactions on medical imaging* 30.3 (2010), pp. 774–791 (cit. on p. 114).

[She99] A. Sherstyuk. “Kernel Functions in Convolution Surfaces: A Comparative Analysis”. In: *The Visual Computer* 15.4 (1999), pp. 171–182 (cit. on p. 70).

[Sig33] Antonio Signorini. “Sopra alcune questioni di statica dei sistemi continui”. In: *Annali della Scuola Normale Superiore di Pisa-Classe di Scienze* 2.2 (1933), pp. 231–251 (cit. on p. 132).

[Sil+09] M Silvennoinen, J-P Mecklin, P Saariluoma, and T Antikainen. “Expertise and skill in minimally invasive surgery”. In: *Scandinavian Journal of Surgery* 98.4 (2009), pp. 209–213 (cit. on p. 1).

[Sin+02] V. Singha, D. Gressa, R. Higashidab, C. Dowdb, V. Halbachb, and S. Johnston. “The Learning Curve for Coil Embolization of Unruptured Intracranial Aneurysms”. In: *American Journal of Neuroradiology* 23 (2002), pp. 768–771 (cit. on p. 47).

[Spe+11] S Speidel, S Roehl, S Suwelack, R Dillmann, H Kenngott, and B Mueller-Stich. “Intraoperative surface reconstruction and biomechanical modeling for soft tissue registration”. In: *Proc. Joint Workshop on New Technologies for Computer/Robot Assisted Surgery*. 2011, pp. 0–0 (cit. on p. 114).

[Ste13] Martin Oliver Steinhauser. *Computer simulation in physics and engineering*. Walter de Gruyter, 2013 (cit. on p. 21).

[Su+09] Li-Ming Su, Balazs P Vagvolgyi, Rahul Agarwal, Carol E Reiley, Russell H Taylor, and Gregory D Hager. “Augmented reality during robot-assisted laparoscopic partial nephrectomy: toward real-time 3D-CT to stereoscopic video registration”. In: *Urology* 73.4 (2009), pp. 896–900 (cit. on p. 114).

[Tal14] Hugo Talbot. “Interactive Patient-Specific Simulation of Cardiac Electrophysiology”. PhD thesis. Université des Sciences et Technologies de Lille, 2014.

[Tam+02] Shinichi Tamatani, Yasushi Ito, Hiroshi Abe, Tetsuo Koike, Shigekazu Takeuchi, and Ryuichi Tanaka. “Evaluation of the stability of aneurysms after embolization using detachable coils: correlation between stability of aneurysms and embolized volume of aneurysms”. In: *American Journal of Neuroradiology* 23.5 (2002), pp. 762–767 (cit. on p. 50).

[Tau91] G. Taubin. “Estimation of Planar Curves, Surfaces, and Nonplanar Space Curves Defined by Implicit Equations with Applications to Edge and Range Image Segmentation”. In: *PAMI* 13 (11 1991), pp. 1115–1138 (cit. on pp. 73, 81, 82).

[Teb+09] Dogu Teber, Selcuk Guven, Tobias Simpfendörfer, Mathias Baumhauer, Esref Oguz Güven, Faruk Yencilek, Ali Serdar Gözen, and Jens Rassweiler. “Augmented reality: a new tool to improve surgical accuracy during laparoscopic partial nephrectomy? Preliminary in vitro and in vivo results”. In: *European urology* 56.2 (2009), pp. 332–338 (cit. on p. 114).

[Fel00] C. A. Felippa. *A systematic approach to the element independent corotational dynamics of finite elements*. Tech. rep. CU-CAS-00-03. Center for Aerospace Structures, 2000 (cit. on pp. 31, 116).

[TBC95] N. Tsingos, E. Bittar, and M.-P. Cani. “Implicit Surfaces for Semi-Automatic Medical Organ Reconstruction”. In: *Computer Graphics Internat. (CGI’95)*. 1995, pp. 3–15 (cit. on pp. 72, 73).

[Vei+14] Catarina Veiga, Jamie McClelland, Syed Moinuddin, Ana Lourenço, Kate Ricketts, James Annkah, Marc Modat, Sébastien Ourselin, Derek D'Souza, and Gary Royle. "Toward adaptive radiotherapy for head and neck patients: feasibility study on using CT-to-CBCT deformable registration for "dose of the day" calculations". In: *Medical physics* 41.3 (2014) (cit. on p. 125).

[WMK06] Ruikang K Wang, Zhenhe Ma, and Sean J Kirkpatrick. "Tissue Doppler optical coherence elastography for real time strain rate and strain mapping of soft tissue". In: *Applied Physics Letters* 89.14 (2006), p. 144103 (cit. on p. 21).

[Web03] Steve Webb. "The physical basis of IMRT and inverse planning". In: *The British journal of radiology* 76.910 (2003), pp. 678–689 (cit. on p. 125).

[WNV00] Onno Wink, Wiro J. Niessen, and Max A. Viergever. "Fast Delineation and Visualization of Vessels in 3D Angiographic Images". In: *IEEE Trans. Med. Imaging* 19.4 (2000), pp. 337–346 (cit. on p. 69).

[WH94] Andrew P Witkin and Paul S Heckbert. "Using particles to sample and control implicit surfaces". In: *Proceedings of the 21st annual conference on Computer graphics and interactive techniques*. 1994, pp. 269–277.

[WC07a] W.C.K Wong and A.C.S Chung. "Probabilistic vessel axis tracing and its application to vessel segmentation with stream surfaces and minimum cost paths". In: *MedIA* 11 (2007), pp. 567–587 (cit. on pp. 67, 68).

[WC07b] Wilbur CK Wong and Albert CS Chung. "Probabilistic vessel axis tracing and its application to vessel segmentation with stream surfaces and minimum cost paths". In: *Medical Image Analysis* 11.6 (2007), pp. 567–587.

[WLS12] Stefanie Wuhrer, Jochen Lang, and Chang Shu. "Tracking complete deformable objects with finite elements". In: *2012 Second International Conference on 3D Imaging, Modeling, Processing, Visualization & Transmission*. IEEE. 2012, pp. 1–8 (cit. on p. 119).

[YAG+05] Kenji YAGI, Koichi SATOH, Junichiro SATOMI, Shunji MATSUBARA, and Shinji NAGAHIRO. "Evaluation of Aneurysm Stability After Endovascular Embolization With Guglielmi Detachable Coils: Correlation Between Long-Term Stability and Volume Embolization Ratio". In: *Neurologia medico-chirurgica* 45.11 (2005), pp. 561–566 (cit. on p. 50).

[YC14] Michael C Yip and David B Camarillo. "Model-less feedback control of continuum manipulators in constrained environments". In: *IEEE Transactions on Robotics* 30.4 (2014), pp. 880–889 (cit. on p. 133).

[Yur14] Ahmed Yureidini. "Robust blood vessel surface reconstruction for interactive simulations from patient data". PhD thesis. Université des Sciences et Technologie de Lille - Lille I, 2014 (cit. on p. 5).

[Zac01] Gabriel Zachmann. "Optimizing the collision detection pipeline". In: *Proc. of the First International Game Technology Conference (GTEC)*. Vol. 2. 2001 (cit. on p. 56).

[Zha19] Zhongkai Zhang. "vision-based calibration, position control and force sensing for soft robots". PhD thesis. université de lille, Jan. 2019 (cit. on p. 5).

[ZZ87] Olgierd C Zienkiewicz and Jian Z Zhu. "A simple error estimator and adaptive procedure for practical engineerng analysis". In: *International journal for numerical methods in engineering* 24.2 (1987), pp. 337–357 (cit. on p. 34).

List of Figures

List of Tables